ELECTRODYNAMICS OF RELATIVISTIC ELECTRON BEAM X-RAY SOURCES

A DISSERTATION SUBMITTED TO THE GRADUATE DIVISION OF THE
UNIVERSITY OF HAWAI'I AT MĀNOA IN PARTIAL FULFILLMENT
OF THE REQUIREMENTS FOR THE DEGREE OF

DOCTOR OF PHILOSOPHY

IN

PHYSICS

MAY 2016

By

Pardis Niknejadi

Dissertation Committee:

John Madey, Chairperson
Eric Szarmes
Gary Varner
Jelena Maricic
Susanne Still

Keywords: Electrodynamics, Free Electron Lasers, Accelerator Physics, Beam Dynamics, Coherent Radiation

To my family and friends.

ACKNOWLEDGMENTS

ABSTRACT

Probing matter at atomic scales provides invaluable information about its structure; as a result interest in sources of x-rays and γ-rays with high spectral resolution, low angular divergence and small source size has been on the rise. Explorations in this domain require x-ray or γ-ray sources with high brightness. In the past decade, relativistic electron sources such as synchrotron rings and free electron lasers have proven to be the best technology available for the production of such beams. We[1] start with an introduction to the physics of radiation and provide a summary of the theoretical grounds this work is based on. This dissertation is dedicated to different aspects of both fundamental processes of radiation in relativistic electron sources, and critical control and diagnostics that are required for the operation of these sources. Therefore this work is broken into two main parts.

In the first part, the electron source that is currently set up at University of Hawai'i at Manoa will be introduced in detail. This source has unique capabilities as it is an inverse-Compton scattering (ICS) source that uses a free electron laser (FEL) with pulses of picosecond duration at ~ 3 GHz rate for production of a coherent/semi-coherent x-ray beam by means of an optical cavity. After introducing the essential elements of the system and what was achieved prior to this work, we will focus on the requirements for achieving an optimum electron beam matched for the operation of the system which is the main focus of part I of this dissertation. The transport beam line of our system is unique and complex. For this reason, a simulation module has been developed for the study and delivery of an optimal beam. We will discuss the capabilities of this system and its compatibility with other elements that were already installed on the beam line.

Finally, we will present results and experimental data as well as guidelines for future operation of the system when the microwave gun has been enhanced and/or the optical cavity (the final step of this proof-of-principle experiment) has been commissioned. Due to the complexity of this integrated system, one of the goals of this work is to serve the future members and staff of the UH FEL laboratory in configuring and operating this complex system. The final goal of the UH ICS project is to establish the principles on which producing

---

[1] Even though this dissertation was completed by one person, as hardly any scientific work is ever completed by one, it is written in first person plural. Only in this way, it is possible to give credit to those who have contributed to this research by spending their time till the late hours of the night and sometimes even early morning in the control room. For the theoretical work, the hope is to also invite the reader to follow the work closely and check its validity as they read along, as well as to acknowledge the fruitful conversations that have led to the discussions and conclusions presented here.

a successful turn-key commercial inverse-Compton x-ray source will depend on.

In the second part of this work we start with the discussion of coherent radiation at its most fundamental level, with emphasis on conservation of energy. We show that for coherently radiating particles the failure of conventional classical electrodynamics (CED) is far more serious than the well-known failure of CED at small scales. We will present a covariant picture of radiation in terms of the theory of action-at-a-distance and introduce a time-symmetric approach to electrodynamics. We demonstrate that this time symmetric approach provides a perfect match to the energy radiated by two coherently oscillating charged particles. This work is novel, as this was an unsolved problem in classical electrodynamics up until now. We also discuss how the conceptual implication of this work is demanding. For this purpose, we will propose two different experiments that can further our understanding of the presented problem.

The first experiment involves a small ($\lambda/10$) antenna, and the goal is to measure the advanced field of the absorber at distances of 5λ or less. Calculation and precise measurement of the antenna field/potential at distances of order λ is challenging, causing this experiment to be a difficult yet possible task. In the second experiment, we discuss in some detail the experimental setup that would verify and/or further our understanding of the underlying physics of Self Amplified Spontaneous Emission (SASE) FELs. We provide an analytical verification as a first step toward better understanding the process, and provide a list of required parameters for the SASE test. These parameters are at the edge of current technology of current light sources, making this experiment also a demanding and challenging task. We conclude that further detailed studies by means of simulation or analytical approaches can reduce the strain of SASE test.

TABLE OF CONTENTS

LIST OF TABLES

LIST OF FIGURES

CHAPTER 1
INTRODUCTION

The human eye has a temporal resolution of 0.1 second. This means we are not able to detect changes faster than one tenth of a second (10 Hertz or Hz). The flickering of a fluorescent lamp at 100 or 120 Hz is usually unnoticed by our eyes. Our eyes are also optimized to see only the visible range of the electromagnetic radiation (the colors red to violet with wavelength of approximately 0.4 to 0.7 microns). Therefore, we have rather limited tool sets for observing and understanding our universe. In 1895, Wilhelm Röntgen discovered an unknown (at the time) type of radiation that could pass through human tissue but would not pass through bone [1]. Today such radiation is known as x-rays. X-rays with wavelength above 0.2-0.1 nm (photon energies below 5-10 keV) are considered soft x-rays and those with shorter wavelength are considered hard x-rays. Radiation with wavelength shorter than 0.01 nm is considered gamma radiation or γ-rays. Since x-rays and γ-rays are on the order of atomic scales, today they serve as one of the most important tools for probing a wide variety of phenomena across many diverse areas of science as well as technology.

1.1　High Brightness Beam Sources

Relativistic electron beams have proven to be the best source of intense and highly directional x-rays and γ-rays. Synchrotron radiation was discovered in the 1940s and it was the means by which the electron lost its energy in an accelerating ring (initially not a desired effect for high energy physics experiments). Synchrotron sources produce radiation by sending the electrons through a bend (bending magnet) or wiggling motion (wiggler or undulator). In the 1980's the first dedicated Synchrotron sources came online. The advantage of these sources is that they provide quasi-coherent radiation in a wide spectral range (UV to 0.1 Å hard x-rays). Another type of highly relativistic electron beam source is an inverse-Compton scattering (ICS) source, where typically longer wavelength electromagnetic radiation (radio, infrared or visible) collides head on with a highly relativistic electron beam ($\gamma \sim 100$) to produce scattered (UV, x-rays, γ-rays). The electrons' energy loss to the incident photons during ICS is identical to the electrons' energy loss to the synchrotron radiation in a bend or in an undulator (when $\gamma \hbar \omega << m_e c^2$). ICS sources are typically more compact and are great sources for creating high brightness, high energy photon beams. These sources

have contributed greatly to our knowledge and understanding of many aspects of biology, chemistry and physics.

Up to the 1970's, however, there was a lack of coherent light sources in the 1 mm to 1 μm (Terahertz and IR) as well as sub nm regime because atomic laser and microwave sources did not cover these areas of the spectrum. In 1971, John Madey coined the term free electron laser (FEL) in his paper "Stimulated emission of bremsstrahlung in a periodic magnetic field" [2]. Bremsstrahlung, or breaking radiation, refers to the radiation emitted during deceleration of the electron beam (again not a desired effect). FEL is a coherent radiation source in which the radiation comes from the free electrons and not the bound electrons of a lasing medium. The difference between the radiation from an undulator and the radiation from a FEL is that in an FEL, under some favorable conditions, the spontaneous electromagnetic radiation (synchrotron radiation) from the "free" electrons in the undulator interacts with the electrons in such a way that induces acceleration. This induced acceleration in turn produces additional radiation that amplifies the electromagnetic radiation. The resonant wavelength at which the FEL operates depends on the electron beam, undulator period, and the strength of the magnetic field of the undulator. Therefore in principle the FEL can be tuned to different wavelengths by changing the electron beam energy. On the other hand, the process of amplification needs ample time (distance). Therefore the feasibility of operating at a certain wavelength becomes the main question.

The first successful operation of an FEL was in 1976, when Madey and his coworkers configured an FEL as an amplifier at a wavelength of 10 μm (Fig. 1.1). This success led to an experiment the following year which utilized the same undulator as an oscillator, by means of an optical cavity, at 3 μm wavelength (Fig. 1.2). This supported the tuneability of the FELs, and for the first time, presented a coherent source in the IR regime. Initially for shorter wavelengths, due to their ability to penetrate matter (the optical cavity mirrors), oscillator designs were not feasible. In recent years, however, because of the rapid progress in the field of multilayer quartz, silicon and diamond mirrors, an x-ray FEL oscillator (XEFLO) design is currently under research and development at Argonne National Laboratory (ANL) [3]. In the 1980s, a new design for coherent x-ray sources was introduced that operates based on self-amplified spontaneous emission (SASE) [3] of the electron beam in an undulator, where the concept of optical cavity is replaced with length. In 1992, it was proposed by Claudio Pellegrini [4] to build a SASE x-ray FEL in place of the previously present 40 MeV, two miles long, linear accelerator at Stanford Linear Accelerator Center (SLAC) National Laboratory utilizing the existing linac sections. The total undulator length at SLAC is 3 km [5]. In

recent years several few large research facilities have come on line and more are on their way. Since 2005, FLASH at Deutsches Electronen-SYnchrotron (DESY) in Germany has been operating in soft x-ray regime [6]; FERMI at Sincrotrone Trieste in Italy is another soft x-ray source. Currently the Linac Coherent Light Source (LCLS) at SLAC holds the record in the hard x-ray regime, having a coherent photon beam of 1.5 Å wavelength [7]. SACLA in Japan has also been successfully commissioned [4]. Three more hard x-ray FELs are under construction: European XFEL [8], Pohang Accelerator Laboratory (PAL) in Korea, and SwissFEL in Switzerland. Therefore research and development for coherent sources that allow study of mater at 10-100's of femtosecond time scale, and with a 1nm to sub Å resolution, is very active.
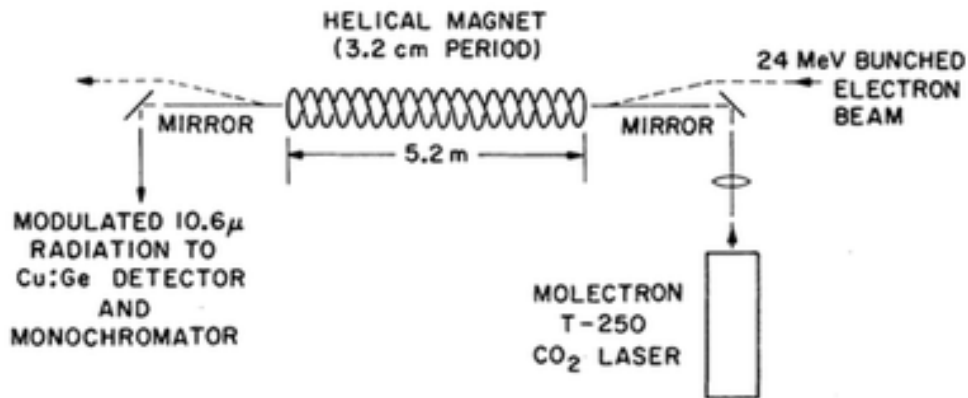
Figure 1.1: Schematic of the 1976 FEL amplifier experiment by Madey and co-workers from [9].
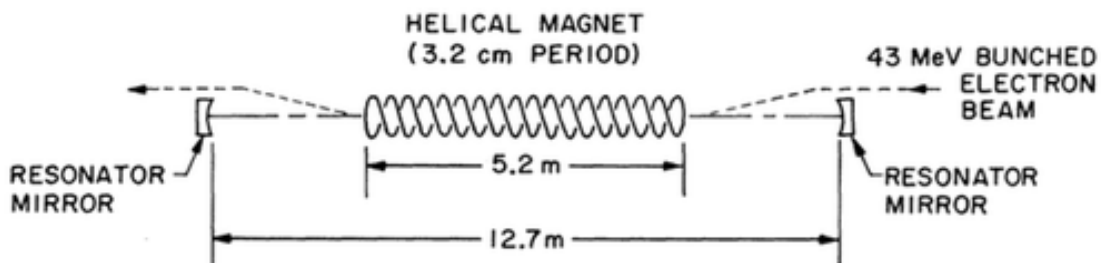
Figure 1.2: Schematic of the 1977 FEL oscillator experiment by Madey and co-workers from [10].

Spectral brightness $\mathcal{B}$ is a measure of quality of the photon beams. Brightness is defined by the six dimensional volume occupied by the photon beam (with a certain frequency

bandwidth) in phase space. In addition to $\mathcal{B}$, etendue or matching spot-size and divergence of source and target is also crucial [11].

$$\mathcal{B} = \frac{spectral\ flux}{transverse\ phase\ space\ area}\ (\frac{photons}{sec \times mm^2 \times mrad^2 \times 0.1\%BW}) \qquad (1.1)$$

LCLS and SACLA x-ray pulses have very high intensity and brightness, with a peak power of tens of GW in a pulse with duration between a few to about 100 fs. This could often lead to total destruction of the sample under study and has demands faster and higher resolution x-ray detector for photon detection. Therefore the need for a source with high brightness and high average power has been on the rise.

A novel high brightness 5-20 keV inverse-Compton x-ray source, Mark V (MkV), is under development at the University of Hawai'i at Manoa (UHM). This system utilizes elements and concepts that are widely recognized and well understood yet have never been put to practical use in one place before [12, 13, 14]. Additionally, it can match requirements of spot size and divergence (etendue) of different applications [11]. The past few years have been dedicated to the upgrades and modifications necessary to achieve a proof-of-concept experiment that produces a high peak and high average flux of monochromatic photons of 10 keV x-rays with $\mathcal{B} \sim 10^{15}$. The instrumentation development laboratory (IDL) at UH also collaborates with the FEL team as they are highly active in design, research, and development of state of the art x-ray detectors. Moreover, the MkV is no more than 20 meters, and in comparison is a low cost machine. MkV has provided many graduate students, including myself, the opportunity to have a hands-on learning opportunity in commissioning of a state-of-the-art system.

1.2   Structure of This Thesis

This dissertation is dedicated to the underlying physics of the above-mentioned light sources. The structure of this document is as follows. In the next chapter, the fundamental process of radiation will be discussed and a mathematical review will be presented. It must be noted that the mathematical descriptions and derivations are somewhat involved, so only those with focus on practical results relevant to our experiment or analysis will be presented. The detailed mathematical derivations are cited for reference and when relevant are reserved for the Appendix. After the theoretical background chapter the dissertation is divided into two parts.

The first part will discuss the proof-of-concept FEL based ICS x-ray experiment currently

underway at UH. We start with the motivation for and the details of the experimental set up. Next, the goals and a set of stringent requirements for the control elements of the experiment for obtaining a suitable electron beam will be presented. The methods that were utilized to achieve these goals and requirements will follow. Finally the results, discussion and future plans will be elaborated on as well as a short summary of the efforts underway at UHM for future x-ray detectors.

As with any experiment, there were many periods of wait and rush for the above mentioned experiment. During one of these wait periods, a review of the fundamental process of coherent radiation became the focus of discussion. As a result of this review and discussion, we demonstrated that a time-symmetric definition of classical electrodynamics, based on Wheeler-Feynman analysis of the interaction of a moving charge with distant absorbers, provides a perfect match to the energy radiated by two coherently oscillating charged particles (a heretofore unsolved problem in classical electrodynamics)[1]. This discussion is presented in the second part of this document and is followed by the analysis and description of its possible applications in antennas as well as current and future FEL based light sources. Finally the concluding remarks and future plans will be presented.

---

[1]This discussion and analysis has been published [15] in collaboration with John Madey and Jeremy Kowalczyk.

CHAPTER 2
THEORETICAL BACKGROUND

Material in this chapter is presented mostly in a chronological order starting from Maxwell's equations. The intention is to provide the reader with a smooth transition while providing all the necessary background information. The references [16, 17, 18, 4, 3, 19, 20, 21] are chosen also with the same intention in mind. The derivations are mimicked closely, providing some skipped steps where necessary, while skipping through irrelevant material when appropriate. Unless otherwise noted the equations are presented in CGS units and we adopt the common curvilinear coordinate description showed in Fig. (2.1).
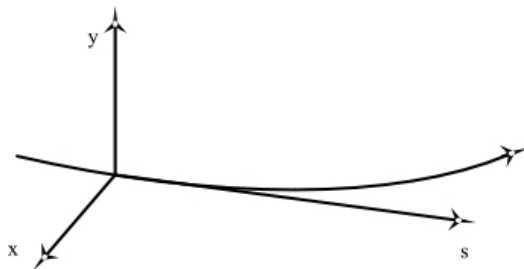
Figure 2.1: Curvilinear coordinates used in this work where the curved line shows the direction of the beam propagation.

2.1   Electromagnetic Radiation

Theory of radiation deals with charged particles in the presence of other charged particles or fields. To describe these systems we use Maxwell's equations:

$$\nabla \cdot \mathbf{D} = 4\pi\rho \tag{2.1}$$

$$\nabla \cdot \mathbf{B} = 0 \tag{2.2}$$

$$\nabla \times \mathbf{E} = -\frac{1}{c}\frac{\partial \mathbf{B}}{\partial t} \tag{2.3}$$

$$\nabla \times \mathbf{H} = \frac{1}{c}\left[4\pi\mathbf{J} + \frac{\partial\mathbf{D}}{\partial t}\right]. \tag{2.4}$$
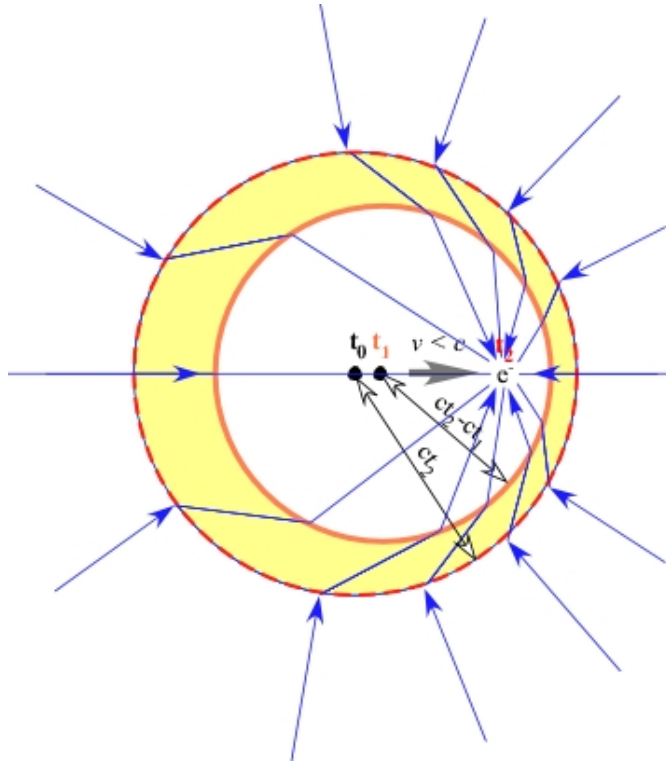
Figure 2.2: Classical description of radiation.

The classical definition of radiation is that radiation is a disturbance carried out to infinity due to the finite speed of light. This is shown in Fig. (2.2). The theory of radiation was developed both in quantum mechanical and in classical terms by Dirac in 1930's. Since the process of radiation involves the two elements of electron and photon, the laws of conservation of momentum and energy governing these two elements determines when/if and how an electron can emit or absorb photon or radiation. A case of particular interest is the radiation in "free space." For this case we will derive Maxwell's energy integral equation. Start with Eq. (2.3) and (2.4) and write:

$$\mathbf{H} \cdot \left[\nabla \times \mathbf{E} = -\frac{1}{c}\frac{\partial\mathbf{B}}{\partial t}\right] \tag{2.5}$$

$$\mathbf{D} \cdot \left[\nabla \times \mathbf{H} = \frac{1}{c}\left[4\pi\mathbf{J} + \frac{\partial\mathbf{D}}{\partial t}\right]\right]. \tag{2.6}$$

7

If we subtract Eq. (2.5) and (2.6) from each other, apply vector calculus and integrate over all volume, we will get the Maxwell's energy integral equation (Eq. (2.7)). We will discuss this equation in detail in Ch. 8. For now just consider Fig. (2.3) which illustrates the volume integral

$$-\int_A^B dt \frac{d}{dt} \int \frac{1}{8\pi} \left[E^2 + H^2 \right] dV =$$

(2.7)

$$\int_A^B dt \left[\int \frac{c}{4\pi} \mathbf{E} \times \mathbf{H} \, d\mathbf{a} + \int \mathbf{E} \cdot \mathbf{j} \, dV \right].$$

We notice that the invariant interval $(cdt)^2 - dr^2$ (covariant distance in space-time separating source/transmitter and absorbers/targets) between the emission of a wave and it's absorption at the target is always identically zero. We will also discuss this matter in detail in part II of this work. Fig. (2.4) demonstrates the general geometry assumed in the devel-
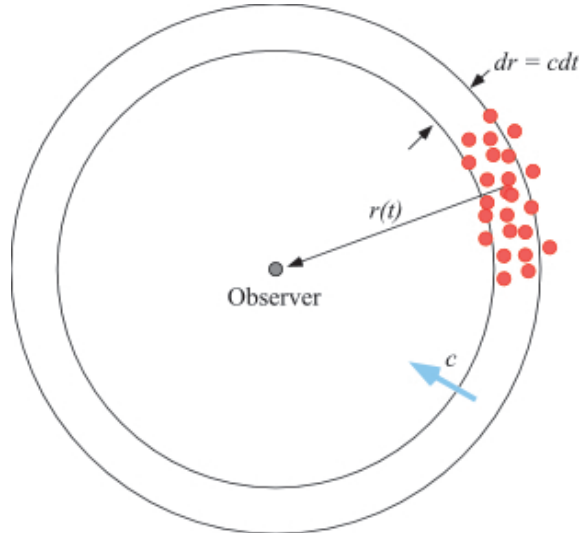
Figure 2.3: The volume integral over all charges.

opment of Maxwell's energy integral. The theorem assumes a periodically oscillating current distribution confined to a volume defined by a closed surface surrounding the oscillating charges with additional fields generated by the oscillating currents in the boundaries outside the surface of integration excited by the radiating charges within the surface. In Ch. 7, we extend this definition to a special geometry assumed in the use of Maxwell's energy integral to test the compliance of the fields generated by synchronously oscillating pairs of charges estimated using the alternative models of electrodynamics including Sommerfeld's, "retarded only," model, Dirac's restricted time symmetric model, and Wheeler and Feynman's fully

time-symmetric model.
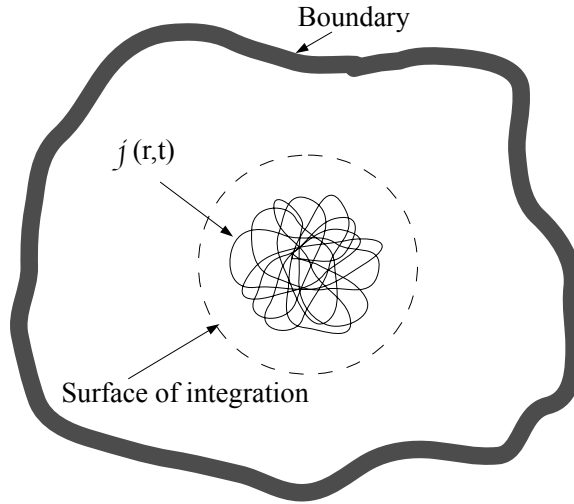
Figure 2.4: An oscillating charged particle surrounded by distant absorber.

2.2 Electron Beam Dynamics

The interplay between particles and fields is called beam dynamics [16]. The evolution of the beam size along the beamline is defined by the β-function. β-function is the characteristic function of a beamline with it specific focusing elements, and depends on the initial β-function value and its derivative.[1]

2.2.1 Equations of Motion

The motion of charge in a electric or magnetic field is given by the energy and momentum relation with the Lorentz force $\mathbf{F} = q\left(\mathbf{E} + \frac{\mathbf{v}}{c} \times \mathbf{B}\right)$. For particle with $\mathcal{E} = \gamma m_0 c^2$ and $\mathbf{p} = \gamma m_0 \mathbf{v}$,

$$\frac{d\mathcal{E}}{dt} = \mathbf{F} \cdot \mathbf{v}, \tag{2.8}$$

and

$$\frac{d\mathbf{p}}{dt} = q\left(\mathbf{E} + \frac{\mathbf{v}}{c} \times \mathbf{B}\right). \tag{2.9}$$

---

[1]Note that β of β-function should not be confused with relative speed with respect to c (speed of light). In part I of this work, β is β-function. In part II, β is the speed.

Since the beam in a beamline travels through magnets with different **B**, lets consider, both a constant and a dipole field. For a constant field the equation of motion becomes:

$$\gamma m_0 \dot{v}_x = q v_y B \quad and \quad \gamma m_0 \dot{v}_y = -q v_x B. \tag{2.10}$$

For a quadruple with gradient Q, $(B_x = Qy, B_y = Qx,)$ the equations of motion will become

$$\ddot{x} = -\frac{q}{\gamma m_0} Q \dot{s} x, \quad \ddot{y} = \frac{q}{\gamma m_0} Q \dot{s} y, \ and \quad \ddot{s} = \frac{q}{\gamma m_0} Q(\dot{x}x - \dot{y}y). \tag{2.11}$$

2.2.2 Basic's of Beam Optics

If we only consider small deviations from s (as in the paraxial approximation) and an ideal beam, we can write the equations of motion as

$$\frac{d^2 y}{ds^2} + K_y(s)y = 0, \tag{2.12}$$

$$\frac{d^2 x}{ds^2} + K_x(s)x = 0. \tag{2.13}$$

These are known as the Hills equations. Solution of Hills equation can be found in form of principle trajectories, which are two particular solutions of homogenous Hills equation and satisfy a certain set of initial conditions. For instance a particular solution C satisfies

$$C(s_0) = 1 \quad C'(s_0) = 0. \tag{2.14}$$

This is a *cos*-like solution. And S satisfies

$$S(s_0) = 1 \quad S'(s_0) = 1. \tag{2.15}$$

This is a *sin*-like solution. Then we can write the general solution as a linear combination of the principal trajectorie:

$$y(s) = y_0 \ C(s) + y_0' \ S(s). \tag{2.16}$$

Also we can write the amplitude $y(s)$ and the angle $y'(s)$ in terms of β and emittance of the beam. Then we will have

$$y(s) = \sqrt{\epsilon \beta(s)} \cos\left(\phi(s) - \phi\right), \tag{2.17}$$

$$y'(s) = -\sqrt{\frac{\epsilon}{\beta(s)}} \left(\sin\left(\phi(s) - \phi\right) + \alpha(s)\cos\left(\phi(s) - \phi\right)\right). \tag{2.18}$$

With some algebra we can find $\beta(s)$ and $\alpha(s)$:

$$\beta(s) = \frac{1}{\beta_0}\left[\frac{S(s)}{\sin\phi(s)}\right]^2, \tag{2.19}$$

$$\alpha(s) = \frac{-S'(s)\sqrt{\frac{\beta(s)}{\beta_0}} + \cos\phi(s)}{\sin\phi(s)}. \tag{2.20}$$

Therefore we can describe evolution of particles trajectories by means of the matrix:

$$\begin{pmatrix} y(s) \\ y'(s) \end{pmatrix} = \begin{pmatrix} C(s) & S(s) \\ C'(s) & S'(s) \end{pmatrix} \begin{pmatrix} y(s_0) \\ y'(s_0) \end{pmatrix}. \tag{2.21}$$

Two particular representations of this matrix, will be important for us in Ch. 5: the focusing quadrupole matrix

$$\mathbf{M_F} = \begin{pmatrix} \cos\left(\sqrt{|K|}L\right) & \frac{1}{\sqrt{|K|}}\sin\left(\sqrt{|K|}L\right) \\ -\sqrt{|K|}\cos\left(\sqrt{|K|}L\right) & \cos\left(\sqrt{|K|}L\right) \end{pmatrix}, \tag{2.22}$$

and the defocusing quadrupole matrices:

$$\mathbf{M_D} = \begin{pmatrix} \cosh\left(\sqrt{K}L\right) & \frac{1}{\sqrt{K}}\sinh\left(\sqrt{K}L\right) \\ \sqrt{K}\cosh\left(\sqrt{K}L\right) & \cosh\left(\sqrt{K}L\right) \end{pmatrix}. \tag{2.23}$$

2.2.3 Phase Space

The spatial quality of a relativistic beam is defined by how well collimated and simultaneously how tightly focused the beam can be configured in applications such as linear colliders or free electron lasers [18]. For a well engineered electron beam the phase space area is often in form of an ellipse. This ellipse is shown in Fig. (2.5) Hills Equations (2.13) and its solutions (2.18), describe evolution of the ellipse shown in Fig. (2.5). The area of this ellipse
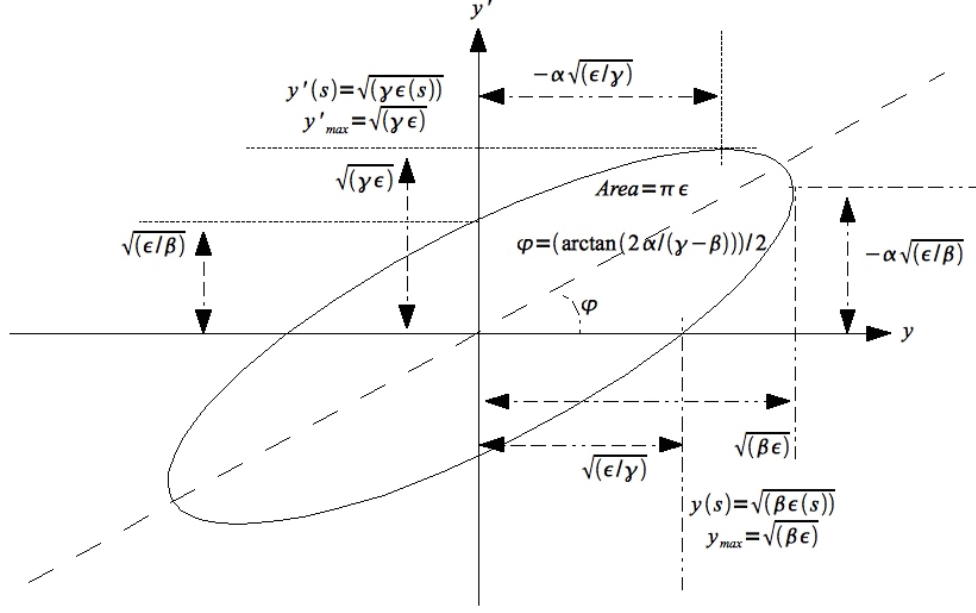
Figure 2.5: Phase space and betatron motion (reproduced from [17]). For a beam at waist (focus) φ would be equal to $\pi/2$.

is invariant and stays constant independent of the optics of the beamline.

$$\beta y'^2 + 2\alpha yy' + \gamma y^2 = constant = \epsilon \tag{2.24}$$

The parameters of Eq. (2.24) (Twiss parameters[2]) can also be represented in form of a matrix:

$$\sigma_y = \epsilon_y \begin{pmatrix} \beta_y & -\alpha_y \\ -\alpha_y & \gamma_y \end{pmatrix}. \tag{2.25}$$

Note that, starting from (2.18), the same is true for the x-direction. For a matrix $\mathbf{M}$ that represents an optical element of the transport line, and σ that defines the parameter of the beam in one plane, the following equation defines the evolution of the beam along the beamline.

$$\sigma(s) = \mathbf{M}\sigma(s_0)\mathbf{M}^T \tag{2.26}$$

This equation is used in the transport simulator module that will be introduced in Ch. 3.

---

[2]Here γ is not the relativistic mass factor but one of the Twiss parameters and $\gamma = (1 + \alpha^2)/\beta$

2.3   Inverse Compton Process

Inverse-Compton light sources, such as the one at UH, operate by colliding high intensity focused and synchronized counter-propagating relativistic electron and optical pulses. Individual electrons propagating as members of the incident electron beam pulse encounter high photon spatial densities in the counter-propagating optical pulse, and absorb, then re-radiate one or more of the individual photons according to the principles of quantum field theory and special relativity. The re-radiated quanta emerge in a $1/\gamma$ cone centered about the electrons' initial vector directions with wavelengths reduced by a factor of $(1 + v/c)^2\gamma^2$ at $\theta = 0$ and shifted slightly to longer wavelengths by their Compton recoils. Both the differential scattering rate and the scattered photon energy are strongly peaked in the direction of the electrons vector momentum [21]. Therefore for small scattering angles θ, the wavelength of the scattered photons is increased by the factor $(1 + \gamma^2\theta^2)$ [22]. If the photons are sent back
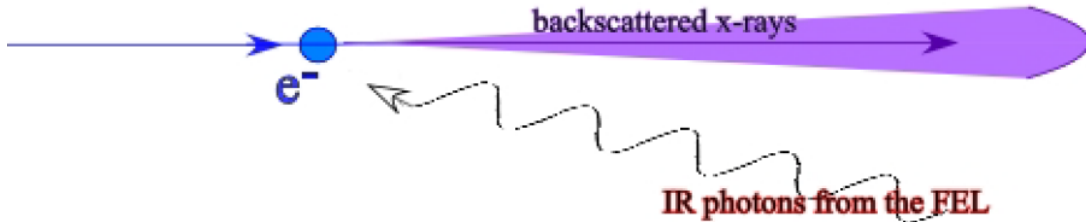
Figure 2.6: Diagram of inverse Compton scattering.

along their original path, the maximum energy of the photons is

$$\mathcal{E}_{\gamma'} \sim 4\gamma^2\mathcal{E}_\gamma. \tag{2.27}$$

For a diffraction-limited optical pulse, with the properties of TEM_{00} gaussian beam or with a beam waist w_0, the probability of a single photon being sent back on its original path is inversely proportional to w_0,

$$\mathcal{P}_{\gamma'} \propto \frac{\sigma_T}{\pi w_0}. \tag{2.28}$$

2.4 Free Electron Laser (FEL) Sources

The free electron laser is a tunable, coherent source for electromagnetic radiation. There are currently a number of active FELs that operate at wavelengths ranging from 1 centimeter to 1 Angstrom (hard x-ray) in the electromagnetic spectrum. In the most basic terms, a FEL transforms the kinetic energy of a relativistic electron beam into coherent electromagnetic radiation [23]. Therefore, in order to get a physical picture for the interactions of an FEL we must find 1) The electron FEL equations (which would depend on the undulator type – planar or helical – and 2) find the equations for the field. There are many different approaches to this and each has different degrees of approximation: 1D, 1D with transverse mode expansion, 3D without energy spread, etc.

For the purpose of this document, its essential to know the focusing properties of the FEL. In the Part I, we will be matching the electron beam to the undulator mode, in order to maximize the lasing power of the MkIII FEL. In part II, we will discuss and present an analytical verification for including the advance fields in the theory of high gain FELs, so here we briefly discuss the field equations for FEL.

Electron Motion in FEL

Matching the electron beam to the FEL in both the vertical and horizontal plane can be obtained from the equation of motion of FEL. In the vertical plane from [18] we have Eq. (2.29)[3],

$$\frac{d^2 y}{dz} = -\kappa^2 y, \qquad \kappa = \frac{\hat{K} k_u}{\gamma} \tag{2.29}$$

with the general solution[4]

$$y(z) = y(0) \cos(\kappa z) + \frac{y'(0)}{\kappa} \sin \kappa z, \tag{2.30}$$

$$y'(z) = -\kappa y(0) \sin \kappa z + y'(0) \cos \kappa z. \tag{2.31}$$

---

[3]here z in the longitudinal axis

[4]here γ is the relativistic mass factor

We notice that the betatron oscillations have a period of $\lambda_\beta = \frac{2\pi}{\kappa} = \frac{\lambda_u \gamma}{\hat{K}}$, with number of oscillation

$$n_{osc} = \frac{L_u}{\lambda_\beta} = \frac{N_u \hat{K}}{\gamma}. \tag{2.32}$$

For the MkV FEL, where $N_u = 47$, $\hat{K}^2 = 1.2$, $n_{osc} = 0.6$. If we chose $y'(0) = 0$, for the elliptical motion of electrons we will have the following aspect ratio:

$$\frac{y_{max}}{y'_{max}} = \frac{y(0)}{\kappa y(0)} = \frac{1}{\kappa}. \tag{2.33}$$

If we want the vertical section of the electron beam to propagate as a collimated pencil beam, the injected phase space distribution must match this value which means that the electron beam must enter the undulator at a waist with

$$\beta_y \equiv \frac{w_y}{\theta_y m} = \frac{\gamma}{\hat{K} k_u}. \tag{2.34}$$

In the x plane or a planer undulator (like the one at UH) the electrons are not effected by the magnetic field of the undulator and will propagate as in free space. To maximize gain, however, we should keep the horizontal radius of the electron beam to a minimum (smaller than the optical radius $\epsilon_x << \lambda$). From equation of motion of particles we can arrive at a set of equations for change in the energy and change in the phase of electrons in FELs and from Maxwell's equations we can arrive at equation of wave in FEL. These three equations will form a complete set describing the rather complicated system of FEL. These equations can be solved analytically for specific cases but for the most general description, numerical codes are used.

Equations of Fields in FEL

Here we use Maxwell equations to find equations for the field. Starting from Eq. (2.4 and 2.4) and write them as:

$$\left(\nabla^2 - \frac{1}{c^2}\frac{\partial^2}{\partial t^2}\right)V = -4\pi\rho \tag{2.35}$$

$$\left(\nabla^2 - \frac{1}{c^2}\frac{\partial^2}{\partial t^2}\right)\mathbf{A} = -\frac{4\pi}{c}\mathbf{J}. \tag{2.36}$$

15

For a more rigorous study we would define the current and charge densities J_e and ρ_e in terms of sums of delta functions but for our study, we just assume a transverse current $J_\perp$ and solve for a complex field amplitude from Eq. (2.36).

$$\mathbf{A} = \mathbf{A_{r,y}} - i\mathbf{A_{r,x}} = i\frac{E(z,t)}{k}e^{ik(z-ct)} \tag{2.37}$$

$$E(z,t) = -iE_0(z,t)e^{i\psi(z,t)} \tag{2.38}$$

where r is the vector position of a single electron in an electron beam. Taking the slowly varying envelope approximation and assuming that the beam that diverges or converges slowly in space (paraxial wave approximation), Maxwell equations for the complex field amplitude become:

$$\left(\frac{\partial}{\partial z} + \frac{1}{c}\frac{\partial}{\partial t}\right)E(z,t) - \left(\frac{\partial^2}{\partial x^2} + \frac{\partial^2}{\partial y^2}\right)\frac{iE(z,t)}{2k} = \frac{2\pi}{c}\mathbf{J}_\perp. \tag{2.39}$$

This will give us the FEL wave equations. It's also important to note that there are two different types of FEL. One the multipass FEL (also cavity FEL) and two the multipass FEL.

2.4.1 Cavity FELs

The cavity FEL shares some characteristics with a standard laser. It has mirrors that would help the build up of resonant harmonic optical amplitude and stores the radiation in the cavity. This design only works at wavelength where we have good quality mirror. The UH MkV FEL is such machine.

2.4.2 Single Pass FELs

In a single pass FEL, the radiation grows within one pass, therefore the single pass machines are much longer than the multipass machines. These machines, when operated in Self Amplified Spontaneous Emission (SASE) would be of interest in the Part II of this document.

Part I

Achieving optimum beam match for production of x-rays in an inverse Compton scattering Free Electron Laser Experiment

CHAPTER 3
OVERVIEW OF THE MKV FREE ELECTRON LASER INVERSE-COMPTON SOURCE

The components of MkV FEL were for the most part developed at Stanford. It was originally identified as the MkIII FEL as it was the third FEL system developed at Stanford. In its days at Stanford, the MkIII performed as a broadly tunable FEL oscillator based on its ability to generate the high peak current, broadly adjustable electron beams needed to achieve high gain, high peak power laser operation in the infrared at an energy of 45 MeV, corresponding to a wavelength of 2.0 microns and proved highly productive as a testbed for both spectroscopic and medical applications, as well as supporting the further exploration of the fundamentals of FEL physics [24]. While the MkIII and other component of the accelerator were being transferred to UHM, different upgrades and control systems were designed for the system to support future research plans. Due to these major upgrades, the system is now called the MkV. A scale drawing of MkV is shown in Fig. (3.1).

3.1   Background and Motivation

The MkV upgraded system is currently in use for the exploration of the physics as well as the research and development associated with Time Encoded Differential Absorption (TEDA) project. This project examines the evaluation of the differential detection technique at x-ray and gamma ray wavelengths. For that purpose the MkV is configured as an inverse-Compton scattering source that utilizes the infrared output of the MkIII FEL to produce photons in the x-ray regime with energies of the order of 10 keV. Utilizing 2.856 GHz drive, the system is capable of producing high brightness photon beams with lower peak power. We discussed in Ch. 2 that the energy of the back-scatted photons in an ICS experiment $\mathcal{E}_{\gamma'} \sim 4\gamma^2 \mathcal{E}_\gamma$, for the set up at UH, $\mathcal{E}_\gamma$ is the energy of the radiation from the FEL laser $(\lambda_\gamma \sim \frac{\lambda_u}{2\gamma_z^2})$[1],

$$\mathcal{E}_\gamma = \frac{2hc\gamma_z^2}{\lambda_u}. \tag{3.1}$$

---

[1]In this work γ as a subscript refers to radiated photon (i. e. $\mathcal{E}_\gamma$ is the energy of the radiation).
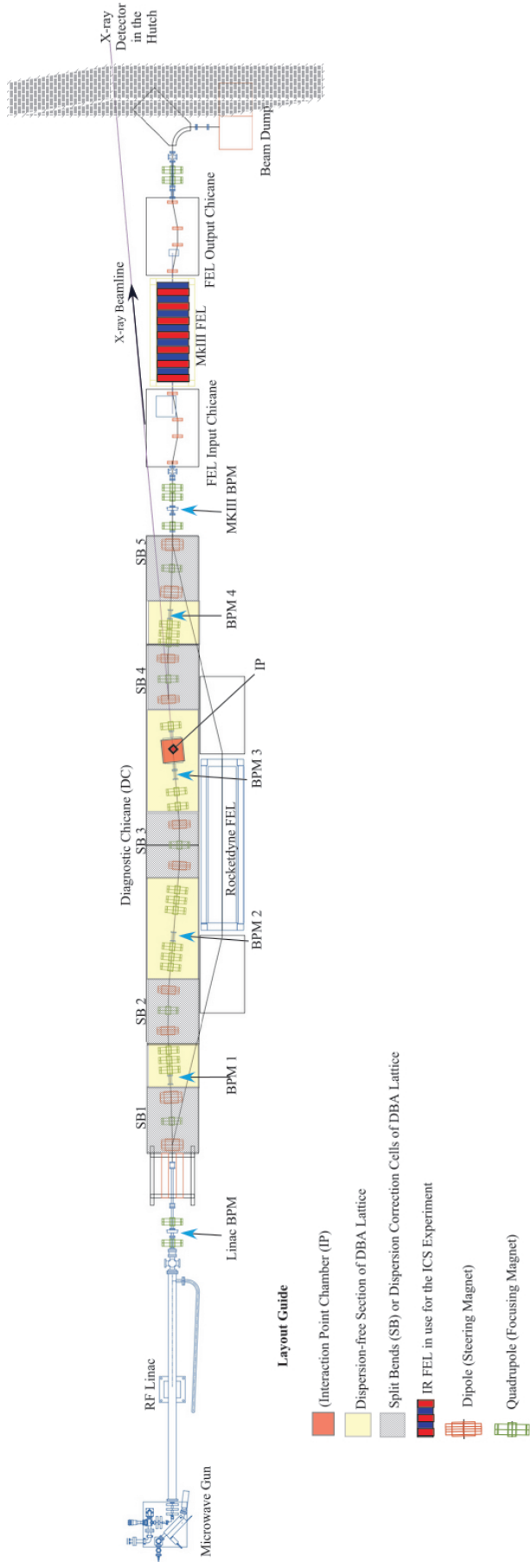
Figure 3.1: Annotated scale drawing of the MkV FEL beamline.

where γ_z is the γ-factor in the electron rest frame in the undulator on the z-axis. Therefore the energy of the photons from our ICS experiment has the following relation:

$$\mathcal{E}_{\gamma'} \sim \frac{8hc\gamma^2\gamma_z^2}{\lambda_u}. \tag{3.2}$$

The power of the x-rays backscattered by the electron beam is then proportional to the above factor and the arrival rate of the electrons. For a strong laser pulse and with an optimized interaction region we can get an estimate of the radiated x-ray photon flux that does not include the coherent effects. As the number of photons becomes large, a strong coherent laser pulse would act like an undulator. In this case, electron beam will micro-bunch which can result in coherent emission. In this case the x-ray brightness may be enhanced by several orders of magnitude [25].

The projected average and peak brightness of the MkV, when fully commissioned, are 10^{14} and 10^{21} $photons/(sec \cdot mm^2 \cdot mrad^2 \cdot 0.1\%BW)$. As a fast high brightness source of x-rays, this set up is particularly valuable for time-resolved, high-resolution, high-contrast crystallography. Additionally, using the FEL as the source of ICS photons provides an excellent advantage over using solid-state lasers. Very complex solid-state lasers are capable of producing multi-terawatt femtosecond pulses, however, at very low repetition rate. A block diagram showing the ICS configuration is shown in Fig. (3.2).
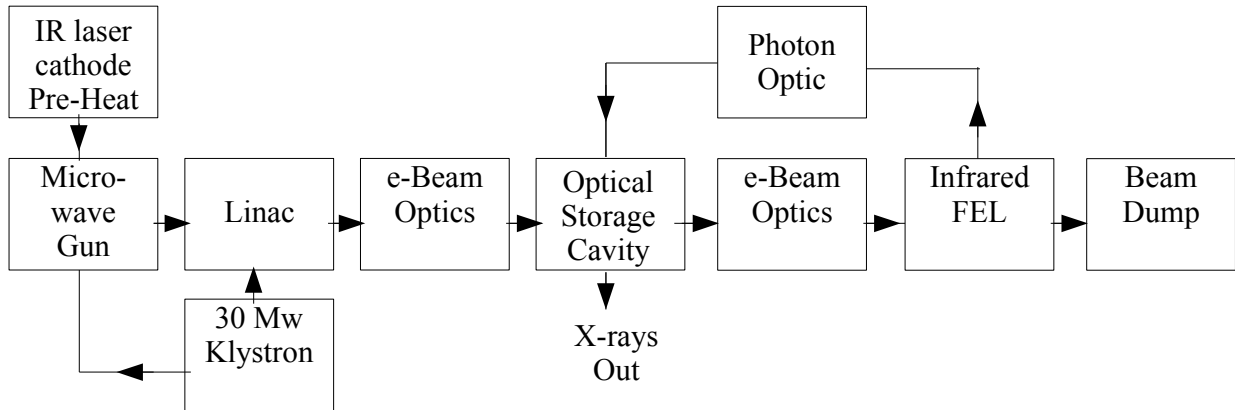
Figure 3.2: Block diagram of the inverse Compton x-ray source with the optical storage cavity at University of Hawai'i Free Electron Laser Laboratory.

3.2   Description of Elements of MkV

3.2.1   Microwave Gun

The MkV utilizes a thermionic Lanthanum hexaboride (LaB_6) cathode electron source in a microwave gun injector. LaB_6 cathodes exhibit 10 times the brightness and more than 10 times the service life of tungsten cathodes. The unique properties of hexaboride crystals provide stable electron-emitting media with work functions near 2.65 eV [26]. This low work function yields higher currents at lower cathode temperatures than tungsten and leads to greater brightness (or current at the beam focus) as well as longer cathode life. The performance and lifetime of the LaB_6 cathode are determined by several factors: vacuum level, cathode temperature, impurity level, crystal orientation, tip shape, and mount design. A careful study of running temperature, reducing the possibility of contamination, and testing several mount design (including a tungsten heater coil assembly) was required for optimum performance of the system. Some of these factors will be discussed in later chapters.

The cathode position can be adjusted using a micrometer stage. The gun cavity surrounding the cathode is an RF resonant structure. The high power RF (1 MV) wave inside the cavity is responsible for striping the electrons from the cathode. After exiting the gun cavity the electrons are focused by a set of focusing magnets [24]. At this point electrons have a kinetic energy between 1-2 MeV. Next they will be transported through an α-magnet which acts as a momentum filter and also provides bunching before the electrons are injected to the linac. The elements of the microwave gun are shown in Fig (3.3). With its capability for operation at high GHz rep rates, high charge per micro-pulse, and low emittance, the microwave gun is perfectly suited for the discussed ICS source. Moreover there are additional upgrades planned that increase the pulse length of the beam from 4.5 μs to at least 8 μs.

Currently, electron beam pulse lengths and energy spreads are limited by a phenomenon known as back-heating of the cathode, where electrons "seeing" a late RF phase would decelerate back toward the cathode and result in an increase in the temperature of the surface of the cathode that will lead to beam loading. The aim of the said upgrade is to use surface cooling due to diffusion by means of a laser to cancel the back-heating effect [27].

3.2.2   Klystron and Linac

A high power ITT Triton 2956 klystron is used to power the MkV FEL's 40 MeV Linac. The 40 MeV S-band RF linear accelerator is used to accelerate the electrons after the alpha
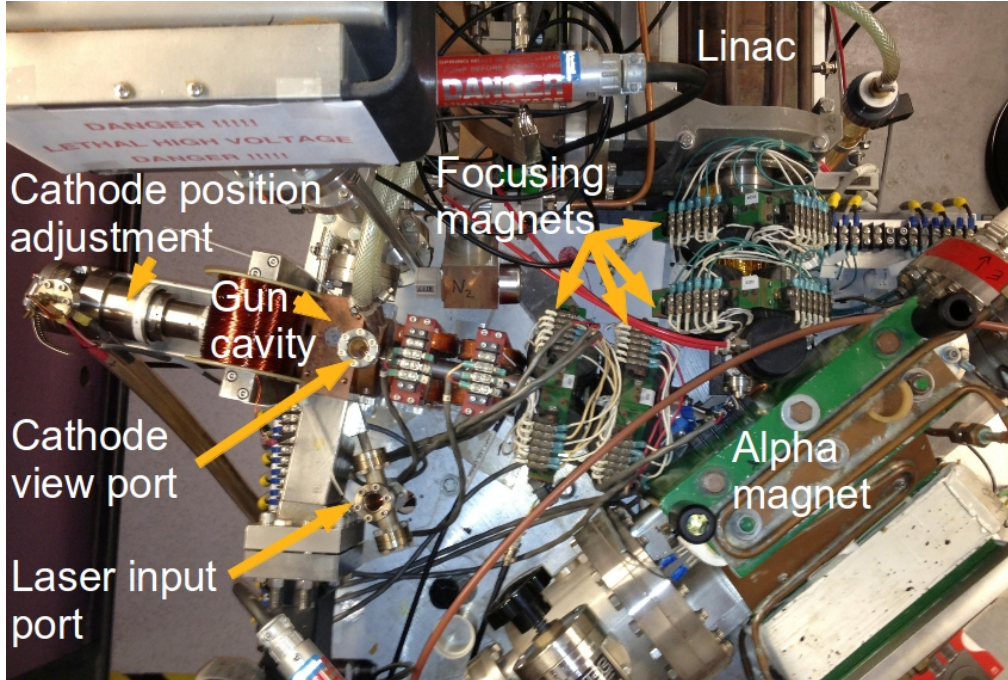
Figure 3.3: Annotated picture of the microwave gun before installation of laser-cooling optics. [Courtesy of J. Kowalczyk]

magnet [28]. The amplitude and phase of the input RF signal is regulated to compensate for any non-uniformity in the complex transfer function of the klystron by a feedforward program written by Mike Hadmack. In the feedforward scheme the compensation is applied to the next pulse, amplitude and phase is measured again and compensation is applied again, going in a loop. This provides the constant desired gain for the electron pulses. The time structure of the beam coming out of the linac is shown in Fig. (3.6). For the ICS project the stability and timing of the electron bunches with the optical pulses is essential. For maximum flux, incoming electron bunches must be synchronized to the circulation time of laser pulses in the storage cavity. For this purpose also the RF carrier frequency is utilized.

3.2.3   Electron Beam Diagnostic Chicane

The beamline transport system at MkV is named electron beam diagnostic chicane or DC. In the context of charged particle beams as well as in FEL physics, the beamline transport system is the array of magnetic elements arranged in between the accelerating section and the interaction point or the undulator. The purpose of the transport system is to deliver a suitable beam to these sections, hence it's often also referred to as the electron beam optics
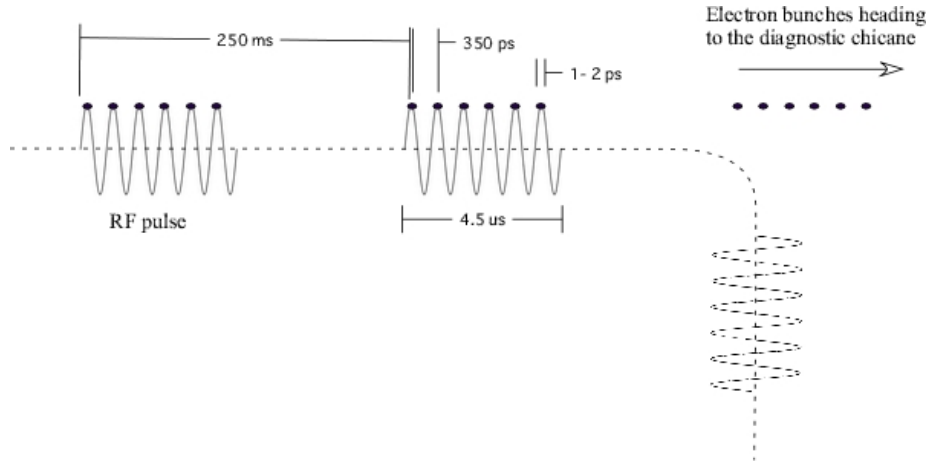
Figure 3.4: Timing structure of the electron micro and macro pulses.

system. In electron beam transport systems containing many bends, the intrinsic momentum spread of the beam can lead to unacceptable beam growth due to dispersion in dipole magnets [29]. The design for DC was inspired by the double-bend achromat, first proposed by Panofsky and then by Renate Chasman and G. Kenneth Green [16] for the bright circulating beam of the National Synchrotron Light Source at Brookhaven National Laboratory (BNL). The Chasman-Green DBA is used in the lattice of many modern synchrotron and storage rings. Alternating the direction of the bend in Chasman-Green DBA lattice design, makes it a suitable design lattice for a linear accelerator. In a circular machine, the bend angels need to add up to 360 °. In MkV DC, the bend angles and drift lengths of the DBA sections are determined by many factors, including the orientation angle of the focusing sections, the availability of space in the lab, and the already built x-ray extraction hole bored through the radiation shielding [29], making the design still a complicated task. The MkV DC lattice was designed and commissioned by Bryce Jacobson. This design consists of a series of five dipole magnets with integrated vacuum chambers designed to deflect the beam through five alternating bends (Fig. (3.5 .b) shows an example with 3 alternating bends). These bends are spaced approximately equally along the section of the transport system (between the linac and the FEL). To accommodate both current and future experiments, spilt bend 1 and 5 use longer dipole magnets that provides additional integrated field. This setup allows for addition of a second beamline for the Rocketdyne undulator. Spilt bend 2,3, and 4 use shorter dipoles. A detailed table is provided in Appendix A. The straight sections of the DC were designed for focusing and diagnostics to be installed along the axis of the beam pipe. The design was also laid out so that it could accommodate the inverse-Compton scattering

23

chamber. The transport system of MkV is therefore a unique setup for our experiment and experiments with similar constraints. In the next chapter we will discuss the control and diagnostics used to utilize DC for the UH ICS experiment.
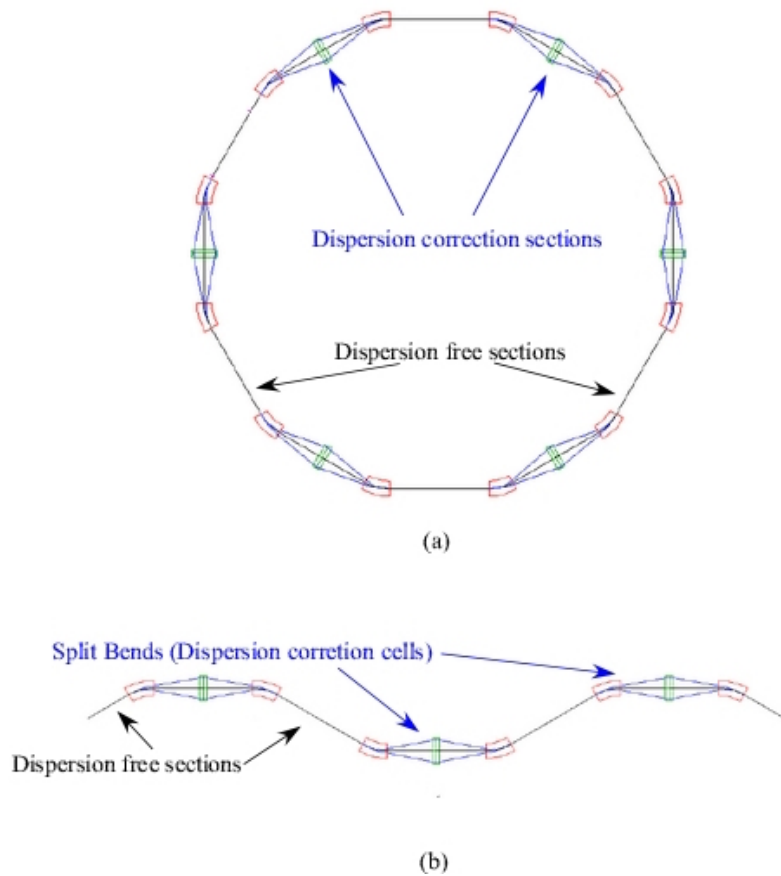
Figure 3.5: Drawing of Double Bend Achromat scheme (a) for a ring (b) for the MkV linear accelerator. A dipole and two quadrupoles form each dispersion correction unit in the ring. The design of the dispersion unit is used in the lattice of the MkV DC. The main difference between the MkV and a ring DBA lattice is that the direction of bends in MkV DC is alternating vs the bends circular rings are in the same direction and have a sum of 360°. [Courtesy of B. T. Jacobson]

3.2.4 Interaction Point (IP)

The scattering chamber was designed and commissioned by Mike Hadmack and installed in the straight section between the DC's third and fourth split bends. Two sets of quad doublet focusing magnets are located before and after the scattering chamber. In the following

chapters, their setup will be discussed in more detail. The vacuum chamber is where the electron beam and the IR laser beam from the MkIII FEL will collide. Originally a copper screen was used as the IP screen. After matching the beam to the microfocus required at IP, however, it was found that the electron beam focused to sub 100 micron easily bored holes through the screen. Therefore a gold plated silicon carbide (SiC) mirror (Moissanite) was grinded and installed as the IP screen. To accurately measure the size and position (as well as overlap with the laser) of the beam, a scanning wire beam position monitor (SWBPM or wirescanner) [30] was also developed and installed by Mike Hadmack at the IP. This system uses a 30 micron diameter graphite fiber (the only wire-like material that did not immediately break due to the intense laser) which is traversed through the focused electron and laser beams at the interaction point. We utilize this tool for setting up the x-ray experiment.
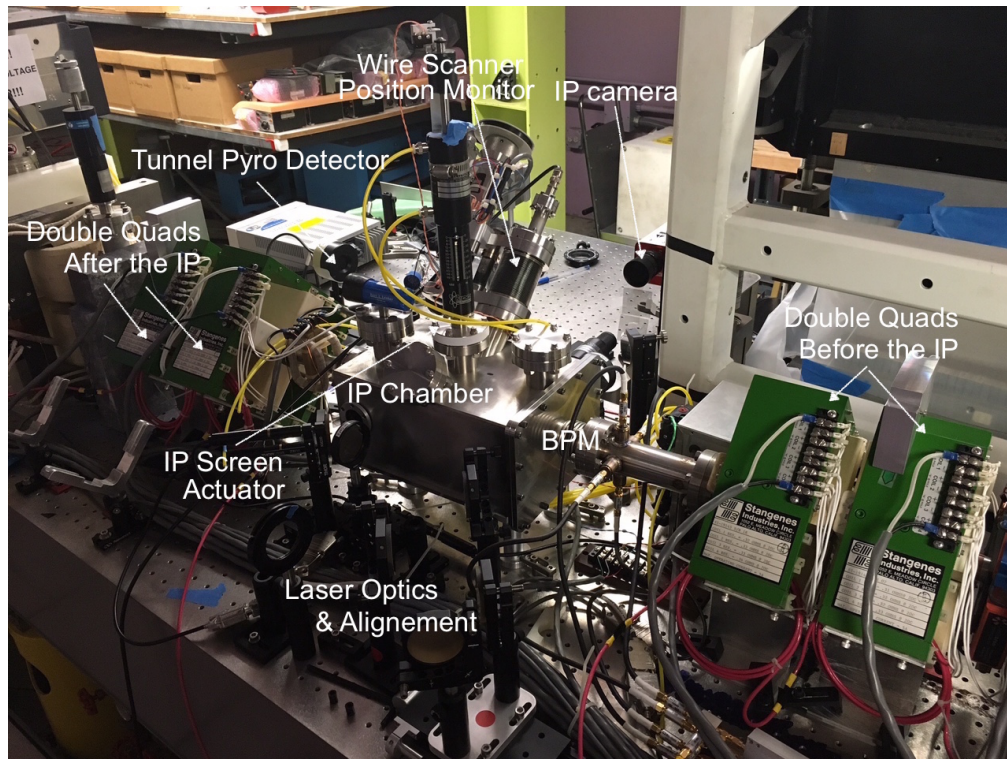
Figure 3.6: The scattering chamber for the ICS experiment.

(a)   (b)
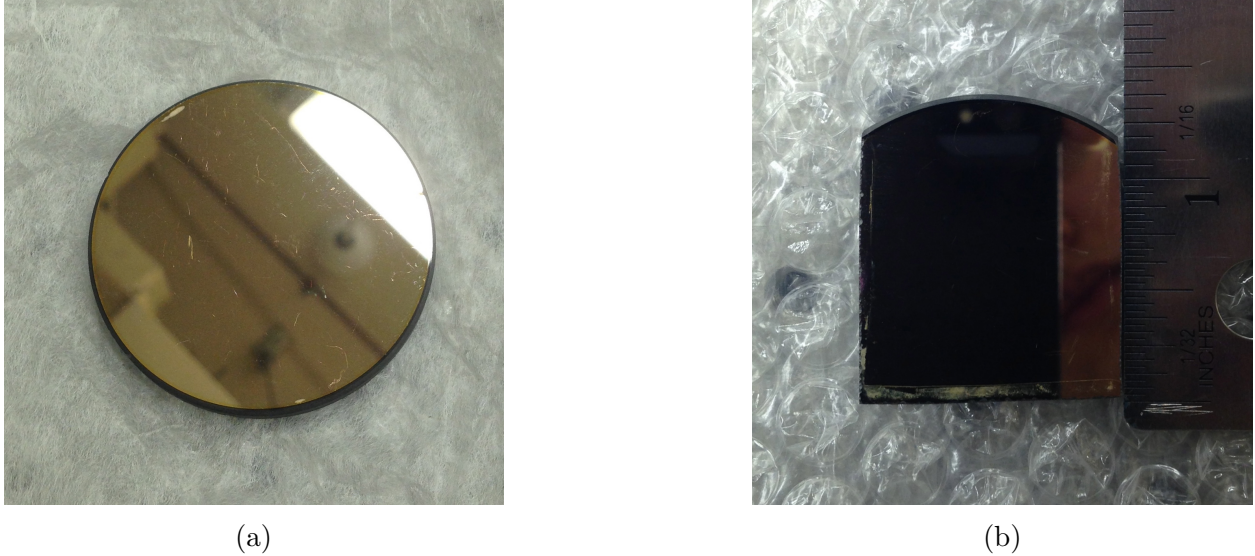
Figure 3.7: A quarter inch SiC mirror was grinded and replaced the copper IP screen. (a) before grinding (b) ready for installation.

3.2.5   MkV Free Electron Laser

As we pointed out earlier, the MkV's Free Electron Laser is the 3rd undulator commissioned at SLAC (the MkIII). The MkIII is now a planer hybrid (using hybrid permanent magnets instead of pure permanent magnets) undulator [31]. The MkIII is designed so that it can work both as an amplifier and as an oscillator. Currently the MkIII is in oscillator mode and set as a quasi-CW mode-locked laser producing 6 mJ, 4 μs macro-pulses at 4 Hz with 1 ps micro-pulses spaced 350 ps and mode-locked at 2.856 GHz. Four different Brewster plates are incorporated for delivering the out-coupled laser beam. The undulator wavelength ($\lambda_u = 2.3$ cm and the number of undulator periods (N_u) is 47. For the ICS experiment, the MkIII offers an optimal compromise, although it has lower average power than the single shot TW laser, its 3 GHz micro-pulse repetition rate of coherent micro-pulses of the mode-locked FEL is highly suitable for utilizing an optical resonator to further enhance the peak power available for x-ray generation.

3.2.6   Optical Storage Cavity

The optical resonator (optical storage cavity) introduces great enhancement of optical power as a result of many coherent optical pulses with high repetition rate interfering constructively and it is now widely recognized that the intensity and brightness of inverse-

Compton x-ray light sources can be enhanced through the use of a high finesse optical storage cavity [22]. Since the Compton backscatter cross-section is small, the electron beam does not deplete the field in an optical cavity significantly and there is a minimal cavity loss due to the electron beam. The mechanism of implementing such optical cavity is however still under study. A 4 mirror design cavity was recently tested at UH by Mike Hadmack and is planned to be commissioned in the near future.

Table 3.1: MkV FEL Based ICS Experiment Parameters.

Symbols	Parameters	Values or Range	Units
RF / Electron Pulses			
f_{RF}	RF Frequency	2.856	GHz
T_{RF} / T_e	Macropulse Spacing	350	ps
I_{mp}	Macropulse Current	~ 170	mA
τ_{mp}	Macropulse Duration	4-8	μs
f_{mp}	Macropulse frequency	4-10	Hz
$I_{\mu p}$	Micropulse Current	30-60	A
$Q_{\mu p}$	Micropulse Charge	60	pC
$\tau_{\mu p}$	Micropulse Duration	1-2	ps
$\mathcal{E}_e$	Electron Beam Energy	35-45	MeV
Laser Pulses			
λ_0	Laser Wavelength	3	μm
$\mathcal{P}_l$	Laser Power	8-16	MW
Interaction Point			
w_0	Beam Radius	30-100	μm
$\mathcal{F}$	Storage Cavity Finesse	2000*	
$\mathcal{P}_s$	Stored Optical Power	$\sim$16*	GW
Scattered X $-$ rays			
$\mathcal{E}_\gamma$	X-ray Energy (Max)	10	keV
λ_γ	X-ray wavelength (Max)	1	Å
$\mathcal{P}_\gamma$	X-ray Average Power	1*	W
$\mathcal{B}_{ave}$	Average Brightness	10^{14}*	$\frac{photons}{sec \times mm^2 \times mrad^2 \times 0.1\% BW}$
$\mathcal{B}_{peak}$	Peak Brightness	10^{21}*	$\frac{photons}{sec \times mm^2 \times mrad^2 \times 0.1\% BW}$

*predicted values

CHAPTER 4
CONTROL AND DIAGNOSTIC ELEMENTS

In the last chapter, a short description of the main elements of the MkV for the ICS project was presented. The objective of the following two chapters is to describe what was done to achieve a beam quality that is suitable for the ICS setup. In order to achieve these objectives, several main diagnostic or control elements had to be set up appropriately. As stated earlier the majority of DBA-based beamline was commissioned. Also beam position monitors (BPM) and transition radiation monitors (TR screens) were physically installed on the beamline, however they were not set up appropriately for use. The following needed to be completed:

1) BPM readout boards,

2) BPM software interface,

3) Precise positioning and calibration of the TR screens, cameras and mirrors, and

4) A simulation module for better understanding of the beamline transport system.

The last item is of great importance for efficient use of the MkV. Then a rigorous study was performed to find a matched solution for operation of the FEL as an inverse Compton source.

4.1   Requirements for the E-Beam

4.1.1   Microfocus

As we discussed in Ch. 2, the probability of a single photon scattered by ICS increases as the electron beam radius (w_0) gets smaller. Therefore it is essential to focus the beam to a waist at the IP. At the same time, since the same beam will be driving the FEL, over focusing the beam at the IP must be avoided to ensure non-linear and undesirable effects are not introduced. As we will describe in Ch. 5, we studied this problem by means of simulation and then from the intuition gained based on the simulations; We present a simple yet elegant and effective solution that can be described by ray optics. Additionally, the electron beam must be centered on the DC's longitudinal axis in order for the photon and electron beam to collide with maximum cross section.

4.1.2   Match to the Undulator

Operation of the FEL depends on the ability of the electron beam to deposit energy in the laser field, therefore electron beam must match the optical mode of the FEL both spatially and temporally. Consequently, maintaining a well focused beam is critical. One advantage of the DC is that it can accommodate the temporal match by means of canceling the dispersion caused by off-energy electrons in the split bends. For the spatial match, we have the following two requirements: 1) the optical mode and the electron beam must be aligned horizontally and vertically (in other words, share a common axis) and 2) they must also have the same phase-space configuration (transverse size and angular spread) throughout the undulator. These requirements can be met by the suitable diagnostic and control elements which will be reviewed here.

4.2   Diagnostic and Control Elements

4.2.1   Beam Position Monitors (BPMs)

Both microfocus and match to the undulator requirements of the electron beam demand a well centered beam. To that end, one of the upgrades for MkV when it was being relocated to Hawai'i was the design and development of the electronics needed to measure and record the transverse position of the electron beam as it moves through the DC, especially the measurement of the electron beam transverse position for injection into the x-ray IP chamber and the FEL. Two varieties of BPMs are installed along the MkV beamline, a wall current type and a strip-line type. There are two wall current BPMs on the beamline: one is placed between the linac quads (before the DC) and the other is placed before the MkIII undulator (after the DC). The DC is constructed to include a series of periodically spaced (SLAC-type) [32] strip-line beam position sensors. The wall current BPMs carry induced wall current at four cardinal positions around the beam pipe with a minimum of temporal distortion to a 4-port connector block. The placement of these BPMs is important for their optimal performance. The strip-line BPMs consist of a stainless steel body with four copper electrodes oriented with $\pi/2$ symmetry. Both BPMs are shown in Fig. (4.1).

The high 3 GHz repetition rate and high macropulse currents of the electron beams passing through the SLAC strip-line BPMs provide signal levels and good sensitivity to the displacement of the beam centroids. The transmission of the 3 GHz signals to the control room, however presents a problem due to attenuation in long cables. To avoid this

difficulty, the BPM readout system utilizes heterodyne mixing of the raw BPM outputs in order to convert the strong 2.856 GHz signal to the more manageable HF Band. The readout strategy is to mix the BPM signals with a local oscillator RF reference in the accelerator vault, resulting in an intermediate frequency (IF) between 10 - 20 MHz. The IF signal from each output port of each BPM is carried through long runs of LMR-400 coaxial cable from the accelerator vault to the operator control room. The Analog Devices AD640 logarithmic amplifier serves as both the detector used to measure the mixer outputs for each BPM port as well as the means to provide calculation. Each BPM port goes through a 10 dB attenuator and then a band pass filter ensures that no higher order harmonics (for strip-line BPMs only) and other frequency components down to DC (for wall current BPMs only) enter the doubly balanced mixer. Any high frequency leakage out of the mixer is blocked by a low pass filter on the mixer IF port mentioned above. This system operates at 10 MHz and allows use of the integrated logarithmic amplifiers. PCB boards for the system were designed by Bryce Jacobson and hold the logarithmic amplifiers, analog signal comparators, and sample and hold circuits for extracting the beam position signals for the time interval of interest. These boards were assembled, troubleshooted and installed in a small general-purpose commercial rack. A software program with a graphical interface BPM-GUI was developed for this setup.

(a)   (b)
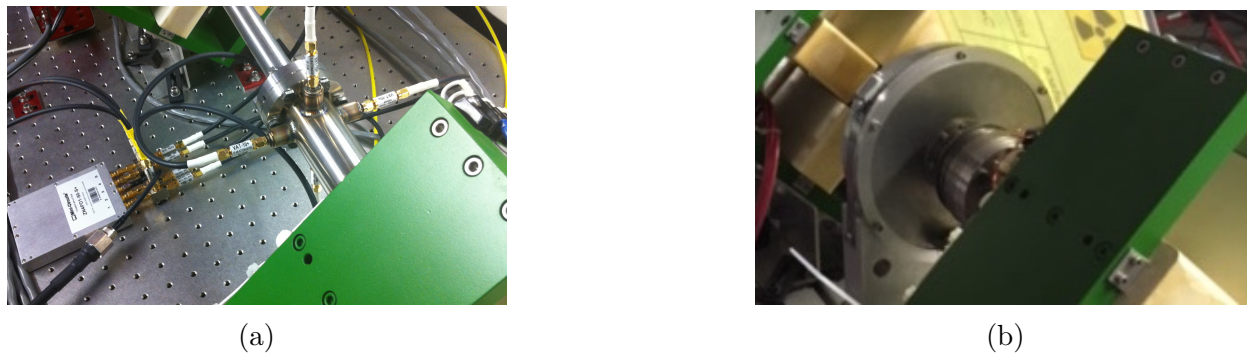
Figure 4.1: Different types of BPM installed on the MkV beamline (a) strip-line (b) wall current.

The purpose of the Beam Position Monitor Graphical User Interface (BPM-GUI) is to provide an interactive tool for the BPM Hardware and Software system. The BPM system reads the beam offsets, in both x and y direction, as positive or negative voltages. The BPM-GUI displays these voltages. The person operating the accelerator can use the BPM-GUI readout to center the beam by zeroing the readouts. The BPMs are connected to a LabJack UE9 hardware for signal transformation. The LabJack UE9 has 14 AIN channels (analog

inputs) on its DN37 connector. Twelve of these channels are used to read the horizontal and vertical voltage differences forwarded from each BPM. The nominal input range for the AINs is +/-5 volts. When using several channel at once there is a 12 microsecond delay for 12 bit-streaming from channel to channel. The pulse rate in the accelerator is 5 Hz. For accurate readouts, the BPM-GUI is set to read every 100 ms (meeting the minimum of 2 readout per cycle). Hence the delay in the channel readouts can be neglected. Therefore, the LabJack software (LabJackPython) was implemented in the GUI code written in wxPython to provide the first version of BPM-GUI. Currently, the BPM-GUI only provides the readout for each BPM in volts (using read only display text boxes). The button "Read Once" retrieves the voltages only once as a test at the start of the run and the "Read Continuously" retrieves and displays the voltages until the program is stopped. The "Restart" button zeroes all the entries and is only functional when the program is not in continuous run mode. The "Exit" button stops the reading and closes the BMP-GUI [32].

Beam Position Monitor Interface

	Horizantal	Vertical
BPM1	2.8393579549	1.7795645534
BPM2	1.1677121645	0.6922440505
BPM3	0.5633671670	0.2530616610
BPM4	0.1692291251	0.0340960822
BPM5	0.0003128214	-0.010948265
BPM6	-0.010948265	0.4870420224

Read Once   Read Continuously   Reset   Exit
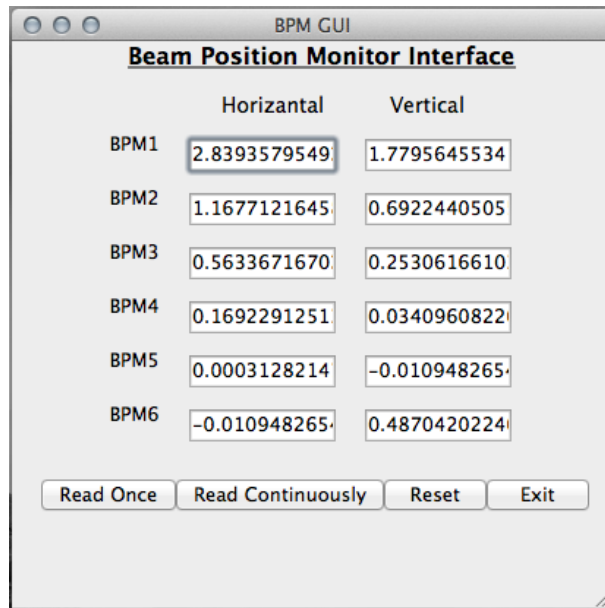
Figure 4.2: Screen shot of BPM GUI display.

4.2.2 Beam Profile Monitors (TR Screens)

The welded form of the dipole magnet vacuum chambers accommodates viewports and in-sertable screens to image the beam's spatial profile at each dipole. The electron beam's spatial profiles is visualized through the synchrotron or transition radiation that was emitted at each dipole. Images are recorded at each of these dipoles are archived in the LABVIEW

31

program. To obtain images with linear representation of brightness intensity, silicon target vidicon camera's were setup as shown in Fig. (4.3) for split bend dipole magnets (other screens have one less mirror). These setups were carefully calibrated as they are used for finding beam parameters. Although the vidicon cameras have high tolerance in high radiation fields, they often have to be repaired or replaced. After each repair or replacement, the calibration of the screens is essential. Table. 4.1 shows the values for the latest calibration by means of images shown in Fig. (4.4). Each fiducial marks 0.1 inch and the mirrors are tilted by 45 degrees so a factor of $\sqrt{2}$ is included.
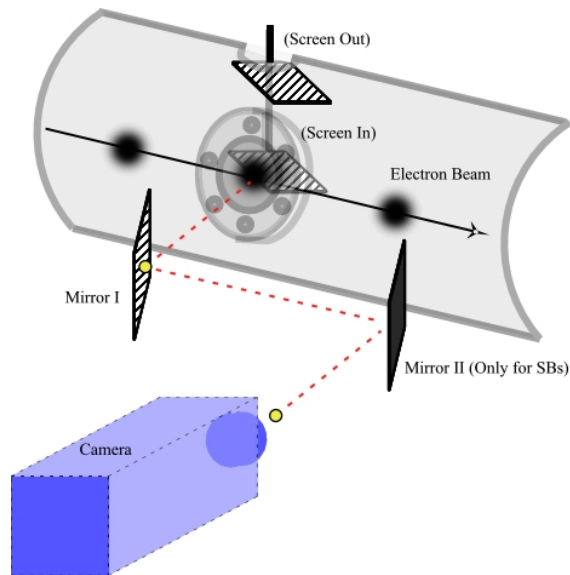
Figure 4.3: Schematic of the transition radiation screen set ups in the split bends.

Table 4.1: Example of Calibration Values for TR Screens.

Screen Name	Pixels per mm (H)	Pixels per mm (V)
SB1	24	22
SB2	16	15
SB3	15	16
SB4	17	16
SB5	10	13
$\pi/2$	16	18
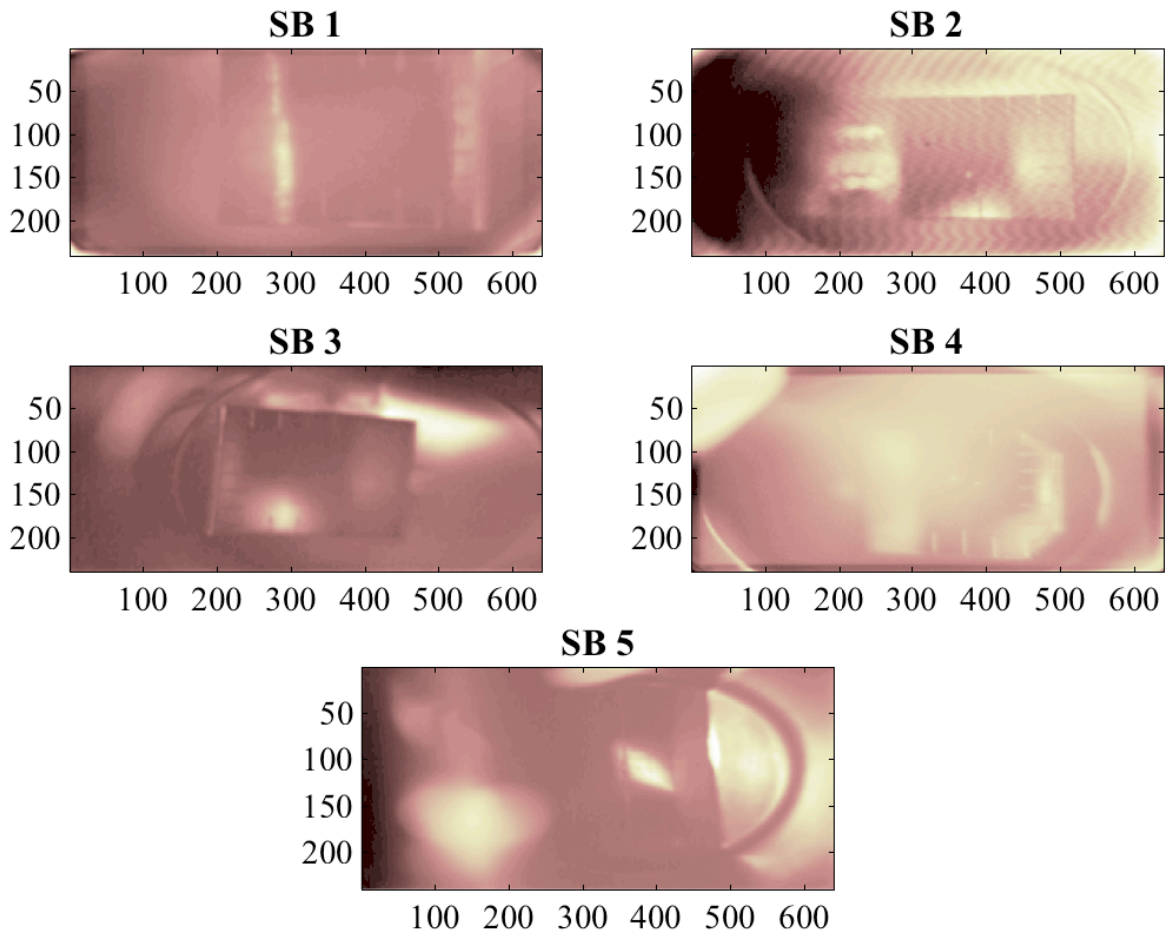
Figure 4.4: Images used to calibrate transition radiation screens along the DC.

4.2.3 Transport Simulation Module

In Ch. 2, we briefly discussed how a beamline like DC can be described in terms of matrices. Although the matrix for DC is known, as it is a linear system without periodicity of a ring, it can not give us a real analytical solution that describes the beamline. Prepackaged simulation codes are often used to describe such beamlines, but in our case, due to the high number of elements and constraints, this becomes a nonlinear problem. If the system is not being operated close to the set configuration by the simulation, it would not be easy to find a stable solution. For this reason, one of the most important diagnostic and control elements on MkV is a computer-based beam transport simulator module (TSM). The TSM gets its inputs from the power supplies that provide the currents to the quadruples installed along the diagnostic chicane and, given a set of initial beam parameters, it can estimate the electron beam's evolution through the DC. The original code was written with the help of Bryce Jacobson who had designed the DBA-based DC.

The structure of this code is as follows: The shunt voltages from the power supplies feeding the ADCs in the control room is read (10 times) and averaged, then the offset value is subtracted and the shunt voltage is scaled. The beam is defined by its energy, input normalized emittances, and α and β in both x and y coordinates. The undulator is defined by the undulator parameter ($\hat{K}^2$). The transport line is defined as one big matrix. The elements of this matrix are the D = drift, Q = quad, B = sector bend, E = bend edge, S = screen marker and U = undulator. An array for each type of element is defined that pins the location and, if applicable, angle of each element. Then the sigma matrix for the beam and the machine matrix for each element is calculated. Finally beam parameters for each screen location is evaluated using the beam and machine matrices. The output of a TSM run is shown in Fig. (4.5)

This system was bench-tested against TRANSPORT code and had good agreements. The main advantages of this system is that the settings of the beamline quads is entered directly in the model and it is possible to create both a 2D beam profile and a fairly accurate 4D phase space distribution at the locations of interest along the beamline. Further capabilities added to the model to estimate the Twiss parameters out of the linac (based on a focused beam in the $\pi/2$ screen by means of the linac quads.) Another advantage of this module is offering the operators a chance to perform "computer experiments" to get a better feel for the capabilities of the physical beamline. With the help of the well calibrated TR screens, the values for the Twiss parameters could be tested and verified. Additionally this approach proved to be more reliable than the conventional quad scan. This interactive model was to
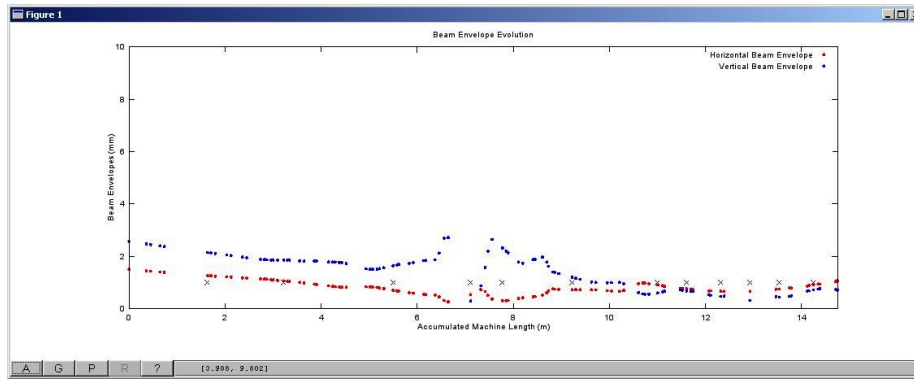
Figure 4.5: Output of the TSM showing a prediction of a microfocus solution envelope evolution.

prove invaluable, both to the development of models for beam transport through the system and for training of operators who could then use the model to better understand how the focusing and defocusing quads installed along the beamline affected the profile of the beam and led to the beam spots they could see on the system's transition radiation screens when operated with a real electron beam [24].

Eliminating Residue Field in Dipole Magnets

During both simulation and operations of the beamline, it became clear that the iron cores of all of the beamline quads held some residue field. To obtain a usable reproducible setting these fields needed to be canceled before each setup. When only a few quads were in use, this was done manually. As the settings became more complex, this process was automatized. We used a single length of number 10 building wire and wrapped a 5 turn coil around the bottom/left sides of the iron cores for each quad. Now before each set up we use a 100 watt subwoofer amplifier to drive up to 12 amps of current at 10 Hz through the number 10 wire. This method has reduced the measured residual fields in the air gaps of the quads to a fraction of a gauss. This modification ensures the reproducibility of the beam profiles with the recorded magnet setting which is crucial for finding reliable setups in advance of a run or reproduce a successful run.

Estimating Beam Parameters

A mathlab code was prepared that reads the TR images and measures the FWHM horizontal and vertical values for the recorded spots. A shorter version of the beam transport module was written in matlab to take the TR screen images for a run with a vertical focus

35

and horizontal minimum (the reasoning for this will be explained in the following chapter) on the IP to find the Twiss parameters introduced in Ch 2. Every time the cathode position is changed or the cathode is replaced this process has to be repeated. If the cathode is unchanged, we would only look for new Twiss values if the spectrum or other identifying parameters of the RF or gun have changed. Table 4.2 and 4.3 shows sets of selected beam parameters in horizontal and vertical plane that were determined based on the TR images collected from the MkV during runs.

Table 4.2: Beam Parameters in the Horizontal Plane.

	Collimated Beam	May 2013 [1]	March 2014 [1]	March 2014 [2]	Units
ϵ_x	0.35	0.25	0.20	0.20	$\pi \cdot mm \cdot mrad$
α_x	0.0	1.0	3.25	0.3	
β_x	3.0	9.0	3.4	5.8	mm/mrad

1: New cathode,   2: Same cathode,   at new position

Table 4.3: Beam Parameters in the Vertical Plane.

	Collimated Beam	May 2013 [1]	March 2014 [1]	March 2014 [2]	Units
ϵ_y	0.15	0.55	0.28	0.28	$\pi \cdot mm \cdot mrad$
α_y	0.0	1.3	-1.9	-3.535	
β_y	3.0	12	10	3.4	mm/mrad

1: New cathode,   2: Same cathode,   at new position

CHAPTER 5
ANALYSIS AND MEASUREMENTS

The control and diagnostics discussed in the last chapter (and those previously installed on the beamline by other members of the UH FEL Lab) proved reliable and effective in finding a match for the electron beam going through the DC with a microfocus at IP and producing a 6 mJ coherent IR laser pulse in the FEL for the purpose of the ICS experiment. Data presented here was taken in the interval of October 2012 to February 2016. The data between October 2012 till May of 2014 were dedicated to the installation and calibration of the diagnostic tools, leading to the first detection of x-rays in May 2014. The remaining data demonstrated the efforts taken to maximize performance of the system.

In the next two chapters, we will discuss the studies of essential design elements and necessary modification as well as the preliminary results of the x-ray measurements. To verify the effectiveness of the solution in practice, as well as its compatibility with other designed and commissioned elements of the ICS experiment at UH's MkV, a few different x-ray analysis codes are prepared and used. As the detected x-ray flux was lower than expected, a thorough study of the x-ray transport from the IP to the hutch detector is performed. The expected PMT high voltage for estimating the total flux is calculated and is presented in a later section of this chapter. In the next chapter we will discuss different elements that were or could have been responsible for the low recorded flux.

5.1   Qualitative Discussion

Based on what we shortly discussed and the theoretical background presented in Ch. 2, we can conclude that, in an ICS experiment, it is possible to optimize the x-ray flux (with some limitation) by adjusting laser power, electron beam current, and focal parameters of the beams. In the ICS experiment at UH, both focal parameters and the laser power are controlled by the match to the beamline requirement. Therefore obtaining the match plays an important role in the experiment. The alignment requirement for the beam is discussed in detail in [31] and accomplish using the vertical and horizontal correctors and the chicane magnets. Although setting up for an experiment involves carefully adjusting the vertical and horizontal correctors to keep the beam centered along the beamline and at the microfocus, these requirements do not introduce any additional constraints to the beamline

design. Therefore, they will not be discussed here.

The dispersion-free sections of the DC have sets of doublet or triplet quadrupoles. In total, there are 23 quadrupoles. The most important quads for our purpose are the two doublets before and after the IP. The placement and excitation of these doublets, and of the other quadrupoles along the DC, has to be chosen to meet the beam size requirements discussed earlier. 1) The electron beam's distribution in phase space at the output of the linac has to be matched to a microfocus at the center of the scattering chamber, 2) the propagated beam's phase space distributions from the microfocus has to match to the vertical and horizontal distributions in the undulator of the downstream FEL. Therefore, the two chicane screens must have beam spots of identical size and distribution. Different settings were simulated and studied so that a better understanding of suitable parameters could be obtained. This understanding led to a simple, yet elegant, and effective solution.

The design and development of the electron beam focusing system required to bring the electron beam to a sub 100 micron optimum focus at the plane at which the electrons were to collide with the counter-propagating optical pulses from the system's laser light source. At the same time we needed to maintain a match to the undulator. The most simple solution was one that focuses the beam coming out of the 3rd split bend to a sub 100 micron spot and returns the beam to its original phase-space (or as close as possible) before the split bend 5. Here original refers to the case without the microfocus. We already had two sets of double quads before and after IP. These quadrupoles were not installed symmetrically and resulted in inadequate match for in the undulator and ultimately scalloping.

5.2   Mathematical Model

Although the TSM provides a cooperative tool for studying the complex beamline at UH, still it has many degrees of freedom. To approach and solve a problem using the TSM most effectively, it is essential to have a simple yet suitable mathematical model in mind. Here we introduce such model for the UH, ICS experiment. To obtain a match for the experiment, we first reintroduce then use the formulas that were presented in Ch. 2. It must be noted that one major benefit of the TSM is that it reduces the need for including the higher order corrections of the system in any analysis. In all cases of study we were able to solve the problem by only including first order approximations and by using the thin lens model, then minor adjustments were introduced when the system was setup. In every case, the predicted values were reasonably close and we were able to work toward the required setting. For the

microfocus, we start from the quadrupole matrices. For quadruples with a width of D,

$$\mathbf{M_F} = \begin{pmatrix} \cos\left(\sqrt{|K|}D\right) & \frac{1}{\sqrt{|K|}}\sin\left(\sqrt{|K|}D\right) \\ -\sqrt{|K|}\cos\left(\sqrt{|K|}D\right) & \cos\left(\sqrt{|K|}D\right) \end{pmatrix} \tag{5.1}$$

and

$$\mathbf{M_D} = \begin{pmatrix} \cosh\left(\sqrt{K}D\right) & \frac{1}{\sqrt{K}}\sinh\left(\sqrt{K}D\right) \\ \sqrt{K}\cosh\left(\sqrt{K}D\right) & \cosh\left(\sqrt{K}D\right) \end{pmatrix} \tag{5.2}$$

can be reduced to

$$\mathbf{M_F} = \begin{pmatrix} 1 & 0 \\ -|K|D & 1 \end{pmatrix} \tag{5.3}$$

and

$$\mathbf{M_D} = \begin{pmatrix} 1 & 0 \\ KD & 1 \end{pmatrix}. \tag{5.4}$$

Now consider the case illustrated in Fig. 5.1. This arrangement focuses the beam in both planes after splitbend 3 and, if the K, D and L (distance between the focusing and defocusing quad) values are chosen correctly with in the beamline geometry, we can bring the beam back to its original (without the microfocus) dimensions before split bend 5. In each plane, we can describe the beam evolution in two sets (one set for each doublequad):

$$\mathbf{M_{tot}} = \begin{pmatrix} 1 & 0 \\ -|K_1|D_1 & 1 \end{pmatrix}\begin{pmatrix} 1 & L \\ 0 & 1 \end{pmatrix}\begin{pmatrix} 1 & 0 \\ K_2 D_2 & 1 \end{pmatrix} = \begin{pmatrix} 1 - \frac{L}{-|K_1|D_1} & L \\ \frac{1}{(KD)'} & 1 + \frac{L}{K_2 D_2} \end{pmatrix} \tag{5.5}$$

Where $(KD)'$ is the effective focal distance of the set:

$$\frac{1}{(KD)'} = \frac{1}{|K_1|D_1} - \frac{1}{K_2 D_2} + \frac{L}{(K_2 D_2)(|K_1|D_1)}. \tag{5.6}$$

Since the width of all quadrupoles is identical, the last expression reduces to

$$\frac{1}{K'} = \frac{1}{|K_1|} - \frac{1}{K_2} + \frac{L}{K_2|K_1|}, \tag{5.7}$$

and when $K_1 = K_2$, the doublet is focusing in both planes. This satisfies half of our requirements: getting the microfocus. To get the beam back to its original dimension, we need to incorporate another constraint. Consider the second set of quadrupoles in the same

plane, again we need

$$\frac{1}{K''} = \frac{1}{|K_3|} - \frac{1}{K_4} + \frac{L}{K_4|K_3|}, \tag{5.8}$$

to have focusing in both planes. We also need K'' to be as close as possible to K'.
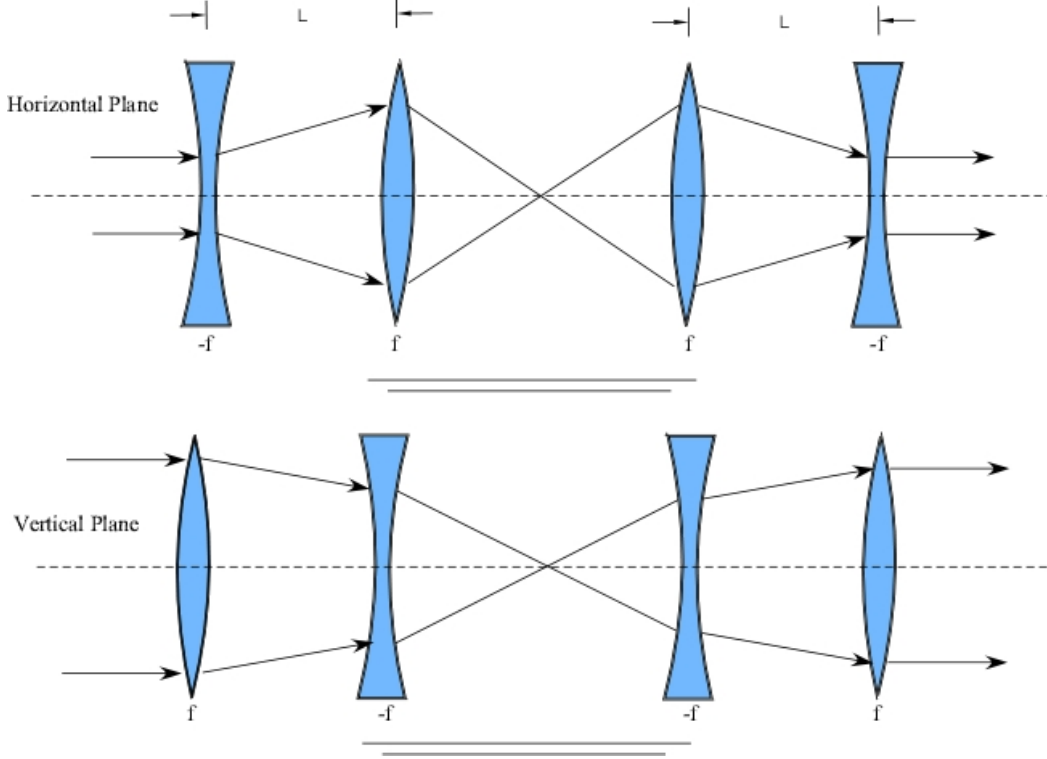
Figure 5.1: Using ray optics to demonstrate model for the doublets around the IP (Quad 1 through 4 from left to right with K_1 to K_4).

In Ch. 2, we discussed the requirement for the vertical and horizontal match to the undulator: $\beta_y \equiv \frac{w_y}{\theta_y m} = \frac{\gamma}{\hat{K}k_u}$, and $\epsilon_x << \lambda$. The first relation can be evaluated for the UH FEL, using $\hat{K} = 1.2$ and $\lambda_u = 2.3 \ cm$ and assuming a normalized emittance of $4\pi \cdot mm \cdot mrad$, we find that we would need a $y_{max} \approx 110 \ \mu m$ which will have a $y'_{max} \approx 0.03 \ mrad$.

The second (horizontal) requirement is easily met with the parameters of the UH FEL. We assume that the beam is drifting with a Gaussian profile. Using

$$\frac{\epsilon_x}{\gamma} = x_{max} \cdot \theta \quad \text{where} \quad \theta = \frac{x_{max}}{z_R}, \tag{5.9}$$

and z_R is the Rayleigh length and equal to half the undulator length. We can expect a horizontal beam spot of $140 \ \mu m$. Since there is no screen directly at the beginning of the

undulator to achieve these goals we utilize a screen located before the first chicane magnets. This screen is positioned so that a vertical waist and a minimum horizontal beam on this screen would always and automatically input a vertical waist and minimum horizontal beam to the undulator.

5.3   Simulation Results

Scalloping in the Undulator

Scalloping is due to over-focusing of the beam in the undulator. Early simulation results, showed that with the existing beamline configuration, the beam was never entering the undulator at waist and this always resulted in scalloping. Examples of scalloping are shown in Fig. (5.2) and (5.3).
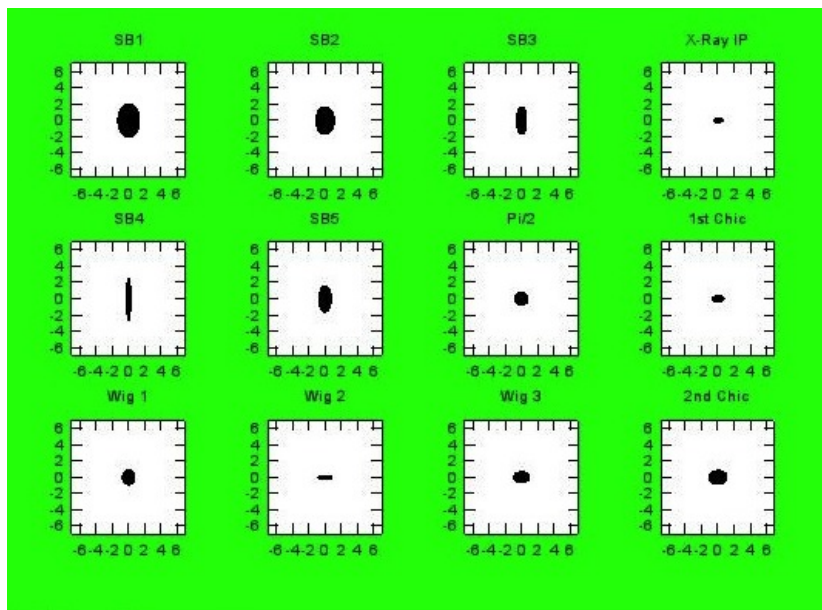
Figure 5.2: Output beam envelope evolution prediction from TSM: beam is entering the undulator (wig1 screen: bottom row first, image) with a profile more focused in the horizontal direction and leaving the undulator (wig2 screen: bottom row, third screen) focused more in the vertical direction.

Symmetric Design

In the original design of the DC, the doublequads after the IP were positioned immediately after the IP, perhaps to collect the diverging beam right out of the microfocus. Both Simu-
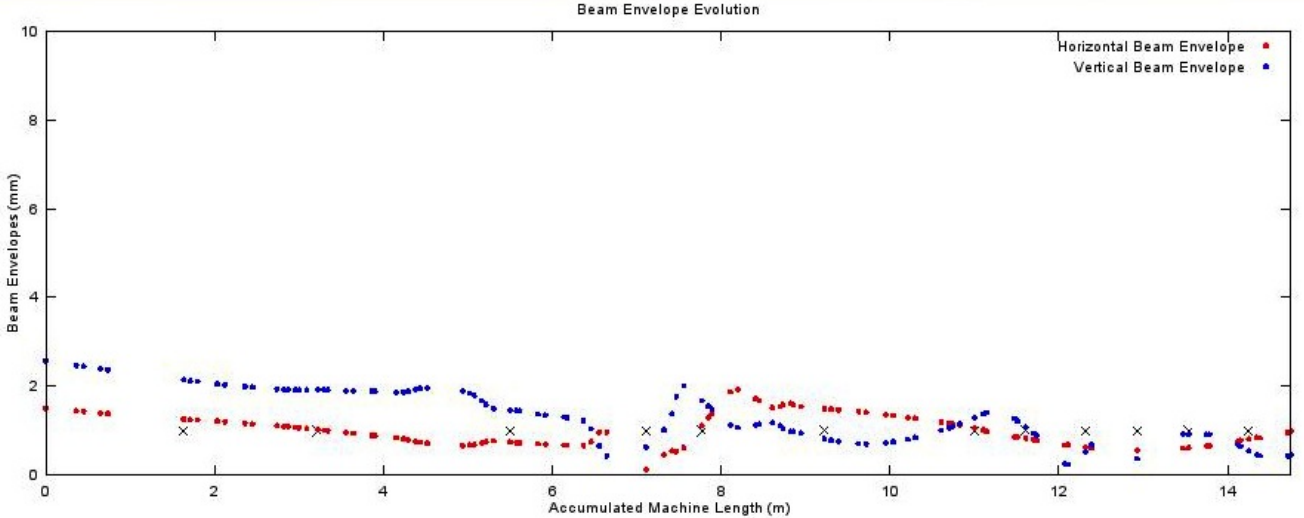
Figure 5.3: Output example of beam envelope evolution predicting scalloping from TSM: the vertical beam profile evolution is not symmetric in the undulator.

lation and hands on examining of this design showed that it would be unsuccessful. A few different symmetric designs were studied with the help of the TSM. We had to consider the positioning of other beamline elements such as BPMs, flanges and etc. The best modification scheme is shown in Fig. (5.4).

Optimum Parameters

As we describe in the previous chapter, it is possible to estimate the beam parameter by means of a match to the undulator and the TSM. A few examples are shown at the end of Ch. 4. A general conclusion from these findings is that the electron gun, more specifically the position of the cathode, plays an important role in obtaining the best match. We found that when the gun's cathode was moved to a position at which the electron beam emerging from the linac was weakly convergent in both the vertical and horizontal planes, achieving the beam requirements became most simple. This result was unexpected.

5.3.1   The Optimum Match

After the beamline modification was performed and a workable cathode position was selected, we were able to demonstrate the predictions of the simulator and the mathematical model. The first 70 μm spot on the IP along with a match to the undulator (identified by the symmetric spots on the chicane screens) is shown in Fig. (5.5). A wirescan of a microfocus
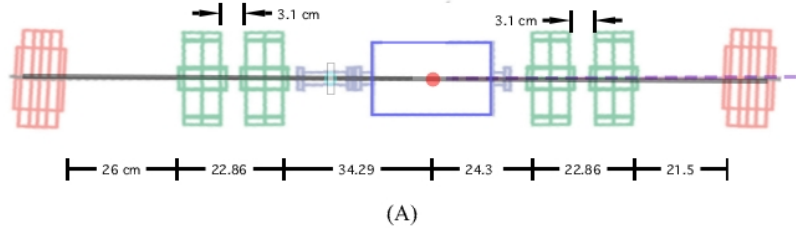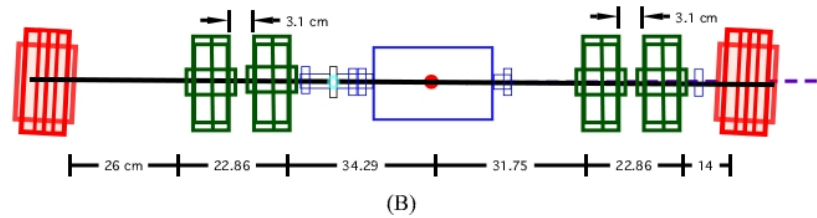
Figure 5.4: Model of the change in the distances of double quads around the IP, (A) before, (B) after.

beam is also demonstrated here in Fig. (5.6). These solutions were able to achieve optimum lasing of $\sim 4mJ$ with the old coupler and $\sim 6mJ$ with the new coupler. An example of strong lasing pulse aligned with the electron beam (ready for an x-ray experiment) is shown in Fig. (5.7)

5.3.2 Preliminary X-rays Measurement

Once a suitable match was found and we were able to align the beam, we recorded some preliminary data for x-rays. In these sets we recorded the scope signal from the detector in two different configuration: 1) when the FEL laser beam was sent to the diagnostic room (not interacting with the electron beam) and 2) when the FEL laser beam was sent to the IP (interacting with the electron beam). We were not able to see a measurable change against the background. Therefore sets of data were collected as the trombone position was changed to provide better statistics (an example is shown in Fig. (5.8)). The trombone is a motorized optical delay line installed for synchronization of the laser micro-pulse phase with the electron bunches. As in Fig. (5.8)), we were able to see a red signal that exceeds the background and its standard deviation for few different trombone positions, however the

43
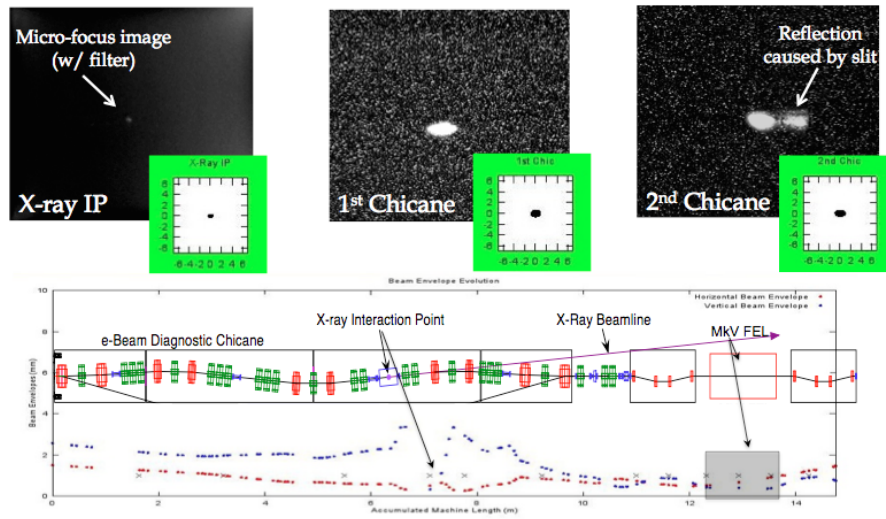
Figure 5.5: Comparison of the TSM prediction and beam profiles for an optimum match for the ICS experiment.
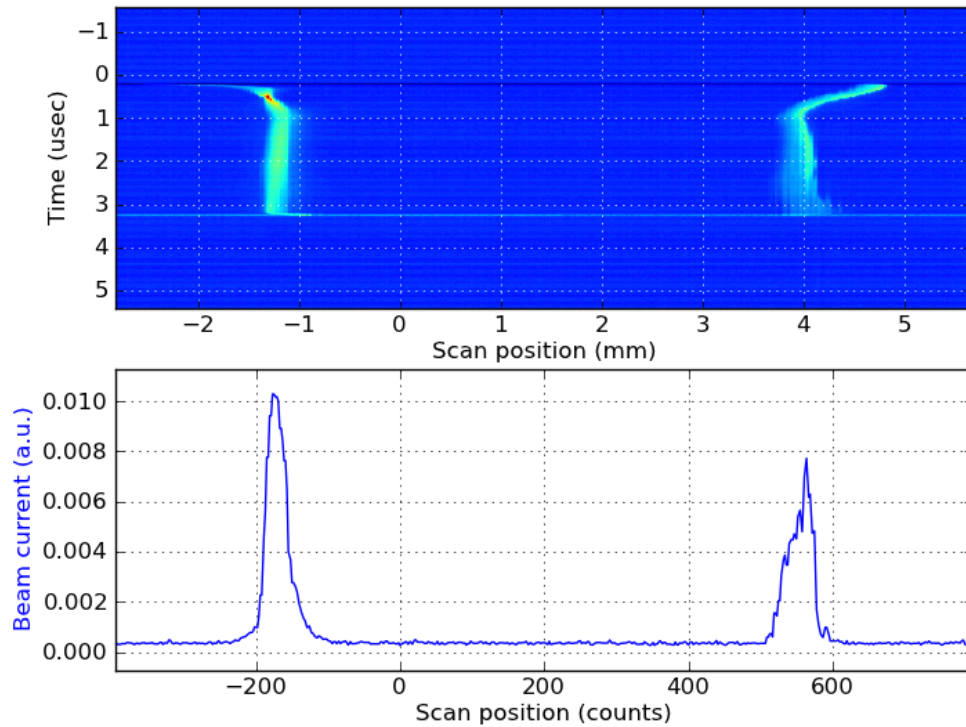
Figure 5.6: Wirescan of the microfocus (electron beam only).
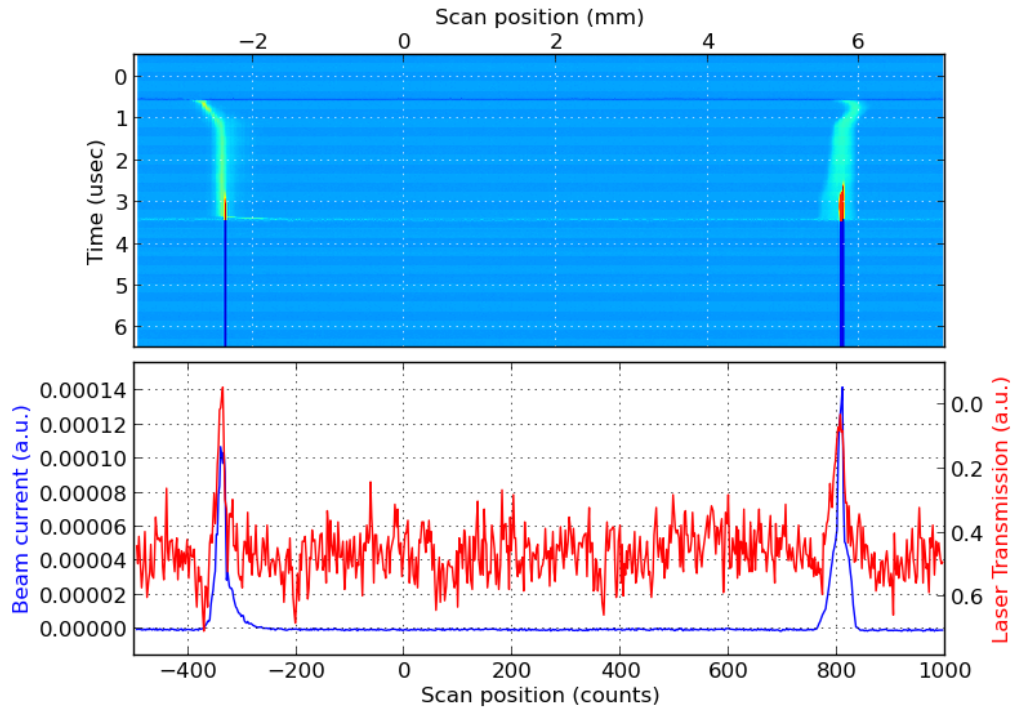
Figure 5.7: Wire scan of the microfocus (electron beam and laser beam aligned) ready for x-ray measurement. The fully optimized laser for this run had a pulselength of $\sim 1.4~\mu$s and energy of ~ 2 mJ (Dec 17th, 2015), however laser power was reduced, by detuning the cavity, by a factor of 4 to prevent damaging the wire.
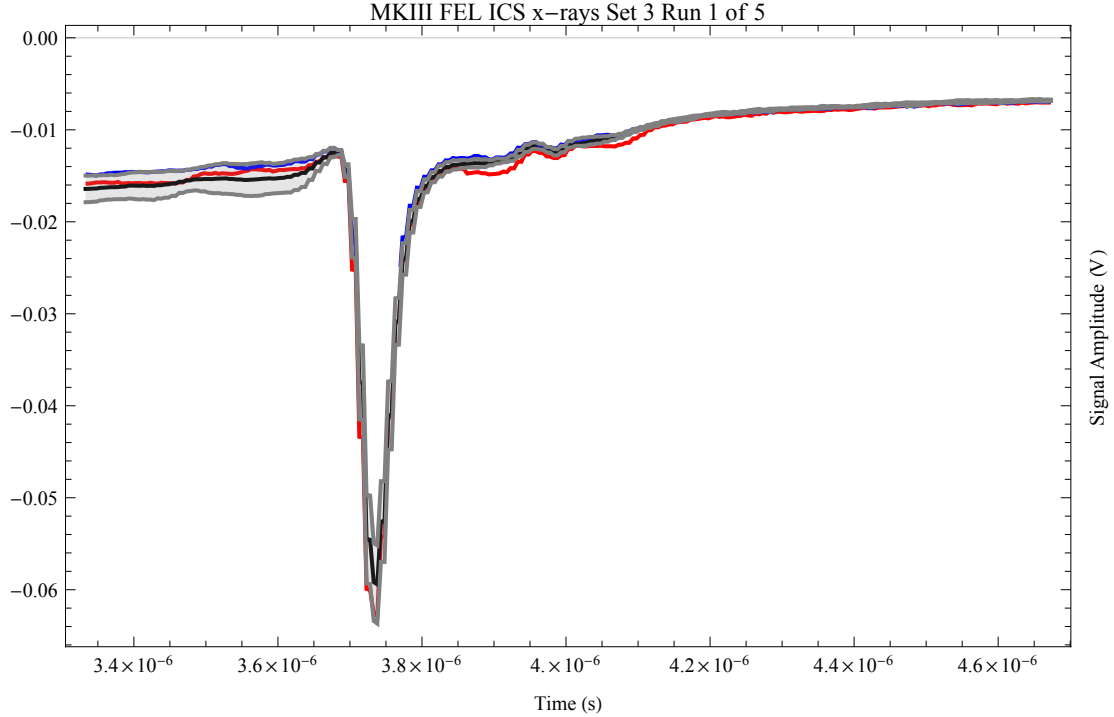
Figure 5.8: Averaged signal (red) in comparison with averaged background (black) with standard deviation (gray region) from 20 scope dumps.

signal was not reproducible for the same trombone position in these runs. A more detail study of the x-ray beamline and expected signal, was needed which is presented in the next section.

5.4   X-ray Measurements and Methods of Analysis

Description of the Beamline from IP to the Detector:

The x-ray transport pipe from the IP to the hutch PMT detector (a 6911 Hamamatsu photomultiplier) includes the following:

1) 0.5 m transport in air

2) 8.5 m transport pipe purged with Helium (will assume that the helium line has 80% helium and 20% air)

3) A collimator

4) A thin (.010") Yttrium Aluminum Phosphate (YAP) screen

We ignore all reflection from the IP to the YAP screen since for 10 keV electrons, the index of refraction of all the material in the beamline is ~ 1. In addition to the above elements, we must factor in some geometric loss since the detector only subtends part of the solid angle that the emitted x-rays. On the other hand, the response of the PMT is measured by a scope, so the photocathode response must be calculated based on the data-sheet information from the PMT. We also include the attenuation and reflectivity of the soda line glass covering the cathode of the PMT. Depending on the number of signal photons to be counted, we use one of two ways available to quantitatively measure their count rates.

Estimating X-ray Signal

X-ray transmission through the 0.5 meter air section is estimated to be 0.73 based on attenuation factors provided by [33]. For the Helium purged line, we have a transmission of 0.34 [33]. The geometric loss and the collimator loss are calculated to be approximately 0.03 and 0.52. After passing through the first three element of the x-ray transport line, the 10 keV inverse Compton x-rays generated by the counter-propagating electron and laser beams are detected using a YAP crystal scintillator that is fixed on the glass envelope of the cathode in the PMT. This arrangement provides both a large fluorescence signature for the incident 10 keV x-rays (a blue photon per x-ray photon) and also a significant bias against the other incident photons or particles that are generated by the background counts in the systems The thin film of the YAP has its maximum sensitivity to incident photons at the energy of the x-rays to be detected, 10 keV. X-rays of higher and lower energy produce fewer fluorescence photons, therefore the background noise counts attributable to those photons are rejected based on their reduced current amplitude.

5.4.1   Photon Counting

Another important factor is that the time structure of the fluorescence photons generated by x-ray photons in the YAP is unique, characterized by an exponential decay of 25 nanoseconds to be compared with the 3.5 nanosecond pulse duration of output current pulses initiated by field emitted electrons within the PMT or with the much longer fluorescence decay of the photons emitted by the glass envelope of the tube as a consequence of neutron irradiation at the beginning and end of each beam pulse. The electrical pulses attributable to these noise sources could therefore be rejected on the basis of their differing pulse shapes (realized in our setup by the rejection of all those PMT output pulses having non-exponential

decays, or exponential decays with lifetimes other than 25 nanoseconds [24]).

At very low rates, the digitally recorded output pulses from the PMT were first analyzed to eliminate all pulses not having the required 25 nanosecond exponentially decaying pulse shapes, and then were binned by pulse height to identify those incident photons that had both the required pulse shape and height. The appearance of a flux of 10 keV inverse-Compton x-ray photons was then determined by the change in count rate when the laser beam was blocked. An example of photon counting data is shown in Figs. (5.9) and (5.10). The 11 per second photon data is at 7 mm trombone position.
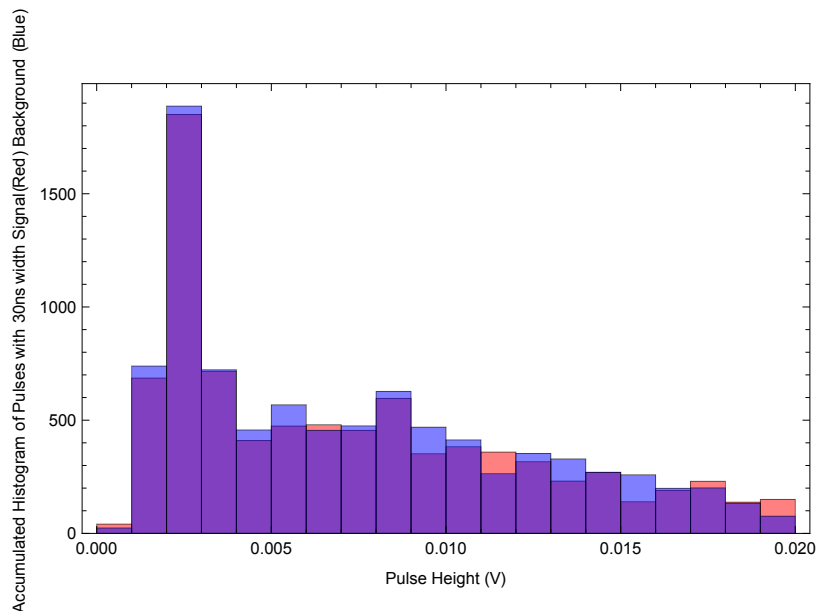
Figure 5.9: Example of photon counting when there is no sign of 10 keV photons.

5.4.2   Averaging Flux from PMT Output

For high flux rates, even with the noise rejection capabilities mentioned above, the number and size of the background radiation pulses could still cause a problem as the signals would overlap and it would be hard to recognize their pulse size. Therefore, at higher count rates, the current from the PMT was gated to isolate the interval in time during which the laser power responsible for the emission x-rays is present, then integrated to obtain the average PMT output current. This includes both the signal and noise counts, so when the beam stop is in, the output current is at its min. The variation of this current, with the timing of the colliding electron and laser pulses, enables the identification the time-averaged component of
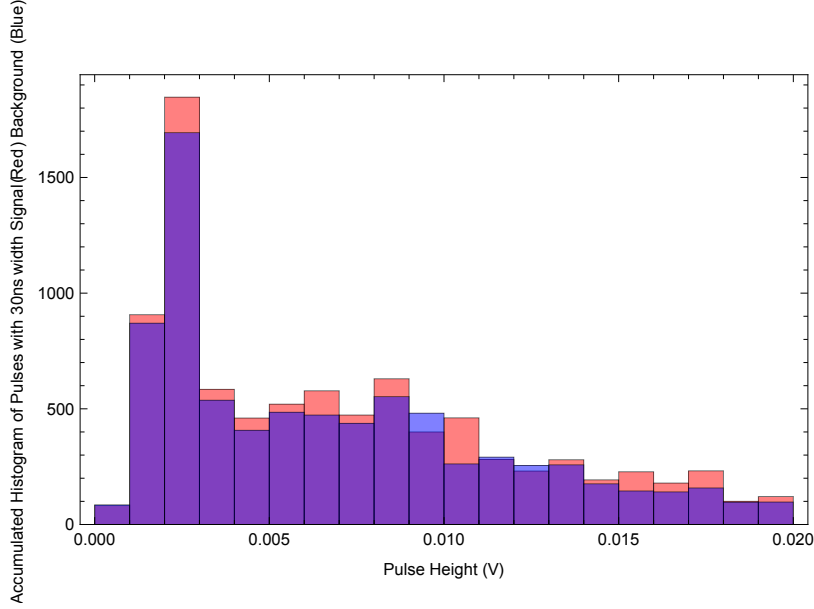
Figure 5.10: Example of photon counting when ~ 11, 10 keV photons per second were recorded.

the PMT current attributable to the signal counts. The count rate is determined by the ratio of the average detected signal current to the estimated charge per detected x-ray photon.

Estimating the Total Flux Based on the PMT High Voltage

We estimate the total flux based on the PMT high voltage using the data available for the YAP screen [34], the PMT glass [35], and the PMT responsiveness and current amplification, in addition to the factors introduced earlier for air and helium attenuation as well as the loss factors). Fig. (5.11), prepared by Jeremy Kowalczyk, is an excellent plot that is convenient for estimating the average flux based on the recorded scope value and includes all the factors listed in this section, except for the saturation effect of the PMT) [36].

An example of data recorded using a box car integrator based on the average flux (the boxcar integrator gate width was set to the last μs of the pulse) and PMT response picked up by the scope is presented in Fig. (5.12). We can see that the background counts are the order of 1/10th or 1/20th of the average signal and that the integrator response suggests a high flux at a trombone position of 14.1 with a laser beam of 2.6 mJ. The scale was adjusted so that the averaged signal due to electron beam only was 40 mV. We detected a signal of approximately 30 mV at trombone position 14.1 mm. This position does not agree with the position of maximum low flux recorded data and was not reproducible. We concluded that
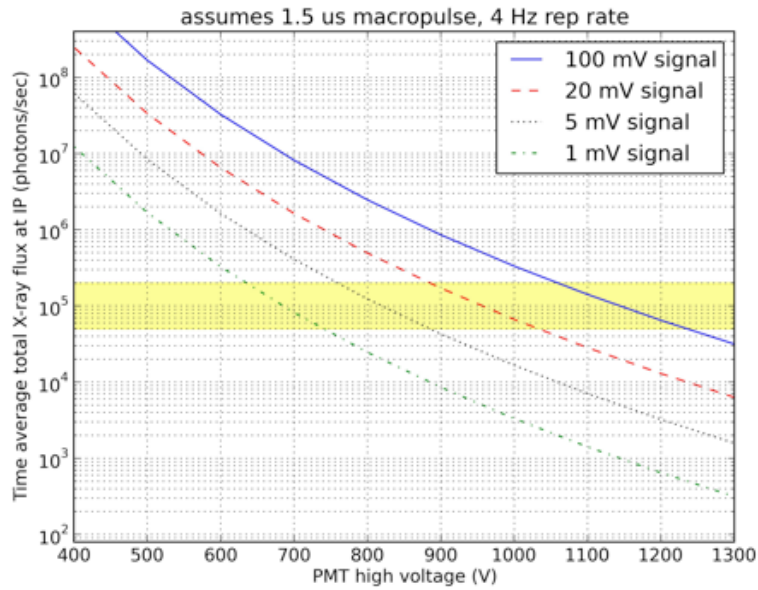
Figure 5.11: Plot showing the response of the PMT for different average photon flux. [Courtesy of J. Kowalczyk]
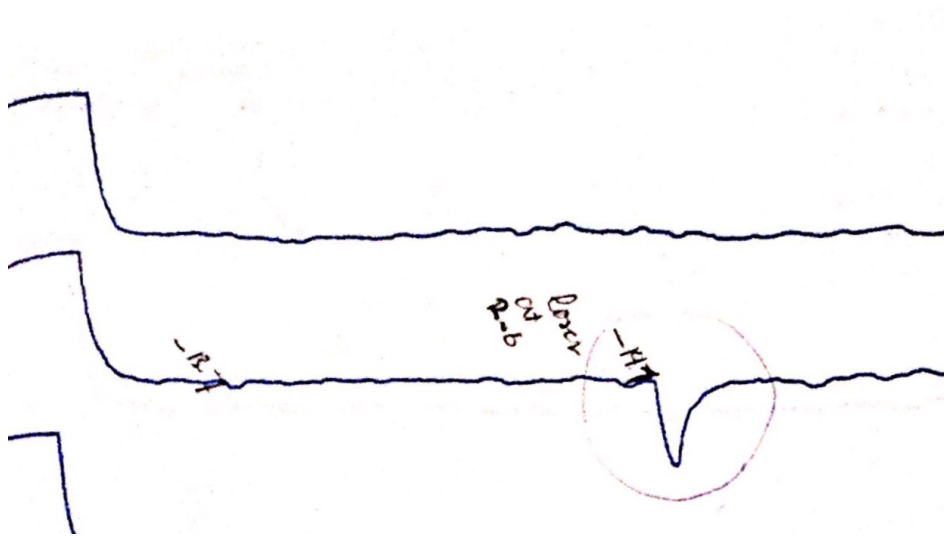
Figure 5.12: Output of the boxcar integrator using a Hewlett Packard x-y plotter (HP 7035 X-Y RECORDER) starts with (on the left) the highest output value (for the minimum current when the beamstop is in), then the beam stop is removed and the averaged beam signal as we changed the trombone position is recorded. At 14.1 mm a signal corresponding to expected flux from the PMT is recorded Date: Nov 26th, 2015.

there are stability and synchronization problems to be solved. These issues will be discussed in the next chapter.

CHAPTER 6
DISCUSSION, REVIEW AND TREATMENTS

6.1 Investigating the Problem of Low Statistic

In the last section of previous chapter, we discussed the preliminary x-ray measurements. Here we present a review and discussion of factors we found to be limiting to the performance of x-ray experiment. In each case, a solution is presented which is either already implemented or will be implemented in the near future. There are five factors that are of significant importance. Three of these factors are related to the beamline transport section and two are related to the accelerating section:

- Background Radiation
- Alignment of X-ray Beamline
- Synchronization Electron and Laser Optical Pulses
- Instability Due to Cathode
- Waveguide Multipactoring

6.1.1 Background Radiation

We discovered that even when the electron beam was stopped by the beam stop before entering the linac, a large background signal was detected. A careful investigation revealed that this signal was most likely due to the production of neutrons in the lead shielding material near the IP. These neutrons also produced florescence in the YAP glass installed before the PMT which also contributed to the background signal. Three different measures were taken to reduce the amplitudes of the large initial and trailing edge of these pulses: 1) replacing the lead shielding blocks with aluminum blocks consisting of the same number of radiation lengths, 2) installing a series of 1 inch thick polyethylene boards around the beam pipes to reduce the energy of the remaining neutrons before they could induce fluorescence in the glass, and 3) installing borated polyethylene (5% Borated - Green Color) squares with a only a small aperture for x-rays between the steel frame and coils of the two quadrupoles before the end of the x-ray pipes to provide a perfect path for the 10 keV x-rays (Fig. (6.1)). By these measures, we were able to significantly reduce and almost eliminate the described background radiation signal.
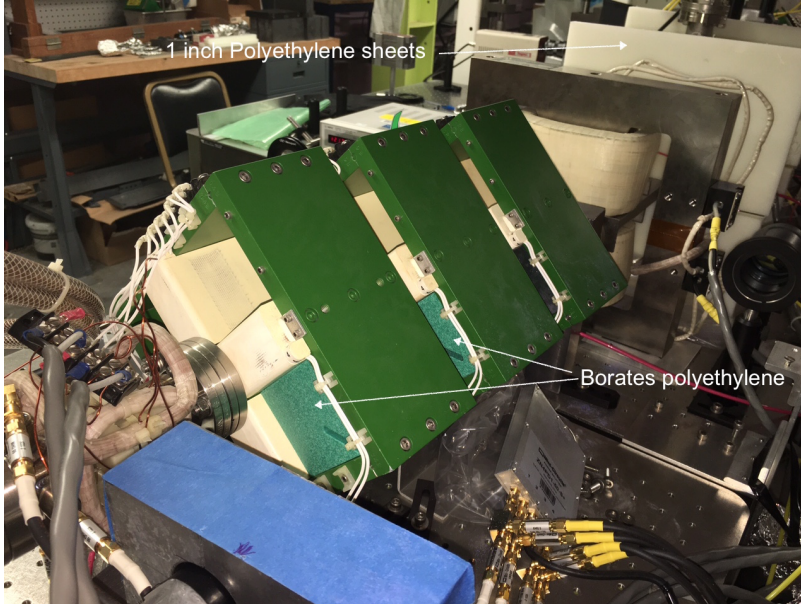
Figure 6.1: Shielding placed around the x-ray paths, polyethylene boards and borated polyethylene blocks shown.

6.1.2 Reinvestigating Alignment of X-ray Beamline

Since the backscattered x-rays in inverse Compton scattering are emitted in a $1/\gamma$ cone centered on the axis of the incident electron beam, it is essential to ensure that the path for x-rays from the IP to the detector in the hutch is clear and aligned. Even though the layout of the diagnostic chicane, the positions of the quad doublets for the x-ray experiment, and the x-ray beamline were designed carefully, we thought it could be possible that there is a misalignment in the position of the long 2 inch diameter hole for the x-ray beam through the shielding wall. Therefore, alignment of all of the elements of this system was carefully investigated. W first examined the line of sight clearance, next checked the alignment of each element and used a string to extrapolate the axis of the quads to make sure the path for x-rays was clear. Finally we used pieces of x-ray medical film cut to conform to the inner boundaries of the pipe and the hutch. We recorded the positions of the x-rays generated during the electrons' passage through the insertable SiC TR screen (IP screen) on these x-rays films.

The bremsstrahlung radiation emitted by the electrons passing through the thin SiC screen, like the backscattered inverse-Compton x-rays, are also emitted into a $1/\gamma$ cone centered on the electrons' axis, therefore they were a reliable measure for verifying the alignment. The bremsstrahlung x-rays were more intense than the inverse-Compton x-rays

and exposed spots on the pieces of x-ray film that were easily discernible by eye. Two example of these spots with their relation to the inner boundaries of the components of the x-ray beamline is shown in Fig (6.2).

<div align="center">(a)   (b)</div>
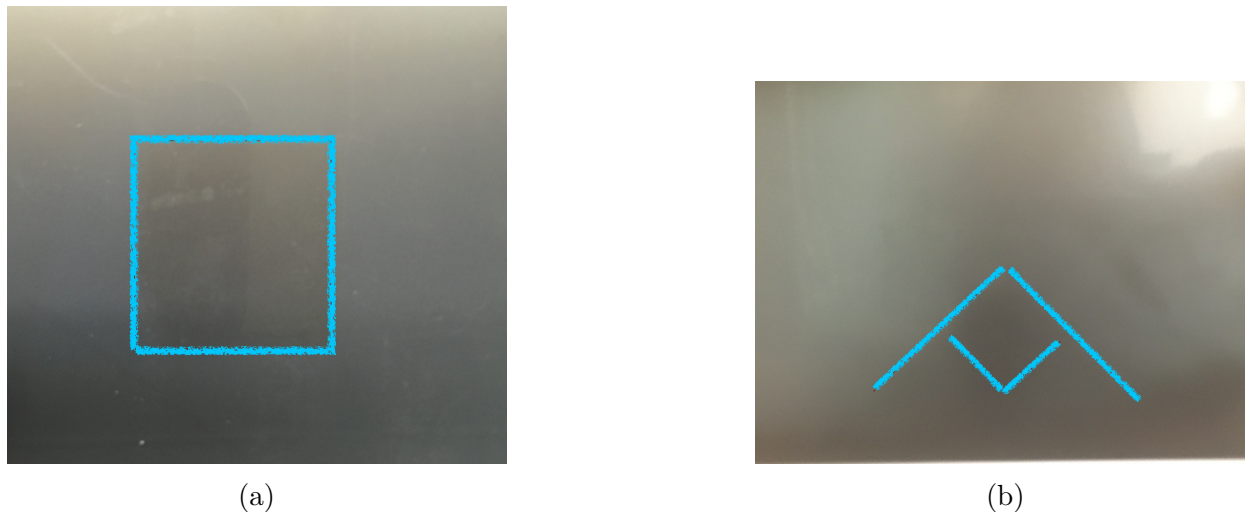
Figure 6.2: Spots recorded on the x-ray films due to bremsstrahlung x-rays (a) at the hutch (the collimator is highlighted), (b) by the pipe (the lead shielding and dipole walls are highlighted).

The conclusion was that the 1 x 1 inch square hole in the thick steel collimator in front of the PMT's photocathode was centered and the collimator and the cathode of the PMT were centered on the axis of the backscattered ICS x-ray beam.

6.1.3 Reinvestigation Synchronization of Electron and Laser Optical Pulses

The optical transport from FEL to IP was designed to be a robust and stable transport system that delivers the laser to the IP optical bench with minimum loss of the IR laser. This system is responsible for both steering and aligning the IR beam and electron beam at the IP and insertion of a precision optical trombone delay which adjusts the synchronization of the IR and the beam pulse. As we discussed in the last chapter, so far, the detected x-rays during different runs were at different trombone positions. As this system has passed rigorous tests [30], we conclude that instabilities of the the electron beam are the main cause. To alleviate this issue, we have considered operating with a larger beam (~ 1 mm minifocus). This however will reduce the x-ray flux and care must be taken in reducing the background radiation so that a signal is detectable. The estimated signal for an electron beam of 1 mm

size at IP and a 2.5mJ laser on the PMT is ~ 20 mV. For a 2 mm electron beam the signal on the PMT will reduce to 5 mV [37], which is close to the background level. Beam-beam synchronization, however, would become simpler and once the beams are colliding we can work our way to the microfocus match. The advantage of this treatment is that we would have a live feedback when we are adjusting the focusing and alignment from the x-ray signal the very same way that we have live feedback from the laser when optimizing the match. Additional discussion for this treatment is presented in the later sections of this chapter.

6.1.4 Cathode

We realized that cathode contamination and/or operating temperature could become a limiting factor during the x-ray runs. The LaB_6 cathode surface is subject to contamination at lower than 1750 K temperatures[38]. This can reduce the work function of the cathode and increase the emitted current, which would cause further reduction of the operating temperature. In this case, unfortunately, the resultant beam is not reproducible or uniform across the face of the cathode leading to variations in the emittance, temporal and spatial profiles of the accelerated bunches from run to run. Considering the sequence of measurement and setup required to start an x-ray run, this is a serious problem. To suppress this effect, a few different designs for the heater coil of these cathodes were tested and one that enabled stable operation at temperatures of 1750 K and above was selected. Making these coils is also a challenge, but cathode system would last for almost a year when with a well designed coil. With these coils, the cathode is operated at temperatures above 1750 K and "baked out" after and/or during long operations. This allows for sufficient time to be available to acquire the data of interest. When operated in the "laser cooled mode" the cathode temperature typically exceeds 1750 K following the laser pre-pulse at the start of every macropulse, insuring stability on an ongoing basis without the need for periodic re-conditioning [36]. We hope that after the commissioning of the laser-cooling set up we will have a much more stable beam and reliable set up for the ICS x-ray experiment.

6.1.5 Waveguide Multipactoring

One of the main challenges during the ICS x-ray experiment was managing multipactoring of the accelerator system. Multipactoring causes large, random shifts in the phase of the electrons ejected from the gun relative to the carefully controlled accelerating fields in the linac. Based on the papers published from other laboratories, multipactoring is difficult to suppress

and does not always respond to conditioning. In our system, this instability sometimes become very hard to control. We were finally able to suppress the multipactoring instability by wrapping many hundreds feet of # 12 wire in the form of a long solenoid (thanks to patience of Ian Howe) around the section of waveguide in which we determined the multipactoring took place. The wire creates a magnetic field within the waveguide which alters the trajectories of the fields emitted by the electrons inside the guide so that the probability of collisions with the interior surfaces of the guide is reduced compared to the operating frequency. This however, was often a deferred response and would reduce multipactoring after a day or two. We also discussed the possibility of introducing a stochastic phase field that would interfere with the build up of the collisions in the guide and, somewhat serendipitously, we discovered that by turning the feedforward system off (discussed in Ch. 3) during the conditioning, often we are able to get rid of multipactoring most efficiently.

6.2 Further Studies for Improving Beam and Setup

6.2.1 Study of Cathode Position to Improve on the Match Solution

As we said earlier, we have found that a detail study of cathode, beam parameters and lasing gives us valuable insight for setting up the x-ray experiment. Every time a new cathode is installed, a careful study of the parameters and flexibility of each position is performed. A sample study is presented in Table 6.1. The third column indicates if that particular cathode position is suitable for a microfocus setup or not. The last column shows the total roundtrip cavity loss which will be discussed in 6.2.3.

6.2.2 Study of Phase and Minifocus Match

In order to remedy the synchronization problem, we proposed a minifocus set up (1 mm electron beam at the IP). When we first set up for the minifocus, we saw a very high background radiation level. After examining every aspect of the set up we realized that this high radiation level was due to scraping of the beam on the mirrors of the scattering chamber. A careful study, similar to that of Ch. 5, was done by means of the simulation module. We learned that gradual focusing and defocusing before and after the IP solved the problem. We also learned that adjusting the phase by only few degrees would reduce the halo of the beam which in return would improve the minifocus, match to the undulator,

Table 6.1: Study of the Cathode Position Influence.

Cathode Position	Lasing (mJ)	microfocus match	Fall Time Constant	Round Trip Loss (%)
g	2.2	N/A	-10.16	12.19
f/g	1.7	N/A	-9.78	11.74
g/h	3.5	No	-9.98	11.98
g/h	1.0	Yes	-9.40	11.28
g	1.6	N/A	-7.61	9.13
f/g	1.0-1.7	N/A	-9.87	11.84
f/g	1.5-1.8	Yes*	-9.67	11.60
f	1.9	Yes	-3.41	4.09

* X-ray run

and reduce the background radiation. Fig. (6.3) shows study of halo and phase for a setup run (a run dedicated to tuning all the parameters before a full x-ray run.) Also, Fig. (6.3) shows the beam images on the TR screen from split bend 4. We plan to change this screen to a synchrotron radiation (SR) monitor/screen once the we are running at beam energy of higher than 40 MeV. This would allow monitoring of the beam spot size and stability of the system without disturbing the beam.

6.2.3 Study of Loss in the Undulator Cavity Due to Coupler and Mirrors

Another issue that was raised during the minifocus setups was the reduced laser power during a few set up runs. We suspected that the mirrors of the optical cavity for the FEL were damaged however that review of the round trip loss in the undulator based on the fall time of the laser showed that for all the runs the loss was approximately equal to that of the coupler. This study lead us to change the coupler of the optical cavity from a 12% to a 4%. After this change we were able to achieve twice as much laser power and the laser spot sizes were more than adequate for the ICS experiment. Fig. (6.4 shows the electron beam only and and 6.5) shows the electron beam and laser beam aligned for the ICS experiment (minifocus) after set up with the new coupler. The estimated signal for an electron beam of 1 mm size at IP and a 6 mJ laser on the PMT is $\sim$ 40 mV[37]. Since we have already eliminated the background issue, we should have a suitable setup for our next x-ray run. We expect to take this data in late spring or summer of 2016.
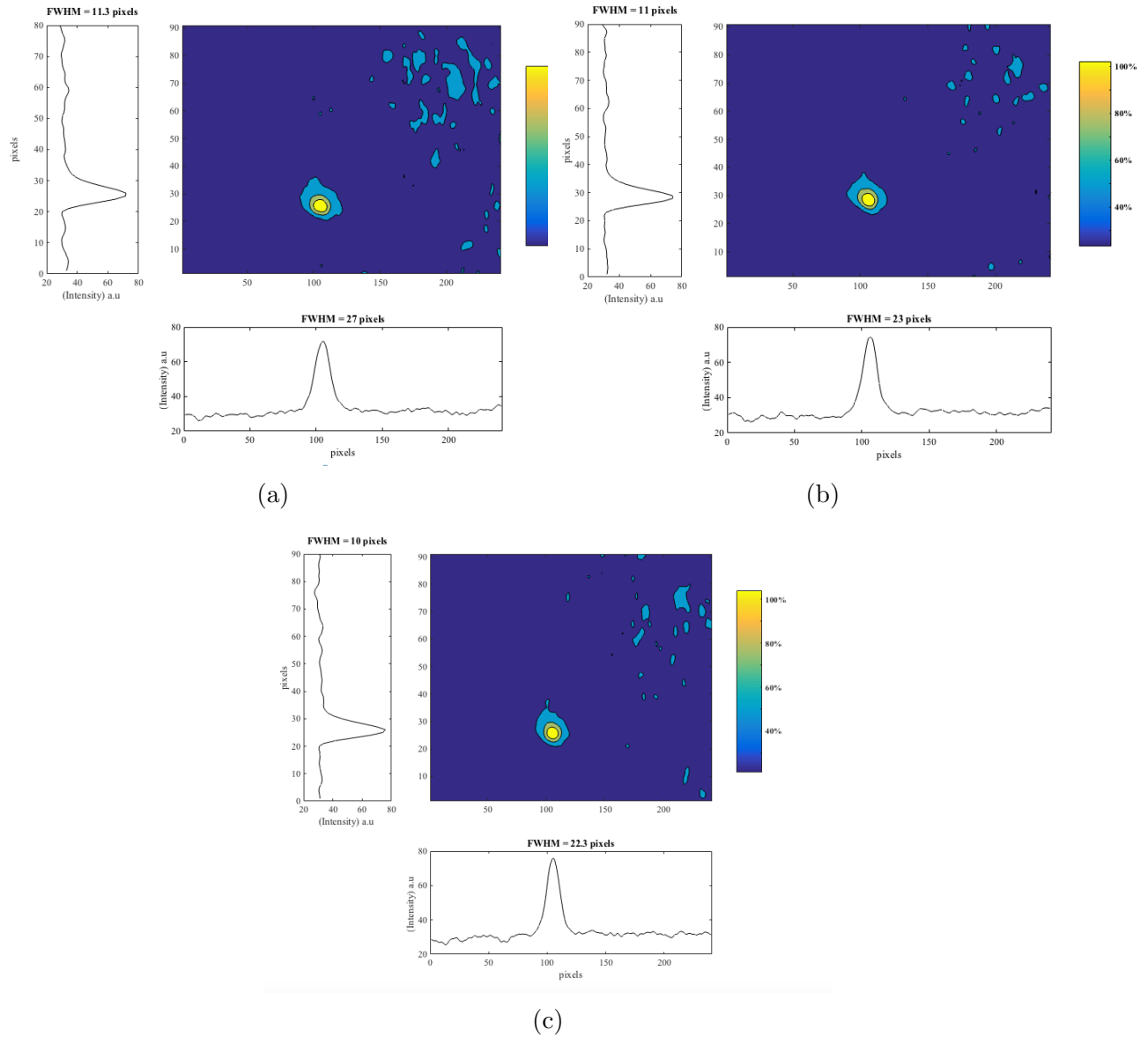
Figure 6.3: Adjusting the phase will reduce the halo of the beam. At (a) phase = 221 Ω, at (b) phase = 223 Ω, at (c) phase = 222 Ω, and (c) shows the beam with minimum halo. Here the phase recorded in Ω is the resistance of the linear encoder which reads the position of the movable shunt in the phase shifter.

58
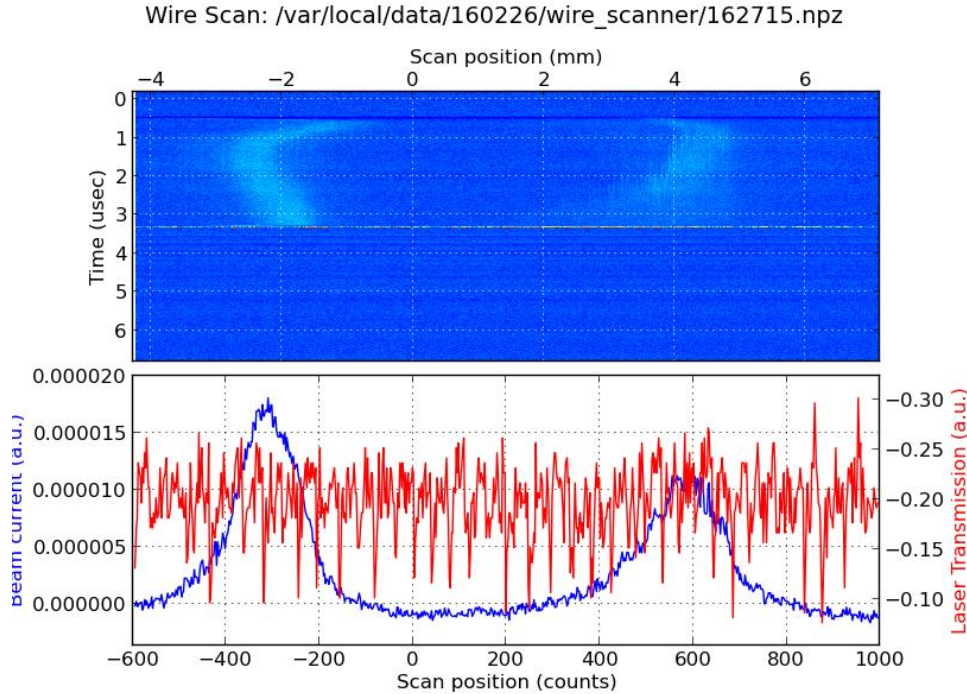
Figure 6.4: Wirescanner measurement for the minifocus setup (electron beam only).

6.3 Final Strategy for Future X-ray Runs

As we showed in the previous sections, although the minifocus allows for better alignment and synchronization of the electron and the laser beam, it introduces additional requirements to the set up. Here we present the sequence of steps that must be taken in order to have a successful x-ray setup. It must be noted that even with the addition laser-cooling for the cathode it would be a good idea to follow the steps below. Once system stability has been improved, some of the checks listed here would not be necessary and it would be possible to partially or fully automate this process. For full automation, a few more diagnostic and control tools (at the very least two SR screens) would be needed.

A successful x-ray set-up requires:

1) Start from a cathode position that supports a microfocus set up,

2) Eliminate steering of the beam in the quadrupoles up to split bend 4,

3) Focus the beam on split bend 4,

4) Find the best phase for the set up (minimum beam halo),

5) Set up for minifocus at that phase,

6) Test if inserting the mirrors increases the background,
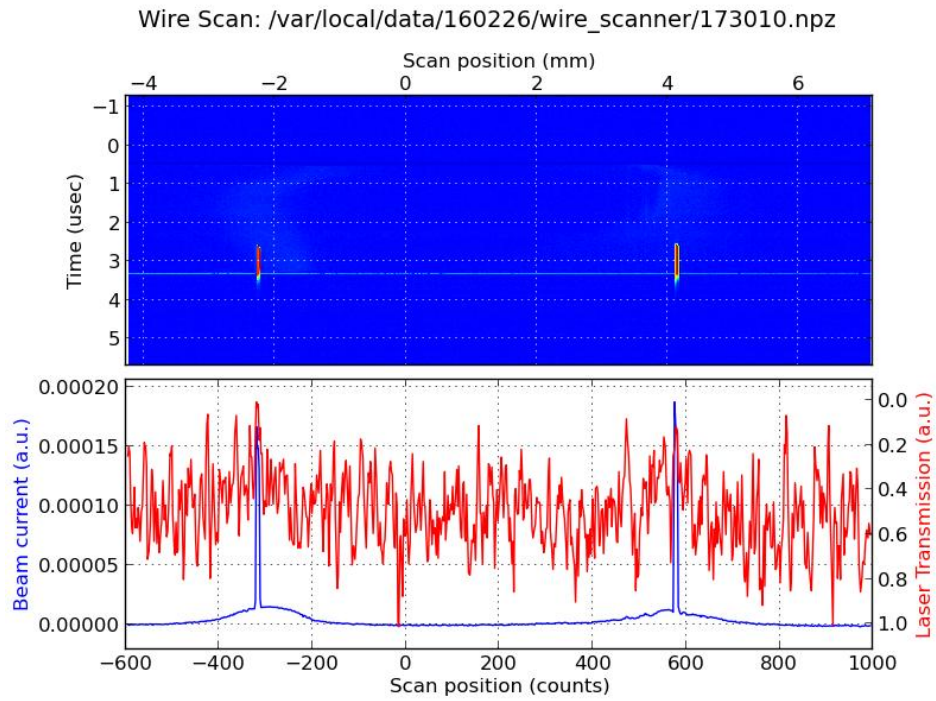
Figure 6.5: Wirescanner measurement for the minifocus setup (aligned laser and electron pulse). The fully optimized laser for this run had a pulselength of $\sim 1.5\ \mu$s and energy of ~ 3.6 mJ (Feb 26th, 2016), however laser power was reduced, by detuning the cavity, by a factor of 6 to prevent damaging the wire.

7) If yes, reduce the background while the mirrors are in,

8) Check lasing,

9) Optimize lasing while the mirrors are in and the background is being monitored ensuring that the background remains low,

10) Align the electron beam and the IR beam,

11) Check if the electron beam is still centered,

12) Check if the electron beam and the laser are still aligned,

13) Repeat steps 9 through 11 until everything is aligned ,

14) Check for x-rays,

15) Find the trombone position for which the electron and the IR beam are colliding,

16) Improve on the minifocus (until approaching a microfocus) and alignment while monitoring the x-ray signal and/or background,

17) maximize the x-ray signal.

6.4   Short Review on the X-ray Detector Development at UH

As we said earlier, the TEDA experiment was a joint project between the FEL and IDL lab at UH. One lab was to provide the x-ray source and the other was to provide the detector and the means by which the x-rays were to be measured. Here we present a short review of the major goals and accomplishments of the detector side of TEDA as well as the general direction the IDL is taking as far as it relates to XFEL detectors. The general goal for the TEDA project was to develop a time resolved picosecond detector and data acquisition system. For this purpose components of an integrated system were designed and fabricated from simulation to mask and board design. The general picture is as follows: the x-rays are stopped in the detectors, the signal from the detectors then is amplified and transferred and backed on servers by means of giga-bit fiber optic links. An important milestone that is significant for the future generations of XFEL detectors was verification of the half decade old prediction that the Switch Capacitor Array technique is capable of picosecond resolution [39]. The design of the Application Specific Integrated Circuit (ASIC) which not only has picosecond resolution but is also a high intensity detector integratable, Giga-sample per second with GHz analog bandwidth [40] (PSEC4) was studied in detail as a joint class project during my studies and proved promising for the next generation of XFEL detectors.

Part II

Study of Radiation Reaction Force and Its Application for Antennas and Self Amplified Spontaneous Emission X-ray Free Electron Lasers

CHAPTER 7
REVIEW OF FUNDAMENTALS OF RADIATION

7.1   Objective

For the foreseeable future, the analysis and design of the complex systems needed to generate intense beams of radiation via the process of coherent emission into free-space will depend on the principles and methods of classical electrodynamics (CED). But the fields and forces predicted by the currently accepted CED theory are manifestly incompatible with Maxwell's equations' energy integral as applied to the process of coherent emission into free-space. It is the purpose of this document to review the evidence for these limitations of conventional CED, to identify an alternative formulation of CED that does not suffer from these defects, and to describe how the predictions of this more physically realistic formulation of electrodynamics, including the role of the advanced interactions allowed by Maxwell's equations and thermodynamics, might be tested by experiment and applied to enhance the capabilities of devices and systems employing the mechanism of "radiation into free-space."

7.2   Radiation in Free Space

As the technology of electron beam-based sources of electromagnetic radiation has advanced, the significance of the physics of the process of coherent radiation, in which a number of charges within a fraction of a wavelength are induced by their synchronized motion to emit electromagnetic radiation, has increased. In such coherently radiating systems, the amplitude of the emitted electric and magnetic fields increases linearly with the number of radiating charges, leading to radiated powers that increase as the square of that number, in contrast to powers that increase linearly with total charge applicable to the emission of radiation by charges moving in uncorrelated random motion.

Historically, the first applications of this coherent radiation process involved the radiation emitted by such coherently moving charges within the reflecting boundary conditions of radio-frequency, microwave, or optical cavities [41]. The presence of these reflecting boundaries made it necessary to implement forms of analysis that explicitly included the effects of these boundaries on the fields within the cavities and hence on the dynamics of the moving

charges, typically via the reformulation of the systems' equations of motion in terms of the amplitudes of the cavities' normal modes as developed by Slater [42, 43]. By these means, it is now understood that the dynamics of these systems reflect at every time and spatial scale the interactions between the moving charges within each of these cavities and the currents induced by these charges in the walls of the cavities as determined by the relevant boundary conditions.

More recently, technology has advanced to the point at which sources based on the radiation emitted into free-space by intense, coherently oscillating relativistic electron beams in free electron laser systems without the resonator mirrors employed in the earlier cavity-based FEL oscillators have been used to generate unprecedented levels of power at ultraviolet and x-ray wavelengths [44, 45, 46, 47, 48, 49]. But the presently available field-based classical electrodynamics (CED) theory available to analyze the dynamics of these intense coherently radiating charge distributions can be shown to be deficient, yielding fields and forces that are incompatible with Maxwell's equations [50] and relying on the imposition of boundary conditions that are manifestly incompatible with the actual physical boundary conditions for these systems. The existence of these problems was first described by Kimel and Elias, who also described a phenomenological but fully covariant modification to the electrons equations of motion to insure the conservation of energy in such radiating systems [51, 52].

As related in further detail below, the failings of conventional, field-based CED are most easily demonstrated through consideration of the fields and forces predicted by conventional CED for an elementary system consisting of a pair of coherently oscillating charges separated by a distance on the order of a wavelength at the frequency of oscillation, including wavelengths and spacings extending out to the physically macroscopic wavelengths relevant to radiation at microwave and radio frequencies. The persistence of the failings of conventional field-based CED [53] at these meter-scale distances makes it clear that the problem is not the consequence of the limitations of the models used to analyze the self-forces needed to conserve energy in the case of single oscillating particles or their equivalent continuous "fuzz ball" [54, 55, 56, 57] charge distributions, but rather must be found in the nonlocal forces attributable to the coherently oscillating charges subject to the relevant boundary conditions for "radiation into free, unbounded space."

It is the first purpose of this document to establish the limitations of conventional field-based CED by demonstrating that the approach is manifestly incompatible with the requirements implicit in the energy integral of Maxwell's equations in the simplest possible case of the coherent radiation emitted by pairs of synchronously oscillating charges spaced by

distances of the order of a wavelength.

We will also observe in this section that one of the potentially relevant limitations of conventional field-based CED theory is its reliance on the imposition at all spatial and temporal scales of Sommerfeld's "radiation condition" restricting the Green's function for radiation by isolated accelerated elementary charges to the "retarded" solutions allowed, but not mandated, by Maxwell's equations (page 245 of [58]). The restriction to the retarded solutions of the wave equation in the case of radiation into free-space stands in direct contrast to the successful solutions of the radiation problem in closed, conducting or reflecting cavities in which there can be no distinction on physical grounds between the advanced and retarded solutions to the wave equation in the absence of the irreversible thermodynamic processes (like dissipation) postulated by Einstein [59] as a prerequisite for the determination of the direction of the "arrow of time" (page 394 - 395 of [60]).

Whether it is simply the reliance on Sommerfeld's radiation condition that is responsible for the manifest failings of conventional field-based CED has yet to be established. But what has recently been established is that a competing model of CED, the action-at-a-distance model of Wheeler and Feynman [61], (1) allows for the time symmetric inclusion of both the advanced and retarded interactions allowed by Maxwell's equations, (2) includes a plausible if not unique statement of the physical boundary conditions for the case of radiation into free-space, and (3) provides a description of the forces generated through the process of coherent emission that is fully compatible with the energy integral of Maxwell's equations in contrast to the fundamentally flawed solutions of conventional field-based CED as restricted by Sommerfeld's radiation condition.

It is the second key purpose of this document to demonstrate that the solutions developed by Wheeler and Feynman in their model of "radiation into free-space" successfully predict the forces needed to insure compliance with Maxwell's equations. The success of this model does not necessarily imply the need to abandon the field-based electrodynamics, but demonstrates the need to reformulate it. In a mathematical sense it demonstrates the need to include both Lienard and Wiechert's "special" solutions to the inhomogeneous wave equation [62, 63] and the homogeneous solutions needed to satisfy boundary conditions.

The intriguing implications of the revisions to conventional field-based CED theory (needed to insure compliance with Maxwell's equations) suggest an experimental test be undertaken of the effects predicted by inclusion of both the advanced and retarded fields allowed by Maxwell's equations and Wheeler and Feynman's assumed "absorbing" boundary conditions. It is the third purpose of this thesis to describe such possible experiments.

Finally, we conclude this thesis with a description of how such a revised version of CED might be employed to optimize the operation of the newly developed free-space self-amplified spontaneous emission (SASE) FELs and other devices or systems whose operation may be subtly altered by the advanced forces of the boundary conditions that may emerge as the basis of a more physically realistic version of classical electrodynamics.

7.3 Previous Work

By the early decades of twentieth century, attempts to describe radiation had favored classical field theory over the idea of action-at-a-distance. In the early 1900s the derivations by Lienard and Wiechert offered the first detailed covariant picture of radiation by accelerating point particles. The boundary conditions applicable to this solution have traditionally been taken to follow from Sommerfeld's analysis of the uniqueness of solutions to the wave equation. In 1912, Sommerfeld established the radiation condition [64], a boundary condition applied outside the volume occupied by radiating charges, which he applied to analyze the implications of the advanced solutions to the wave equation. Sommerfeld's analysis concluded by requiring that advanced solutions outside this far off boundary must be excluded to achieve uniqueness [64], and that result has continued to be relied upon through present date.

Although the Sommerfeld radiation condition holds a very strong position in the classical theory of radiation, there have been cases where it has been enforced unnecessarily. For example, the advanced solutions for cases of radiation in conducting cavities were ignored until Einstein argued that the advanced and retarded solutions to Maxwell equations were critical to conservation of energy and momentum for a radiating particle in a "box" (conducting cavity) [65] which served as the intellectual basis for the subsequent treatment of radiation into microwave and laser cavities by Slater, Lamb and Siegman [66, 67, 43]. It is of great interest to us that Einstein's original remarks and the subsequent cavity analyses were not intended to deal with the case of radiation into free-space [68], therefore most classical analysis of radiating sources completely ignored the effect of an absorbing media in the system until the analysis by Wheeler and Feynman.

Similarly, it has also been brought to our attention that the Wheeler and Feynman analysis has been criticized for not agreeing with Sommerfeld's radiation condition [69]. Nonetheless it must be noted that a main requirement of Wheeler and Feynman's analysis is that the radiation fields of all the accelerated charges in the Universe are to be specified as

one half of the advanced plus one half of the retarded solutions to the inhomogeneous wave equation. Since the relative contributions of the advanced and retarded solutions are specified in this model, there can be no ambiguity regarding the fields that are actually present in the system, and as further shown by Wheeler and Feynman, superposition of these fields yields the retarded field of experience at large distances from the radiating charge.

Sommerfeld's condition was intended to restrict solutions to the wave equation to yield only the retarded fields of experience but Wheeler and Feynman's assumption of half-advanced plus half-retarded fields, while leading to the same retarded field of experience at large distances from the source, also provides a nonlocal field in the vicinity of accelerated charges attributable to the advanced fields of the absorbing boundaries needed to achieve compliance with Maxwell's equations. The key failing of Sommerfeld's radiation condition is that it rules out this nonlocal field and thus can not generate the fields needed to satisfy Maxwell's equations for the case of coherent radiation.

The continuing efforts to identify an approach to the forces needed to insure compliance with Maxwell's equations in the case of accelerated single charges, which began with Abraham and Lorentz [54, 55] and continues through current date [53], also appears to have been limited by the imposition of Sommerfeld's radiation condition as exemplified by the failure of Larmor's theorem to account for the restriction of radiation by such elementary charges to the eigenfrequencies of the closed conducting or reflecting cavities in which they find themselves [70], an effect that cannot be understood without consideration of the effects of the advanced forces and boundary conditions in these systems.

Thus, it seems to have been Wheeler and Feynman's exploration of the action-at-a-distance model of electrodynamics that has helped to clarify the physical effects needed to resolve these problems. Though starting from a model of the interactions of charged particles that makes no references to electric or magnetic fields, only to the forces acting between these particles, it was established by Gauss [71], Schwarzschild [72], Tetrode [73] and Fokker [74, 75, 76] that descriptions of electrodynamics based on such action-at-a-distance models could be developed that were self-consistent, causal, and fully consistent with Maxwell's equations and thus consistent with the experimental basis of these equations.

To explain the instantaneous loss of energy that must occur in the course of radiation by an accelerated elementary charged particle, Wheeler and Feynman noted in their paper that this objective could only be achieved through the introduction of an advanced force acting between the emitting and absorbing particles [77]. In further consideration of Einstein's arguments concerning the role of thermodynamics in determining the direction of the arrow

of time in electrodynamics, Wheeler and Feynman also postulated that the fields generated by isolated charges should be time symmetric, including equal components of the advanced and retarded solutions to interactions governed by Maxwell's equations [78]. Wheeler and Feynman's final step was to evaluate the forces that would appear in the vicinity of an accelerated charged particle as a consequence of its interactions with a surrounding ensemble of passively accelerated - and thus absorbing - charged particles whose motion responded to the forces attributable to a single, periodically accelerated test charge [79].

It has long been known that Wheeler and Feynman's approach leads to an expression for a force at the position of a periodically accelerated charge that is in phase with its velocity and has an amplitude precisely equal to the amplitude needed to insure consistency with Maxwell's equations and conservation of energy in such systems without the fundamental divergences of the earlier model of Abraham and Lorentz [80]. Wheeler and Feynman also pointed out that the interference of the advanced and retarded force-fields in such a system would lead to a final result in which an observer at large distances from the accelerated charge (compared to a wavelength at the frequency of oscillation) would see that the propagating force fields in the system would coalesce to form what appeared to be a single, retarded force field propagating towards the absorbing charges with an amplitude and phase corresponding to the retarded solution of Lienard and Wiechert. Thus consistency is achieved both with "every day" experience [81] and Einstein's hypothesis that the introduction of an irreversible thermodynamics process—dissipation—into such an otherwise time symmetric system would unambiguously establish a direction to the arrow of time in the evolution of the dynamics of the system [59].

What was noted [81] but not identified as significant by Wheeler and Feynman at the time was the existence in the vicinity of the periodically oscillating charge of a nonlocal force field owing its origins to the incomplete interference of the multiple advanced and retarded forces attributable to the multiple interacting particles in the system whose spatially dependent amplitude and phase is precisely that needed to insure compliance with Maxwell's equations in the case of the coherent radiation emitted by pairs of spatially separated but synchronously oscillating pairs of the elementary charges.

It is only now with the emergence of powerful new electron beam radiation sources based on the mechanism of coherent emission into free-space that we have come to appreciate this last consequence of Wheeler and Feynman's model. In contrast, absent the advanced forces and boundary conditions incorporated within Wheeler and Feynman's model of electrodynamics, the fields computed following conventional field-based CED as further restricted by

Sommerfeld's radiation condition have neither the spatially-dependent amplitudes or phases to achieve compliance with Maxwell's equations in the case of coherent radiation.

While Wheeler and Feynman subsequently discarded their model based on their inability to find a means by which it could serve as the basis of a self-consistent quantized version of electrodynamics [82] along the lines of the approach subsequently followed by Schwinger, Feynman and Tomonaga in developing the modern theory of quantum electrodynamics, that decision may have been premature given Hoyle and Narlikar's recent demonstration that Wheeler and Feynman's action-at-a-distance model could in fact serve as the basis of an alternative, divergence-free version of QED [83, 68].

There is obviously motivation in these developments for further critical analyses and reviews that go far beyond the objective of this document, defined pursuant to the abstract and introduction above to explore by means of analysis and experiment whether the alternative model of electrodynamics of Wheeler and Feynman can provide a solution to the description of coherent emission into free-space that is consistent with Maxwell's equations, but has so far eluded the efforts based on the principles and methods of conventional, field-based CED.

CHAPTER 8
CONSIDERING TWO COHERENTLY OSCILLATING CHARGED PARTICLES

Many classical electrodynamics textbooks introduce the failure of classical electrodynamics at the scale of 2.8 femtometers, where the electron as a point particle would carry infinite electrostatic energy (page 751 of [58]), and argue that the problem lies with the failure of classical physics at small scales. Here we demonstrate that for coherently radiating particles, the failure of *retarded only* CED is far more serious than the well-known failure of CED at small scales.

8.1 Radiated Power and Electric Fields of Periodically Oscillating Charges

When in equilibrium, the electromagnetic time-averaged energy stored within a spherical shell surrounding a periodically oscillating charge is constant, requiring that the time-averaged surface integral of the Poynting vector must be equal to the time-averaged volume integral of $\mathbf{E} \cdot \mathbf{j}$ within the sphere.

$$-\int_A^B dt \frac{d}{dt} \int \frac{1}{8\pi}\left[E^2 + H^2\right] dV =$$

$$\int_A^B dt \left[\int \frac{c}{4\pi}\mathbf{E} \times \mathbf{H} \, d\mathbf{a} + \int \mathbf{E} \cdot \mathbf{j} \, dV \right],$$

(8.1)

if A and B are separated by an integral number of periods of the oscillation of the charges, then

$$\int_A^B dt \frac{d}{dt} \int \frac{1}{8\pi}\left[E^2 + H^2\right] dV = 0$$

(8.2)

$$\Rightarrow \int_A^B dt \int \frac{c}{4\pi}\mathbf{E} \times \mathbf{H} \, d\mathbf{a} = -\int_A^B dt \int \mathbf{E} \cdot \mathbf{j} \, dV.$$

The surface integral of the Poynting vector can thus be used to infer the amplitude of the electric field acting on the electrons in phase with their velocities [84]. The equilibrium

between the time-averaged radiated power as calculated using Poynting's vector and the work done on the radiating charges by the electric field they generate subject to the relevant boundary conditions is thus a requirement that follows directly from Maxwell's equations (page 179 of [60]), and requires the rigorous detailed balance of these two quantities.

Eqs. (8.1) and (8.2) are exact and complete without the addition of any other fields or forces. More general statements of energy conservation can be and have been developed through the use of these equations in combination with the Lorentz force law. Although in this thesis we do not rely on these more general statements, we have cited several authors who have used such theorems in their analysis.

Radiated Power by Two Coherently Oscillating Charged Particles Displaced by Distance r in an Arbitrary Direction

If the two coherently oscillating charged particles are displaced by distance r at angle α to their direction of motion, the integral of Poynting vector becomes Eq. (8.3). When the charges oscillate perpendicular to the direction of their separation vector, $\alpha = \pi/2$, and the power is given by Eq. (8.4).

$$P_{Radiated}(\alpha) \propto 2 \int_0^{2\pi} \int_0^{\pi} \sin^3(\theta) \times \cos^2\left(\frac{kr(\cos(\theta)\cos(\alpha) + \sin(\theta)\sin(\alpha)\cos(\phi))}{2}\right) d\theta d\phi \quad (8.3)$$

$$P_{Radiated}(\alpha = \pi/2) \propto 2 \int_0^{2\pi} \int_0^{\pi} \sin^3(\theta) \times \cos^2\left(\frac{kr(\sin(\theta)\cos(\phi))}{2}\right) d\theta d\phi \quad (8.4)$$

where $k = \frac{\omega}{c}$.

Consider the geometry of the case presented in Fig. 8.1, where two charged particles are oscillating in phase and are separated by distance r in the direction parallel to the direction of their oscillation, λ (wavelength of the oscillating motion) is approximately a micron, [$\mathbf{x}_1(t)$ and $\mathbf{x}_2(t)$ are the amplitude of of oscillation, and r is the magnitude of $\mathbf{r}$]. The power radiated by this system, $P = \frac{c}{4\pi} \int \mathbf{E} \times \mathbf{H} \cdot d\mathbf{a}$, integrated over the surface of a large diameter sphere centered on midpoint between the two charges is
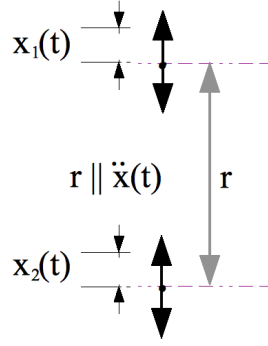
Figure 8.1: Two coherently oscillating charged particles with distance r between the centers of their oscillation, and amplitude of oscillation of $x(t)$, where $\mathbf{r}$ is parallel to the direction of oscillation $[\mathbf{x}_1(t) = \mathbf{x}_2(t) = \mathbf{x}(t) = x_0\cos(\omega t)\hat{\mathbf{y}}]$.
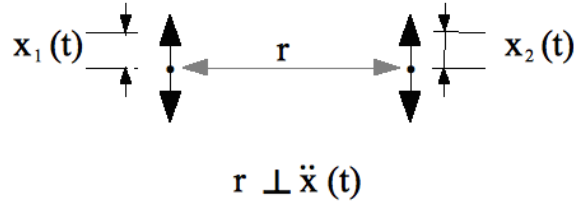
Figure 8.2: Two coherently oscillating charged particles with distance r between the centers of their oscillation, and amplitude of oscillation of $x(t)$, where $\mathbf{r}$ is normal to the direction of oscillation $[\mathbf{x}_1(t) = \mathbf{x}_2(t) = \mathbf{x}(t) = x_0\cos(\omega t)\hat{\mathbf{y}}]$.

$$P = \frac{e^2\ddot{x}_0^2}{c^3}\int_0^\pi \sin^3(\theta)\cos^2[\frac{\omega r}{c}\frac{\cos(\theta)}{2}]d\theta,$$

$$(8.5)$$

$$= \frac{e^2\ddot{x}_0^2}{c^3}[\frac{2}{3} - \frac{2\cos[\frac{\omega r}{c}]}{(\frac{\omega r}{c})^2} + \frac{2\sin[\frac{\omega r}{c}]}{(\frac{\omega r}{c})^3}].$$

When the separation $r = 0$, the total time-averaged power radiated by the two electrons is $\frac{4e^2\ddot{x}_0^2}{3c^3}$ which is used to normalize Eq. (8.5) in the subsequent plots. The normalized power radiated by these two coherently oscillating charged particles is shown in Fig. 8.3 as a

function of their separation.

Since, as shown in Fig. 8.3, the time-averaged power radiated by the particles varies with their separation, there must be an electric field acting on the two electrons that oscillates in phase with their velocities and has an amplitude that varies with spacing to match the variation with spacing of their radiated power [85]. We can then ask the question of whether any of the existing theories for the radiation reaction field provide an estimate of that force, which agrees with the electrons' radiated power and has the same variation of power with the vector separation of the two charges.

8.2   Role of the Induction Field

According to Sommerfeld's *retarded only* formulation of electrodynamics, the electric fields generated by the periodically oscillating charges in the model of coherent radiation shown in Fig. 8.1 include the charges' individual Abraham-Lorentz-Dirac self-fields, their retarded Lienard-Wiechert radiation and the induction fields. For the assumed case of "radiation into free-space," the only charges whose fields can contribute to the integrals of Eq. (8.1) and (8.2) are the two charges shown in Fig. 8.1, with no contribution from any of the possible boundaries which might be present in a more physically realistic model.

Since, for the alignment of the charges shown in Fig. 8.1, there is no component of the particles' radiation fields along the axis on which they are positioned, the particles' radiation fields cannot contribute to the radiation reaction force needed to conserve energy for the case of radiation into free-space. The retarded electric induction field, however, does include an oscillating component when evaluated for oscillations of small amplitude compare to the wavelength and the distance separating the oscillating charges ($x_0 << \lambda$ and $x_0 << r$). The retarded induction field acting on one of the particles due to the other is

$$\mathbf{E}(\mathbf{x}, t) = e \left[\frac{\hat{\mathbf{n}} - \boldsymbol{\beta}}{\gamma^2 (1 - \boldsymbol{\beta} . \boldsymbol{n})^3 R^2} \right]_{ret}, \tag{8.6}$$

from page 664 of [58], where

$$R = r + \delta r, \tag{8.7a}$$

$$\delta \mathbf{r} = \mathbf{x_1}(t) - \mathbf{x_2}(t_{ret}), \tag{8.7b}$$

$$t_{ret} = t - \frac{R}{c} = t - \frac{r + \delta r}{c}. \tag{8.7c}$$

In Eq. (8.7a), R is the retarded distance of the two particles from the perspective of the first particle at present time and the second particle at $t_{ret} = t - \frac{R}{c}$. Expanding terms in the denominator of Eq. (8.6) and keeping only the lowest order terms in x_0 and δr we evaluate the volume integral of $\mathbf{E} \cdot \mathbf{j}$,

$$P_{ind} \quad = \quad < e \, \mathbf{E}_{2_{ret}} \cdot \dot{\mathbf{x}}_1(t) >, \tag{8.8}$$

which has a dependence on particle spacing r and is plotted in Fig. 8.5. Here and in the rest of this document, we use the $<>$ notation instead of the $\int_A^B dt$ for integer intervals in Eqs. (8.1) and (8.2) .

8.2.1   Derivation for the Case $\dot{\beta} \parallel r$

To calculate and plot the volume integral of $\mathbf{E} \cdot \mathbf{j}$ at the position of particle 1 due to the induction field of particle 2 (as shown in Fig. (8.1)), we use Eq. (8.6) and (8.7a)–(8.7c). Since $\ddot{x} \parallel r$, $(\beta \parallel n)$ and $\beta << 1$, $(\gamma^{-2} \approx 1)$, Eq. (8.6) can be rewritten as

$$\mathbf{E_2}(\mathbf{x}, t) = e \left[\frac{\hat{\mathbf{n}}(1 + 2\beta)}{R^2} \right]_{ret}. \tag{8.9}$$

The first order approximation of Eq. (8.7a) also reduces the R^{-2} term to $r^{-2}(1 - 2\frac{\delta r}{r})$, which reduces Eq. (8.9) to

$$\mathbf{E_2}(\mathbf{x}, t) = e \left[\frac{\hat{\mathbf{n}}(1 + 2\beta)(1 - 2\frac{\delta r}{r})}{r^2} \right]_{ret}, \tag{8.10}$$

where $\boldsymbol{\beta} = \frac{\dot{\mathbf{x}}}{c}$. Since now we have $\delta t = (r + \delta r)/c$, Eq. (8.7b) can be rewritten as

$$\delta \mathbf{r} \quad = \mathbf{x_1}(t) - \mathbf{x_2}(t - \tfrac{r}{c}) + \tfrac{\delta r}{c} \dot{\mathbf{x}}_2(t - \tfrac{r}{c}). \tag{8.11}$$

Since $\delta \mathbf{r}$, $\mathbf{x_1}$, $\mathbf{x_2}$, and $\dot{\mathbf{x}}_\mathbf{2}$ are all in the same direction ($\hat{\mathbf{y}}$) we drop the vectors notation. Solving for δr:

$$
\begin{aligned}
\delta r &= \frac{x_1(t) - x_2(t - \frac{r}{c})}{1 - \frac{1}{c}\dot{x}_2(t - \frac{r}{c})} \\
&\approx (x_1(t) - x_2(t - \frac{r}{c}))(1 + \frac{1}{c}\dot{x}_2(t - \frac{r}{c})),
\end{aligned} \tag{8.12}
$$

and keeping only the first order term, we have

$$
\delta r = x_1(t) - x_2(t - \frac{r}{c}), \tag{8.13}
$$

and

$$
\delta t = \frac{1}{c}(r + x_1(t) - x_2(t - \frac{r}{c})). \tag{8.14}
$$

So Eq. (8.10), the retarded induced field due to the 2nd particle will become

$$
\mathbf{E_{2_{ret}}}(\mathbf{x}, t) = \frac{e\hat{\mathbf{n}}(1 + 2\frac{\dot{x}_2}{c})(1 - 2\frac{x_1(t) - x_2(t - \frac{r}{c})}{r})}{r^2}, \tag{8.15}
$$

where $\dot{x}_2$ is evaluated at t_{ret}. We consider the general oscillating motion where $u_o = \omega x_o$ and $a_o = \omega^2 x_o$:

$$
x = x_o \cos(\omega t) \tag{8.16a}
$$
$$
u = -u_o \sin(\omega t) \tag{8.16b}
$$
$$
a = a_o \cos(\omega t). \tag{8.16c}
$$

Then explicitly evaluating the retarded E_2 in terms of x_1 and x_2, we have

$$
\mathbf{E_{2_{ret}}}(\mathbf{x}, t) = \frac{e\hat{\mathbf{n}}}{r^2}\left[1 - \frac{2\omega x_o}{c}\sin(\omega(t - \frac{r}{c})) + \frac{2x_0}{r}\left[\cos(\omega t) - \cos(\omega(t - \frac{r}{c}))\right]\right]. \tag{8.17}
$$

Using Eq. (8.8), we evaluate the induced power using

$$< e\ \mathbf{E_{2_{ret}}}\cdot\dot{\mathbf{x}}_1(t) >$$

$$=< \frac{e^2\omega x_o \sin(\omega t)}{r^2}\left[1 - \frac{2\omega x_o}{c}\sin(\omega(t - \frac{r}{c})) + \frac{2x_0}{r}\left[\cos(\omega t) - \cos(\omega(t - \frac{r}{c}))\right]\right] >$$

$$=< \frac{e^2\omega x_o \sin(\omega t)}{r^2}\left[1 - \frac{2\omega x_o}{c}\sin(\omega(t - \frac{r}{c})) + \frac{2x_0}{r}\left[\cos(\omega t) - \cos(\omega t)\cos(\frac{\omega r}{c}) - \sin(\omega t)\sin(\frac{\omega r}{c})\right]\right] >$$

$$=< \frac{e^2\omega x_o \sin(\omega t)}{r^2}\left[1 - \frac{2\omega x_o}{c}\left[\sin(\omega t)\cos(\frac{\omega r}{c}) - \cos(\omega t)\sin(\frac{\omega r}{c})\right] - \frac{2x_0}{r}\left[\sin(\omega t)\sin(\frac{\omega r}{c})\right]\right] >$$

$$=< \frac{e^2\omega x_o \sin(\omega t)}{r^2}\left[1 - \frac{2\omega x_o}{c}\left[\sin(\omega t)\cos(\frac{\omega r}{c})\right] - \frac{2x_0}{r}\left[\sin(\omega t)\sin(\frac{\omega r}{c})\right]\right] >$$

$$(8.18)$$

and after expanding and dropping all the $\cos(\omega t)$ terms in $\mathbf{E_{2_{ret}}}$ that result from $< \cos(\omega t)\sin(\omega t) >= 0$ for those terms, shown by (8.18) we have

$$P_{ind,ret} = \frac{e^2\omega x_o^2}{r^2}\left[-\frac{\omega}{c}\cos(\frac{\omega r}{c}) - \frac{1}{r}\sin(\frac{\omega r}{c})\right],\qquad(8.19)$$

which is plotted in Fig. 8.5.

As is evident from Fig. 8.5, the force due to the induction field fails to comprise a component of the radiation reaction force, not only because it is not in phase with the reaction force as inferred by Fig. 8.3, but also because it diverges as the particles' separation approaches zero. The only way to cancel this divergence is to add a component to the field equal to the advanced component of the Lienard-Wiechert induction fields which has a divergence of the opposite sign. If that advanced component is also added to the two particles' radiation fields, however, the two particle system no longer emits any induced radiation.

In principle, Sommerfeld's *retarded only* formulation of electrodynamics could be extended to include the fields generated by reflection of the outgoing radiation fields of the oscillating charges in Fig. 8.1 from the physical boundaries that might exist in more physically realistic situations. But those fields could not appear at the position of the oscillating charges in Fig. 8.1 until the retarded radiation fields of the oscillating charges in Fig. 8.1 had enough time to propagate outwards (towards those boundaries), and the retarded radiation fields of the charges and currents in the physical boundaries had the time needed to propagate back towards the oscillating charges in Fig. 8.1. For distant boundaries, the "out and back" propagation delay times would foreclose the possibility of satisfying the constraints

that follow from Eqs. (8.1) and (8.2) at intermediate times. For such shorter times, the outcome would still manifestly violate the strict equivalence of the time-averaged volume integral of $\mathbf{E} \cdot \mathbf{j}$ and the time-averaged surface integral of $\mathbf{E} \times \mathbf{H}$. Sommerfeld's *retarded only* formulation of electrodynamics is thus fundamentally incapable of achieving consistency with Maxwell's equations for the case of coherent emission.

Advanced Component of the Radiation Reaction Force from the Induction Field

Consider the advanced term:

$$\mathbf{E_2}(\mathbf{x}, t) = e \left[\frac{\hat{\mathbf{n}}(1 + 2\beta)(1 - 2\frac{\delta r}{r})}{r^2} \right]_{adv}. \tag{8.20}$$

For

$$t_{adv} = -t - \delta t, \tag{8.21}$$

the advanced induced field due to the 2nd particle is

$$\mathbf{E_{2_{adv}}}(\mathbf{x}, t) = \frac{e\hat{\mathbf{n}}(1 + 2\frac{\dot{x}_2}{c})(1 - 2\frac{x_1(t) - x_2(-t - \frac{r}{c})}{r})}{r^2}, \tag{8.22}$$

where $\dot{\mathbf{x}}_2$ is evaluated at t_{adv}. Then $P_{ind,adv}$ can be calculated just as $P_{ind,ret}$ was in (8.18).

$$P_{ind,adv} = \frac{e^2 \omega x_o^2}{r^2} \left[\frac{\omega}{c} \cos(\frac{\omega r}{c}) + \frac{1}{r} \sin(\frac{\omega r}{c}) \right]. \tag{8.23}$$

Since $P_{ind,adv}$ yields the exact value as the $P_{ind,ret}$ except with an opposite sign ($P_{ind,adv} = -P_{ind,ret}$) therefore $P_{ind,total} = 0$. So when including $\mathbf{E_{2_{adv}}}$ in calculating $< e \, \mathbf{E}_2 \cdot \dot{\mathbf{x}}_1(t) >$, the power extracted from the oscillating charge is zero.

8.2.2 Derivation for the Case $\dot{\beta} \perp r$

Derivation in the case shown in Fig. (8.2) is more straight forward. In this case we have to use Eq. (8.24), the full Lienard-Wiechert retarded potential from [58],

$$\mathbf{E}(\mathbf{x}, t) = e \left[\frac{\hat{\mathbf{n}} - \boldsymbol{\beta}}{\gamma^2(1 - \boldsymbol{\beta}.\boldsymbol{n})^3 R^2} + \frac{\hat{\mathbf{n}} \times [(\hat{\mathbf{n}} - \boldsymbol{\beta}) \times \dot{\boldsymbol{\beta}}]}{cR(1 - \boldsymbol{\beta}.\boldsymbol{n})^3} \right]_{ret} \tag{8.24}$$

Now with $\mathbf{x}(t) = x_0 \cos(\omega t)\hat{\mathbf{y}}$, $\boldsymbol{\beta}$ and $\dot{\boldsymbol{\beta}}$ would be $\frac{-\omega x_0}{c} \cos(\omega t)\hat{\mathbf{y}}$ and $\frac{\omega^2 x_0}{c} \cos(\omega t)\hat{\mathbf{y}}$. Again taking $R = r + \delta r$, we will have three terms contributing to the total extracted power: 1) power from the self force, 2) induced power, and 3) radiated power. Fig. (8.6) shows that, in this case, also there is no agreement between the Lienard-Wiechert retarded potential and power extracted from Eq. (8.2). Fig. (8.6) is normalized to $\frac{2e^2 \ddot{x}_0^2}{3c^3}$.

$$P_{self} = \frac{2e^2 \ddot{x}_0^2}{3c^3}, \tag{8.25a}$$

$$P_{ind} = \frac{2e^2 \ddot{x}_0^2}{2c^3} \frac{\left(-\left(\frac{\omega r}{c}\right) \cos\left(\frac{\omega r}{c}\right) + \sin\left(\frac{\omega r}{c}\right)\right)}{\left(\frac{\omega r}{c}\right)^3}, \tag{8.25b}$$

$$P_{rad} = \frac{2e^2 \ddot{x}_0^2}{2c^3} \frac{\sin\left(\frac{\omega r}{c}\right)}{\left(\frac{\omega r}{c}\right)}. \tag{8.25c}$$

8.3 Dirac's Solution

In his 1938 "Classical Theory of Radiating Electrons" [86], Dirac proposed an expression for the "radiation reaction field (rrf)" of a single particle, needed to insure energy conservation:

$$\mathbf{F}_{Dirac-rrf} \propto \frac{[\exp(iu) - \exp(-iu)]}{u}. \tag{8.26}$$

where $u = kr$ for our physical interpretation. While this seems to have been a key step in the right direction for explaining the phenomena of radiation in free-space, Dirac did not disclose the physical basis for his radiation reaction field. Dirac's motivation for expressing Eq. (8.26) as half the difference of the advanced and retarded components of the field seems purely mathematical.

Dirac noted that the real part of the radiated Lienard-Wiechert field at the position of the particle is 90 deg out of phase with the particle's velocity. The imaginary part, on the other hand, is in phase with the particle's velocity and is therefore capable of reducing the particle's kinetic energy during the process of radiation. By evaluating half the difference of the advanced and retarded solutions for the field equations he was able to demonstrate that the electric field at $r = 0$ had precisely the value required to insure conservation of energy. Although Dirac's radiation reaction field at finite values of r in the near field is also defined

by Eq. (8.26), these values are only close to what is required for energy balance for coherent emission in vicinity of the particle.

Dirac's field fails in two ways to account for the power actually radiated by a pair of coherently oscillating charged particles. Since such charges emit no electric fields along the direction of their acceleration, the Dirac model is not capable of satisfying Eq. (8.2) for vector displacements parallel to the direction of the charges' oscillation as in Figs. 8.1 and 8.3. So in the case of two particle oscillating coherently with r being parallel to direction of oscillation, Dirac's formula does not provide a suitable solution as demonstrated in Fig. 8.7. Also as stated, the Dirac field for two coherently oscillating charges,

$$P_{Dirac-rrf,2e} =$$
$$< 2\mathbf{F}_{Dirac-rrf}(0,t) \cdot \dot{\mathbf{x}}(t) > +$$
$$< 2\mathbf{F}_{Dirac-rrf}(\frac{\omega r}{c},t) \cdot \dot{\mathbf{x}}(t) > \qquad (8.27)$$
$$\propto \frac{1 + \frac{\sin(\frac{\omega r}{c})}{\frac{\omega r}{c}}}{2},$$

does not match the variation of coherently radiated power by particles with vector separations r normal to the direction of acceleration as shown in Fig. 8.8.

8.4   Wheeler and Feynman Approach

Fortunately, Dirac's radiation reaction field inspired Wheeler and Feynman to more directly explore the physical basis of the radiation reaction field for point particles. In their 1945 paper, Wheeler and Feynman were able to demonstrate that, when formulated in the language of covariant action-at-a-distance, the solution of the boundary value problem corresponding to an oscillating particle within a spherical absorbing shell (representing free-space) of arbitrary composition and at an arbitrary distance from the radiating charge was dominated by the interference of the retarded and advanced forces originating in the accelerated and absorbing particles. By including both advanced and retarded solution for the source and absorber they were able to define a radiation reaction force exactly equal to that needed to match the power carried by radiation to the particles in the absorbing shell (see Appendix A for details) that was independent of the positions of the absorbing boundaries, in contrast to the "out and back" delay that characterizes the interactions of radiating charges and boundary conditions in Sommerfeld's *retarded only* formulation of electrodynamics."

Wheeler and Feynman identify Eq. (B.1a) as the force field for the radiation reaction

field (rrf) for a single particle which is also finite when $r = 0$. They explicitly note that the adjunct field they had derived converged to Dirac's radiation reaction field at $r = 0$ and also at large distances from the accelerated particle. Despite that they do not mention that their adjunct radiation reaction field diverged from Dirac's radiation reaction field at distances between a few tenths of a wavelength and 4-5 wavelengths. Nevertheless, based on Eq. (B.1a), the total power of $\mathbf{F}_{WF-rrf}$ for the system of two coherently oscillating charged particles is

$$P_{WF-rrf,2e} =$$
$$< 2\mathbf{F}_{WF-rrf}(0,t) \cdot \dot{\mathbf{x}}(t) > + \tag{8.28}$$
$$< 2\mathbf{F}_{WF-rrf}(\frac{\omega r}{c},t) \cdot \dot{\mathbf{x}}(t) > .$$

8.4.1 Derivation for the Case $\dot{\beta} \parallel r$

To evaluate $P_{WF-rrf,2e}(\frac{\omega r}{c})$ explicitly for the case shown in Figs. 8.1 and 8.3, we start from Eq. (B.1a). In this case, $P_2(\cos(\mathbf{a}, r)) = 1$. Because $\cos(\mathbf{a}, d)$ is the cosine of the angle between $\mathbf{a}$ (acceleration of the oscillating charges with amplitude a_0) and r and since the particles are oscillating parallel to the direction of motion $\cos(\mathbf{a}, r) = 1$ and $P_2(x) = \frac{1}{2}(-1 + 3x^2) \Rightarrow P_2(0) = 1$, therefore Eq. (B.1a) becomes:

$$F_{WF-rrf}(\frac{\omega r}{c}, t) =$$
$$\frac{2e^2}{3c^3}(-i\omega a_0)\exp(-i\omega t)\,[F_0(\frac{\omega r}{c}) - F_2(\frac{\omega r}{c})]. \tag{8.29}$$

Evaluating Eq. (B.1b) and (B.1c) and substituting in Eq. (8.35), we will have

$$F_{WF-rrf}(\frac{\omega r}{c}, t) =$$
$$\frac{2e^2}{3c^3}(-i\omega a_0)\exp(-i\omega t) \times \Big[\frac{\sin[\frac{\omega r}{c}]}{(\frac{\omega r}{c})} - \frac{3\cos[\frac{\omega r}{c}]}{(\frac{\omega r}{c})^2} + \frac{(3 - (\frac{\omega r}{c})^2)\sin[\frac{\omega r}{c}]}{(\frac{\omega r}{c})^3}\Big], \tag{8.30}$$

which simplifies to

$$F_{WF-rrf}(\frac{\omega r}{c}, t) =$$
$$\frac{2*3*e^2}{3c^3}(-i\omega a_0)\exp(-i\omega t) \times \Big[-\frac{\cos[\frac{\omega r}{c}]}{(\frac{\omega r}{c})^2} + \frac{\sin[\frac{\omega r}{c}]}{(\frac{\omega r}{c})^3}\Big]. \tag{8.31}$$

The term in the bracket at $r = 0$ converges to: $\lim_{x \to 0} \left[\frac{\sin[x]}{x^3} - \frac{\cos[x]}{x^2} \right] = \frac{1}{3}$. Therefore, for a periodic oscillation with $\dot{x} = -\omega x_0 \sin(\omega t)$

$$< 2\mathbf{F}_{WF-rrf}(0,t) \cdot \dot{\mathbf{x}}(t) >= \frac{2e^2 \omega a_0}{3c^3} \omega x_0 = \frac{2e^2 \ddot{x}_0^2}{3c^3}, \tag{8.32}$$

and for any value of r we have:

$$< 2\mathbf{F}_{WF-rrf}(\frac{\omega r}{c},t) \cdot \dot{\mathbf{x}}(t) >= \frac{2e^2 \ddot{x}_0^2}{c^3} \left[-\frac{\cos[\frac{\omega r}{c}]}{(\frac{\omega r}{c})^2} + \frac{\sin[\frac{\omega r}{c}]}{(\frac{\omega r}{c})^3} \right]. \tag{8.33}$$

For comparison, the total power for the system of two coherently oscillating charged particles separated by the distance r is

$$P_{WF-rrf,2e} = \frac{e^2 \ddot{x}_0^2}{c^3} \left[\frac{2}{3} - \frac{2\cos[\frac{\omega r}{c}]}{(\frac{\omega r}{c})^2} + \frac{2\sin[\frac{\omega r}{c}]}{(\frac{\omega r}{c})^3} \right] \quad . \tag{8.34}$$

which is identical to the result from Eq. (8.5). Both Eq. (8.5) and Eq. (8.34) are compared in Fig. 8.9. The results for the total radiated power of two oscillating charged particles with displacements at right angles to their vector accelerations is evaluated and plotted in Fig. 8.10.

8.4.2 Derivation for the Case $\dot{\beta} \perp r$

To evaluate $P_{WF-rrf,2e}(\frac{\omega r}{c})$ for the case shown in Figs. 8.2, again we start from Eq. (B.1a). In this case, $P_2(\cos(\mathbf{a},r)) = -1/2$. Because $\cos(\mathbf{a},d)$ is the cosine of the angle between $\mathbf{a}$ (acceleration of the oscillating charges with amplitude a_0) and r and since the particles are oscillating perpendicular to the direction of motion $\cos(\mathbf{a},r) = 0$ and $P_2(x) = \frac{1}{2}(-1+3x^2) \Rightarrow$ $P_2(90) = -1/2$, therefore Eq. (B.1a) becomes:

$$F_{WF-rrf}(\frac{\omega r}{c},t) = \frac{2e^2}{3c^3}(-i\omega a_0) \exp(-i\omega t) \left[F_0(\frac{\omega r}{c}) + \frac{1}{2}F_2(\frac{\omega r}{c}) \right]. \tag{8.35}$$

Evaluating Eq. (B.1b) and (B.1c) and same as before, and following the same steps:

$$F_{WF-rrf}(\frac{\omega r}{c}, t) =$$
$$\frac{2e^2}{3c^3}(-i\omega a_0)\exp(-i\omega t) \times \Big[\frac{\sin[\frac{\omega r}{c}]}{(\frac{\omega r}{c})} + \frac{3\cos[\frac{\omega r}{c}]}{2(\frac{\omega r}{c})^2} - \frac{(3-(\frac{\omega r}{c})^2)\sin[\frac{\omega r}{c}]}{2(\frac{\omega r}{c})^3}\Big]. \quad (8.36)$$

We can evaluate the power for this case as well, which is plotted in Fig. (8.10) and is again in perfect agreement with the curve obtained from integral of Maxwell's equations. In fact this formalism yields the correct power for any angle between the charges oscillating coherently.

8.5 Discussion and Analysis

Figures 8.9 and 8.10 suggest that the Wheeler-Feynman model is significant with respect to the process of coherent radiation in free-space, for in contrast to Dirac's field, the Wheeler-Feynman adjunct radiation reaction field—owing its existence to the radiating particle's interactions with the advanced fields of the absorbing boundaries—accounts exactly for the force needed to satisfy Eq. (8.2) when compared with the strongly enhanced radiated power emitted by two coherently oscillating charged particles at varying spacings and angular displacements in their mutual near fields.

It is also important to note that their approach is not offensive to our naive understanding of causality. In the analysis of Wheeler and Feynman, the advanced field of the absorber must be added to half-retarded and half-advanced field of the source. But in their analysis [81], the advanced field of absorber is equal to the difference between the half-retarded and half-advanced fields of the source. Therefore, the superposition of the half-advanced, half-retarded fields of the source and advanced field of the absorber produces the fully retarded field familiar from experience at large distances from the radiating charge.

Based on past critical reviews, the Wheeler-Feynman model of radiation into free-space has been found to be fully compatible with Maxwell's equations, quantum electrodynamics and causality. Therefore, there can be no objection on theoretical grounds to its implication for the reformulation of the more widely accepted field-based CED theory to include the model's half-advanced, half-retarded time symmetric interactions as required to assure consistency with Maxwell's equations. Objections to this reformulation can only be based on experiment. As we describe below, the elementary process of coherent emission provides a good opportunity to perform such a test. We describe one such a test in Sec. IV A (below).

From the theoretical standpoint, the results demonstrated in Sec. III C (Figs. 6 and 7)

strongly suggest that the limitations of established CED radiation theory with respect to the case of coherent radiation in free-space are due to the omission of the radiating particles' interactions via the advanced terms included in the general solution of the inhomogeneous wave equation with the distant charges and currents that absorb that radiation.

This failure is fully consistent with our understanding of the nature of the solutions to inhomogeneous linear differential equations like Maxwell's equations. The general solutions to such inhomogeneous problems are composed of a particular solution to the inhomogeneous equation plus the homogeneous solution needed to satisfy boundary conditions [87]. Accordingly, in field theory, the general solution to radiation problems requires the inclusion of the boundary conditions that fix the values of the solution at the boundaries of the region surrounding the source. Those conditions will differ depending on the nature of the boundary. In the case of conducting cavities, the discrete spectrum of solutions to the homogeneous wave equation which need to be added to the solution of the inhomogeneous wave equation to satisfy the boundary conditions at the conducting walls of the cavity define the nature of the radiation that can be emitted by oscillating charge distributions in the cavity.

The fields which have traditionally been ascribed to the radiation emitted by a single oscillating charge into free-space, constitute a "special solution" to the inhomogeneous wave equation for that problem, but do not include any of the solutions to the homogeneous wave equation needed to fulfill the boundary conditions applicable to the problem, presumably those appropriate to the distant absorbing shell assumed in the Wheeler-Feynman model for free-space. It is thus not a surprise that the fields traditionally attributed to a single oscillating charge without consideration of the relevant boundary conditions, either those of the conducting microwave or reflecting optical cavities long familiar from cavity electrodynamics, or the absorbing walls the anechoic chambers used to simulate radiation into free-space should manifestly fail to comply with the test represented by Maxwell's energy integral in the case of coherent radiation into free-space. Absent the inclusion of the specific homogeneous terms needed to satisfy the boundary conditions applicable to radiation into free-space, there obviously can be no confidence that any special solution to the wave equation for this case can accurately define the fields acting on other oscillating charges in the vicinity of the assumed source charge [88].

Although fully consistent with the generally accepted means of solutions for such inhomogeneous linear differential equations, the results presented in this thesis, if verified by experiment, will require a significant extension of our understanding of the nature of the radiative interactions that occur in the limit of classical electrodynamics. In particular, since

the influence of the absorber at the time the source has just started to radiate is what is responsible for compliance with Maxwell's energy integral, we need to imagine that at the very moment the source begins to oscillate, it is also subject to a connection between itself and its surrounding medium through which energy can be transmitted or shared. Although suggested by theory as elaborated by Wheeler and Feynman, such a radical revision of our understanding of the process of radiation can only be based on experiment.
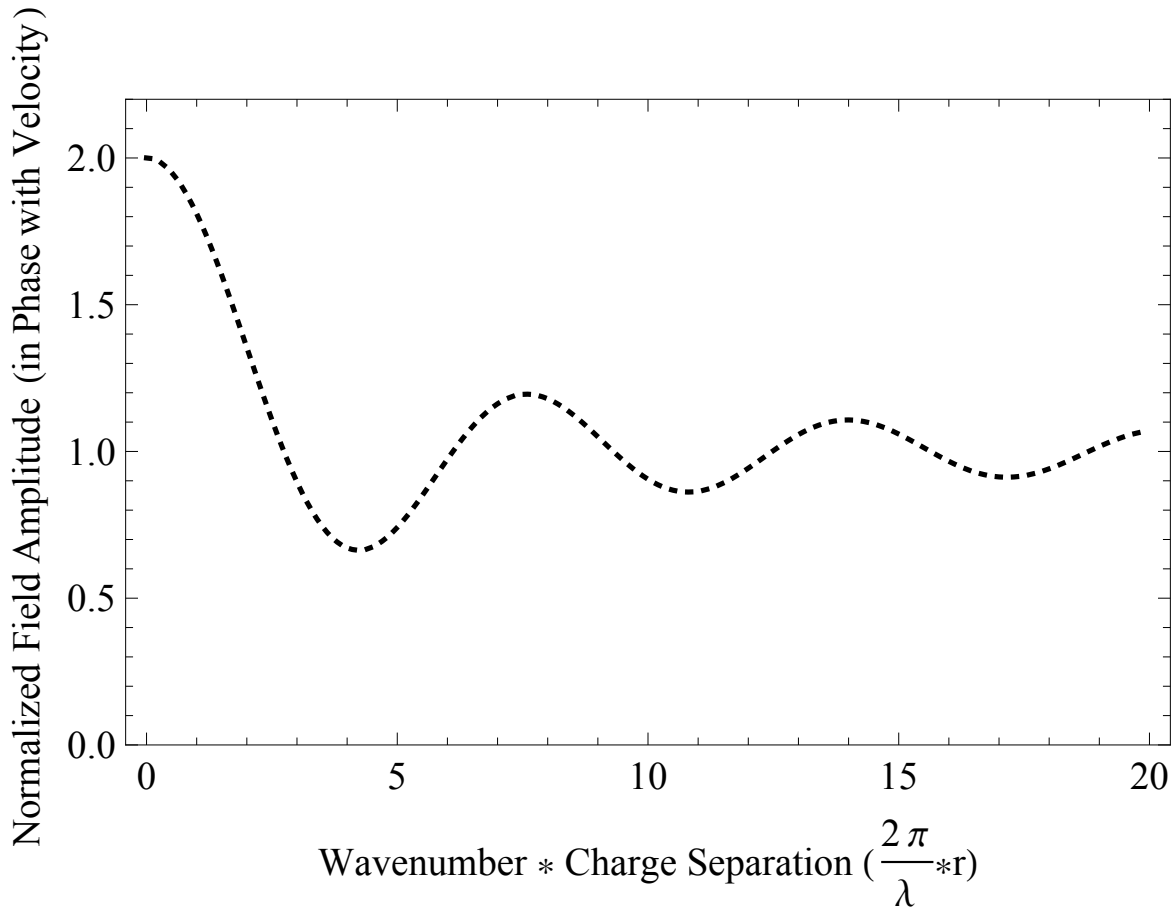
Figure 8.3: Plot of normalized total radiated power from two coherently oscillating charged particles showing dependence on the separation between the center of oscillation of two charges. When $r << \lambda$ the radiated power has twice the magnitude compared to when $r >> \lambda$, or the normalized amplitude of that component of the electric field acting on the individual charges and oscillating in phase with the charge's velocity for charges separated by vector displacements parallel to the direction of their velocities as in Fig. (8.1).
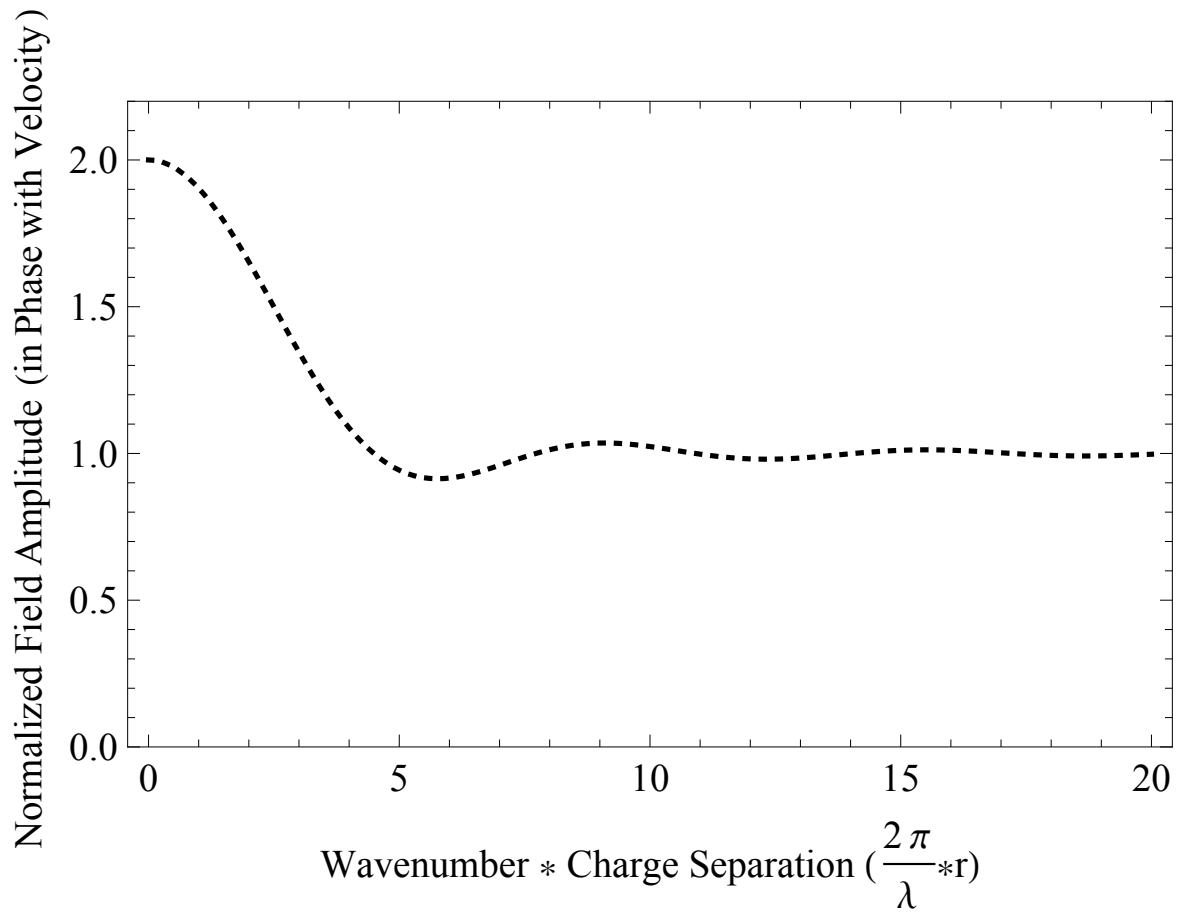
Figure 8.4: Plot of normalized total radiated power from two coherently oscillating charged particles showing dependence on the separation between the center of oscillation of two charges. When $r \ll \lambda$ the radiated power has twice the magnitude compared to when $r \gg \lambda$, or normalized amplitude of that component of the electric field in phase with the velocity of the oscillating charge at the position of one of the oscillating charges in the system shown in Fig. (8.2).
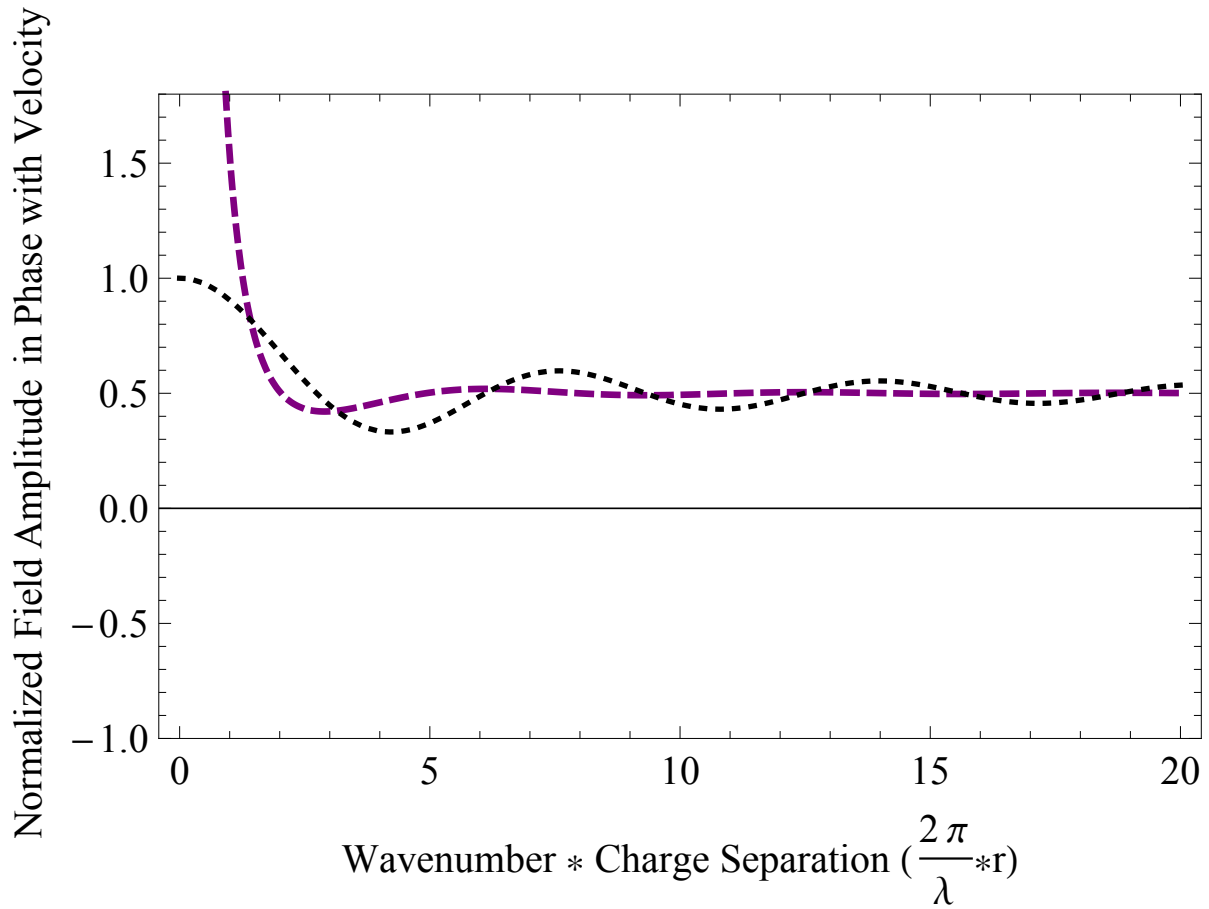
Figure 8.5: The normalized amplitudes of those components of the fields acting on the individual charges in Fig. (8.1) in phase with their velocities calculated using the retarded Lienard Wiechert potentials that determine field amplitudes in Sommerfeld's *retarded only* version of electrodynamics. The divergent field amplitudes at small charge separations compared to the wavelength is due to the charge's retarded Coulomb fields
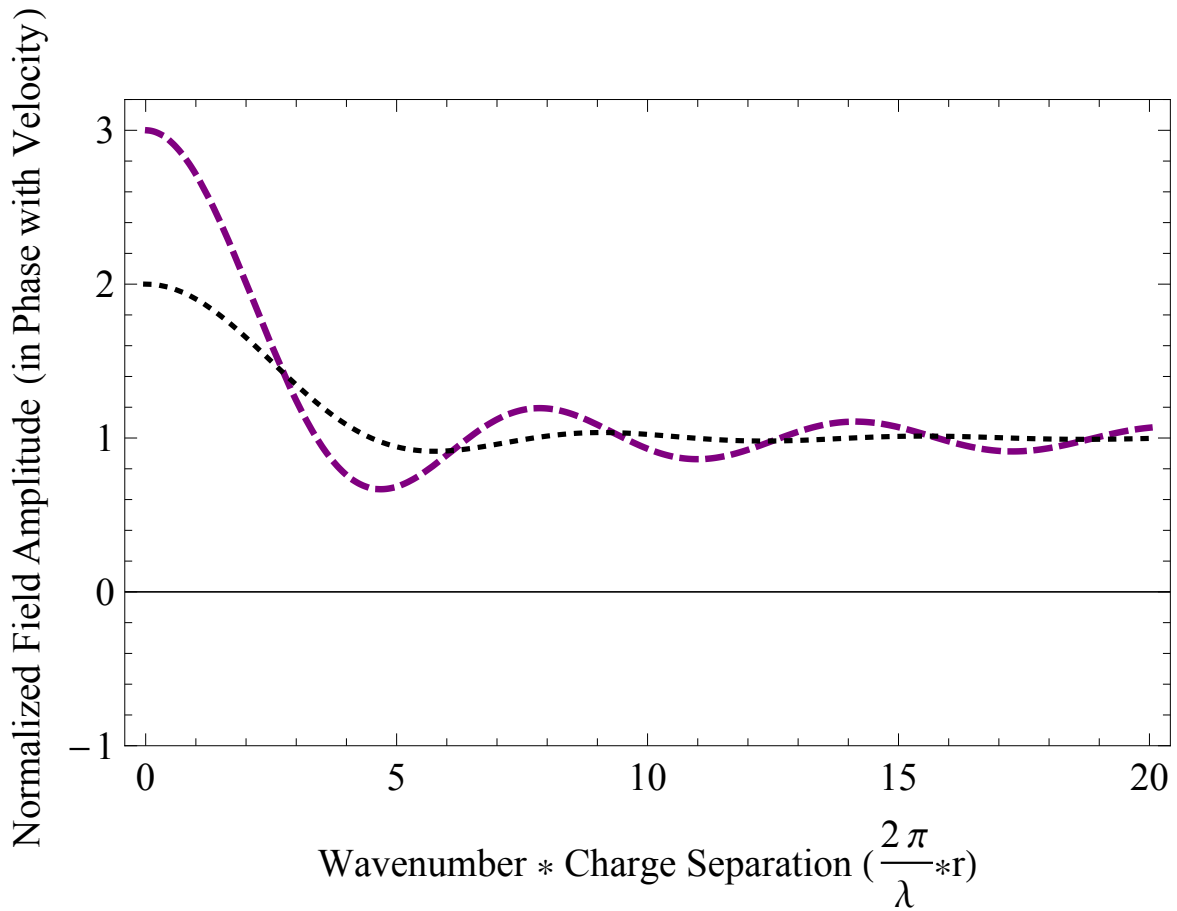
Figure 8.6: The normalized amplitudes of those components of the fields acting on the individual charges in Fig. (8.2) in phase with their velocities calculated using the retarded Lienard Wiechert potentials that determine field amplitudes in Sommerfeld's *retarded only* version of electrodynamics.
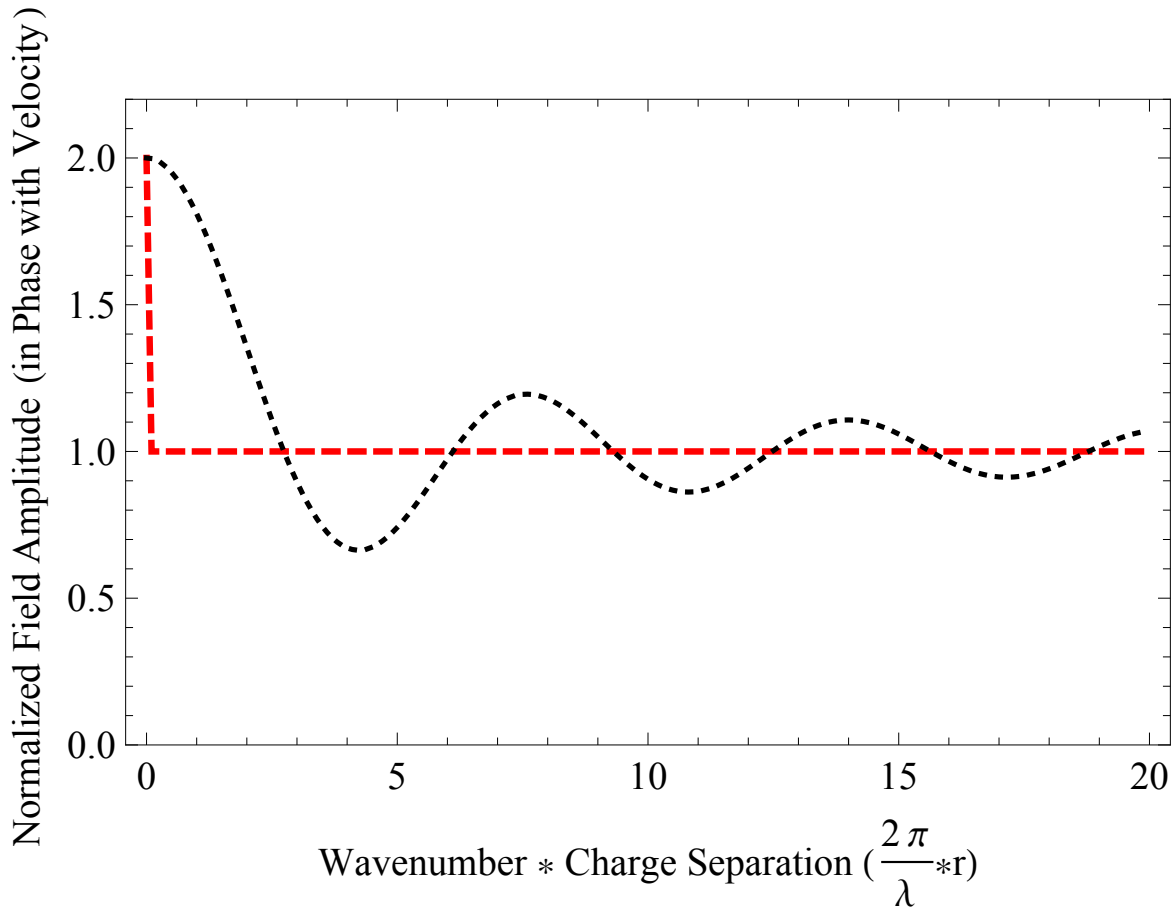
Figure 8.7: Comparison of the volume integral of $\mathbf{E} \cdot \mathbf{j}$ attributable to the Dirac coherent radiation force with the power radiated by the two oscillating charged particles' for displacements parallel to their vector accelerations. The nonlocal component of the Dirac coherent radiation reaction force falls to zero for any finite displacement of the two charges along this direction, leaving only each particle's single point radiation reaction force to oppose their oscillating velocities.
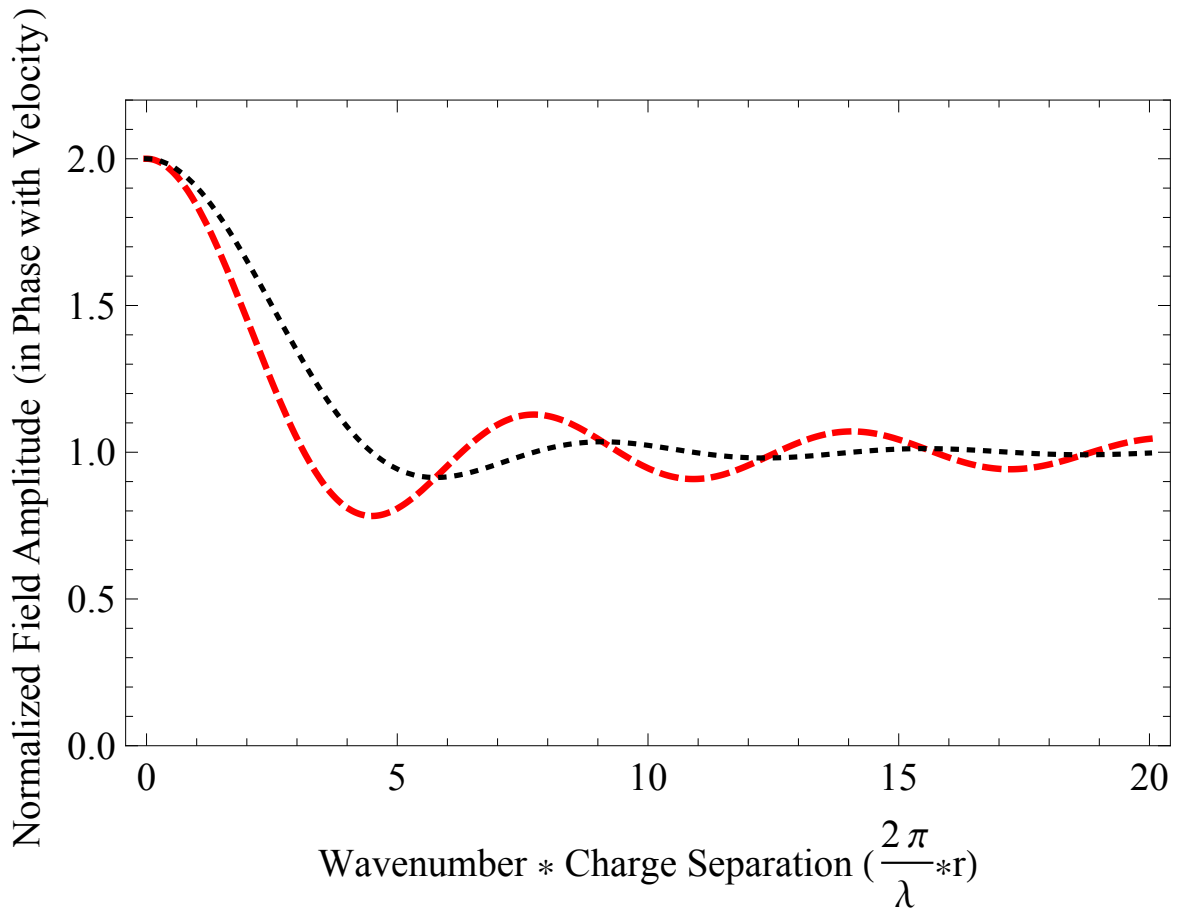
Figure 8.8: Comparison of the volume integral of $\mathbf{E} \cdot \mathbf{j}$ attributable to the Dirac coherent radiation force with the power radiated by the two oscillating charged particles' for displacements perpendicular to their vector accelerations.
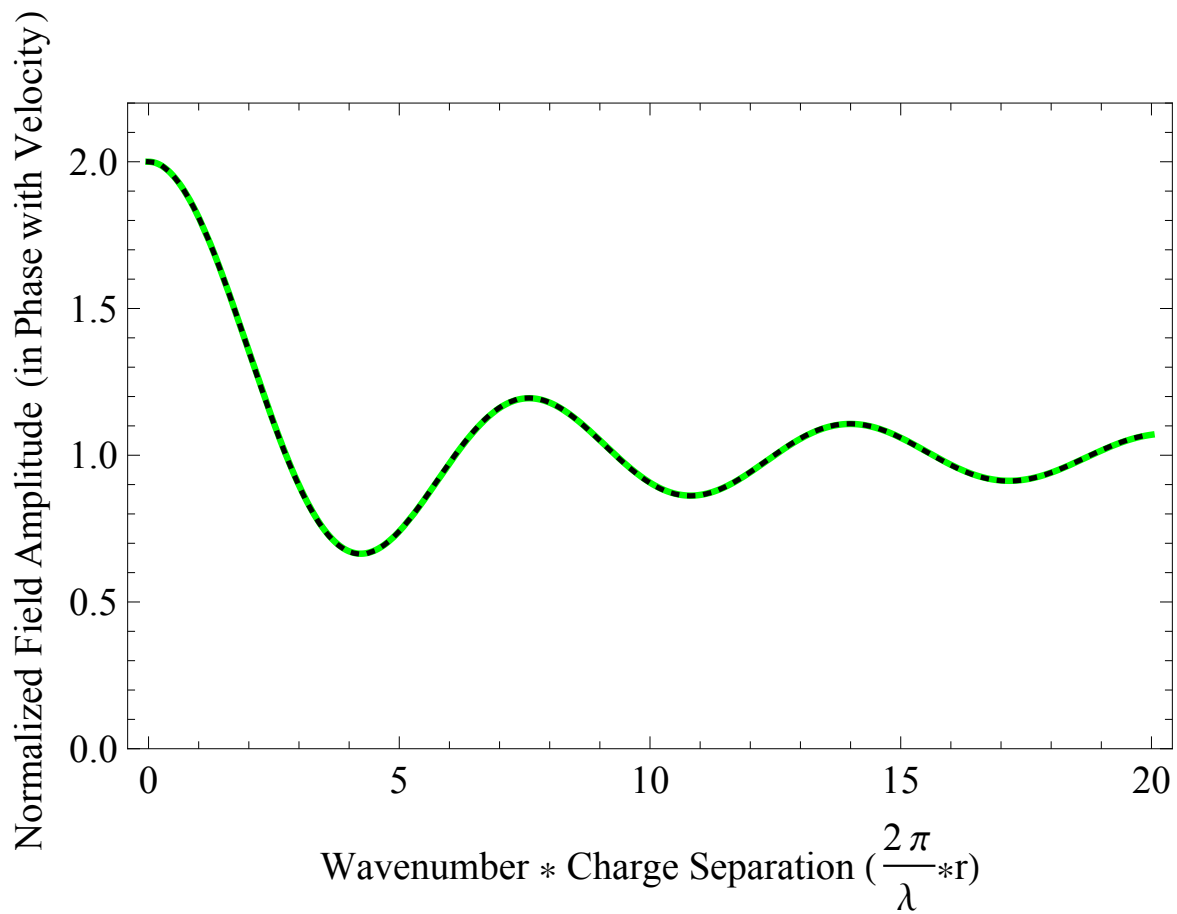
Figure 8.9: Comparison of the volume integral of $\mathbf{E} \cdot \mathbf{j}$ attributable to the Wheeler-Feynman coherent radiation force with the dependence of the two oscillating charged particles' radiated power for displacements parallel to their vector accelerations.
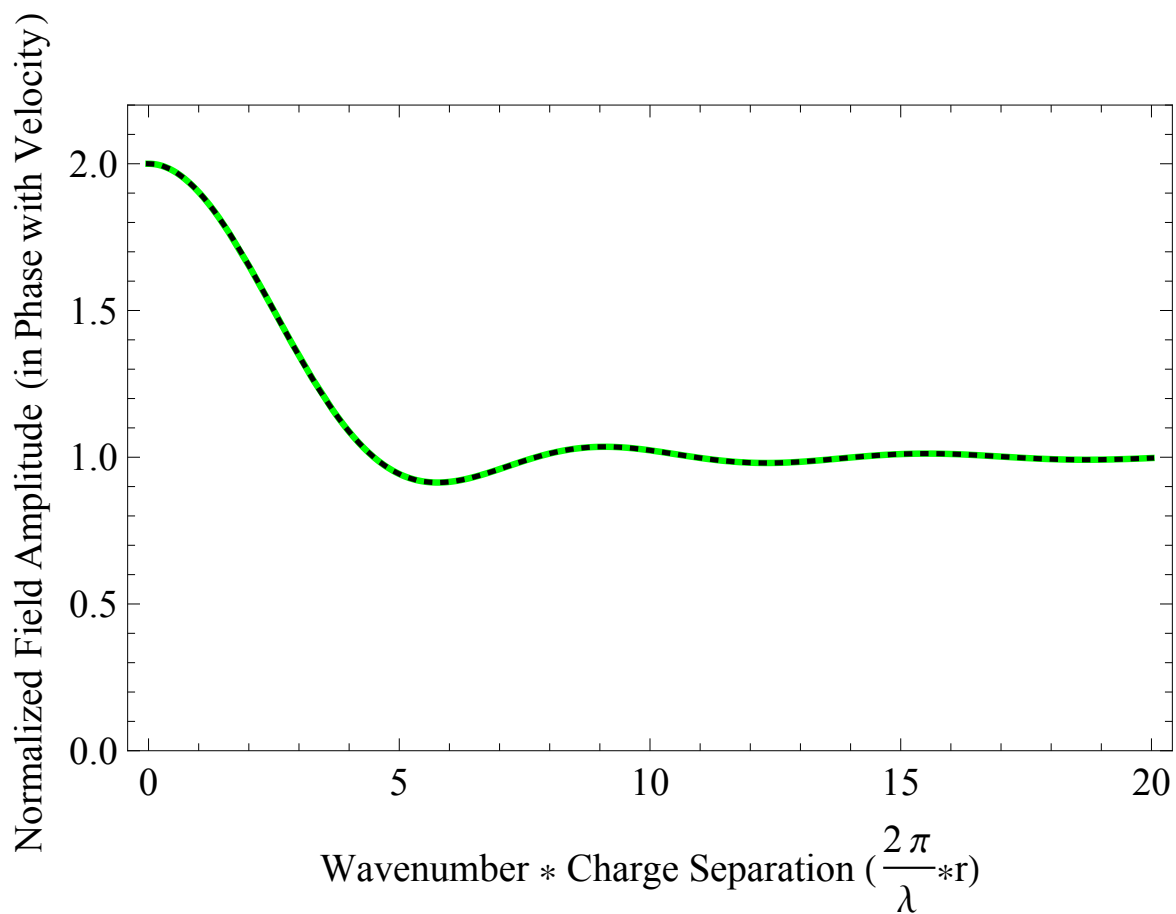
Figure 8.10: Comparison of the volume integral of $\mathbf{E} \cdot \mathbf{j}$ attributable to the Wheeler-Feynman coherent radiation force with the dependence of the two oscillating charged particles' radiated power for displacements at right angles to their vector accelerations.

CHAPTER 9
PROPOSED EXPERIMENT I: MEASUREMENT OF THE ADVANCED RADIATION REACTION FIELD IN A $\lambda/10$ ANTENNA

9.1 Related Work

Based on the discussion in chapter 7 and 8, the measurement of power delivered to a radiating antenna by calorimetric[1] means would - according to Sommerfeld's electrodynamics - exceed the power emitted by the antennas when they are spaced by short distanced parallel to the direction of their radiating elements [89, 90].

The radiation emitted by macroscopic antennas bears many similarities to the radiation emitted by elementary oscillating charges[2]. Further, it has long been known that the driving point impedance of an antenna is affected by presence of other antenna systems (resonant or nonresonant) surrounding them. In particular, it has recently been shown in general that if both advanced and retarded Green's functions are included for the case of a single antenna, a single antenna in free-space will not radiate[3] analogous to the case of the isolated oscillating charges considered by Wheeler and Feynman. Radiation only becomes possible when dissipative elements are introduced into the corresponding boundary value problem [92].

9.2 Qualitative Discussion

We discussed radiation from two oscillating charged particles and showed the variation of the radiation reaction fields with distance between the oscillating charged particles in the presence of absorbing boundary conditions. Now if we consider a small dipole antenna, it will generate a field attributable to the superposition of the many oscillating elementary charges set in motion along the surfaces of its conducting elements by its signal source [91]. We

---

[1] In case of an antenna system, one of the most reliable means of measurement available to us is measuring power outside the surface of a sphere surrounding the antennas by means of calorimetry.

[2] The similarities of the radiation emitted by antennas and by isolated elementary charges should not be surprising given that the mechanism responsible for the radiation by antennas at the microscopic scale is precisely the same accelerated motion of the charges that carry the macroscopic current in these devices.

[3] Using equations 1-25 on pages 389-393 from ref [91]

assume that the current along the elements of the dipole decreases linearly from a maximum at the feed point to zero at the ends of the dipole as is conventional in analysis of short antennas (page 413 of [58]).

For the purpose of the proposed experiment, it is important to note that if the elementary oscillating charged particles comprising the superposition are not closely spaced or not limited to a small volume in space, the interference of their individual coherent radiation reaction forces will generally result in a net force field that bears little resemblance to the force fields of the antenna's individual oscillating charged particles. To minimize this distortion, we have determined that the functional form of the Wheeler-Feynman radiation reaction field for an antenna (modeled by the superposition of single oscillating particles) converges to the form of the single-particle radiation reaction field as the dimensions of the antenna are reduced to $\lambda/10$ or less. The current distribution of the antenna can be constructed by adjusting the amplitudes and positions of the single oscillating particles to match the known current distribution for such a short dipole antenna as shown in Fig. 9.2. The advanced radiation reaction field predicted for the antenna from the radiated power and that of single oscillating particles as a function of distance r perpendicular to the direction of the current for absorbing boundaries is shown in Fig. 9.3; they are nearly identical. By measurement of the power attributed to these fields present in this antenna's vicinity it should therefore be possible to test the existence and functional form of the nonlocal coherent radiation reaction field of the Wheeler-Feynman model.

Although we live an era of technology where minimally perturbing multi-axis electric field probes are now commercially available for use in the characterization of new antenna systems, the additional means needed to measure only that component of the field that oscillates in phase with the velocity of the oscillating charged particles in the nearby radiation source appears to represent a new requirement for these field probes. We nonetheless believe that the design of such a phase sensitive field probe is within the current state of the art, though requiring a significant commitment with respect to engineering and commissioning.

Also, it will be required in any such measurement to implement the boundary conditions surrounding the transmitting antenna and field probe which should match as closely as possible the absorbing boundary conditions assumed in the Wheeler-Feynman analysis. This challenge can be overcome through the use of a high quality anechoic chamber with absorbing walls of the kind used in the field of antenna research and development. A detailed proposal and patent have been submitted based on our analysis.
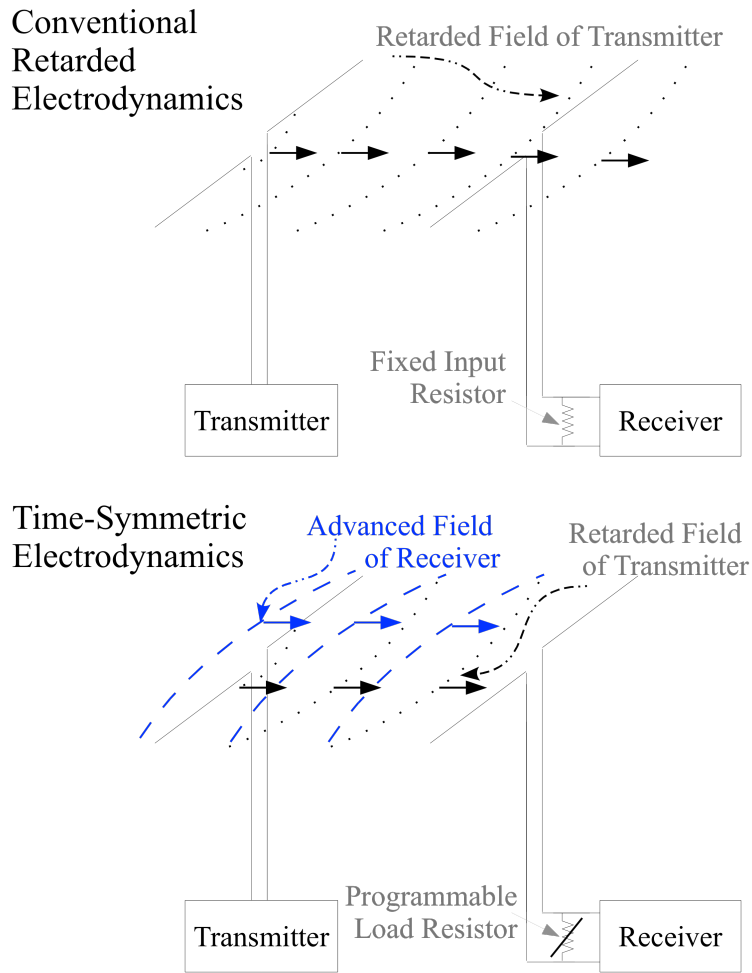
Figure 9.1: Comparing two antenna system the top one is only capable of measuring the conventional retarded field, the bottom one is able to "see" both advance and retarded field.
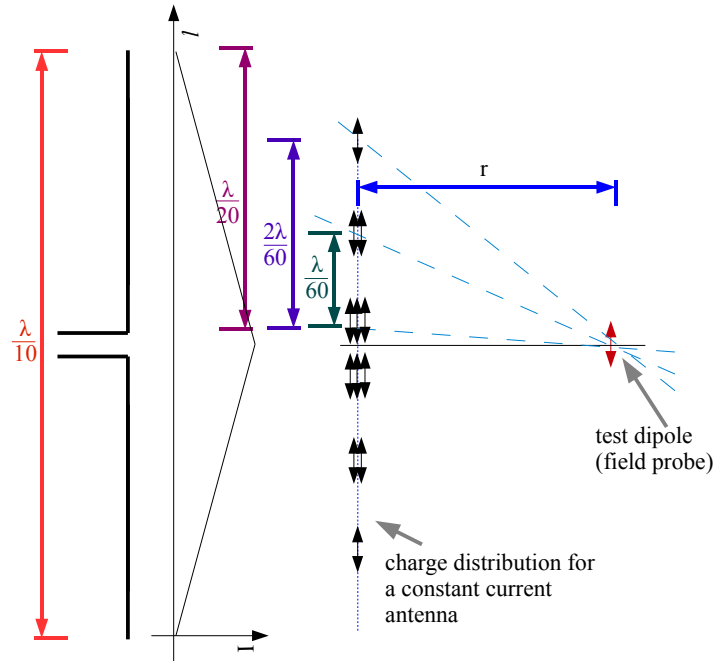
Figure 9.2: Drawing showing the distribution of elementary oscillating charged particles used to derive the form of the Wheeler-Feynman coherent radiation reaction field for the short dipole antenna with constant current I distributed along the length l of the antenna which is located at distance r from the field probe or test charge. Here r is the distance between the probe and the antenna and the axes of the probe and antenna are parallel.

The figure shows a plot. The y-axis is labeled "Normalized Total Radiation for Dipole Antennas" ranging from 0.0 to 1.2. The x-axis is labeled "Charge Separation ($\frac{2\pi}{\lambda} * r$)" ranging from 0 to 20.

Text within the plot:
Solid Green → Coherent Radiation Reaction for *a* Single Oscillating Charge

Dashed Blue → Small $\frac{\lambda}{10}$ Antenna Consist of 12 Coherently Oscillating Charges

with Amplitude Adjusted to Match Kraus' Current Distribution

Figure 9.3: Comparison of the amplitude of the Wheeler-Feynman coherent radiation reaction force for a single oscillating particle with the superposed and scaled Wheeler-Feynman fields of an array of individual oscillating particles distributed along the length of the elements of a short dipole antenna shown in Fig. 9.2 according to the known distribution of current in these elements.

CHAPTER 10
PROPOSED EXPERIMENT II: ADVANCED INTERACTIONS IN SASE FELS

10.1 Objective and Introduction

In earlier chapters we discussed the time-symmetric properties of Maxwell equations. We also discussed that our classical experience is limited to the retarded field. In the past few decades, however, there have been analyses and experiments that indirectly support the time-symmetry promised by Maxwell equations. A few of these experiments/analysis are based on the interaction of light and mater. We mentioned two of them in passing in chapter 7. Here we give a short background and discuss three of these experiments/analysis. It must be noted that these experiments played an important role our understanding of the problem presented in the earlier chapters. Next we propose an experimental setup that includes a high gain FEL.

10.1.1 Photon Decay in Cavity QED experiments

The interaction of a single atom and a single photon is at the heart of Cavity QED. This can be described in terms of a two level approximation of Rabi oscillation. If the photon lifetime in the cavity is long enough it would be possible to measure its interaction with multiple single atoms that pass through the cavity. The photon would cause the passing atoms to be suspended in any arbitrary superposition of their ground or excited states leading to complex entangled states. In his personal account of early days of cavity quantum electrodynamics, Serge Haroche discusses their quest in achieving quantum non-demolition (QND) measurement of single photon and atom [70]. One of the main breakthroughs was the observation of photon exchange between cavity mode tuned to resonance and single passing atoms in 1985. In this setup, a closed cylinder structure housed the cavity mirrors with small apertures for entry and exit of the atoms. The cavity significantly reduced the nonresonant decay of the photons. The closed structure of the cavity, however, was the cause for further technical difficulties in precision measurement. Atoms passing through tiny holes, very close to metal surfaces, produced additional fields that would disturb the atoms state. This problem was solved by using an open structure cavity with highly reflective mirrors. These

mirrors were precision machined out of copper with a small amount of superconducting niobium doping on top of them. In this setup photon lifetimes was extended to 130 ms allowing the photon to travel back and forth between the mirrors for 40,000 km. This feature that the open cavity, a reincarnation of Einstein-Bohr photon box, can reduce the photon decay similar to a closed cavity supports the time-symmetric property discussed earlier.

10.1.2 Laser Normal Mode Expansion

A highly debated analysis of laser and cavity equations of motion is the normal mode expansion by John Slater. This analysis is independent of the cavity shape and form. In his initial approximation, Slater assumes a lossless cavity with orthogonal modes [66]. For conventional laser cavities, transverse and axial modes satisfy the general biorthogonal relation (not orthogonal). In other words, their forward and reverse operators are not Hermitian, however the reverse propagator is the transpose of the forward propagator in the conventional laser cavity. Despite this, Slater's normal assumptions leads to ideal Hermite-Gaussian functions which are a very good approximation of the solutions for the system [43]. This feature also supports the time-symmetric properties discussed.

10.1.3 High Resolution Spectroscopy in a Cavity FEL

In 1993, Eric Szarmes and John Madey designed and utilized an intracavity interferometer design, in which one of the interferometer mirrors is also the cavity mirror (or vise versa), to phase lock adjacent optical pulses of MkIII FEL. The objective and result were to achieve a train of high peak power ultrashort phase locked optical pulses. In this set up the high power was achieved with an uncoated sapphire beamsplitter (the specifics of MkIII setup has been discussed in the first part of this work). Sapphire plate is birefractive (or birefringent). In this setup birefringence (or the refractive indices) of the beamsplitter was used to provide output coupling at of the P-polarized reflection near the Brewster angle at one interface and high interpulse coupling by the S-polarized reflection at the other interface simultaneously (for the same incident angle). By adjusting the position of the interferometer mirror that is not part of the cavity, laser modes can be continuously tuned. The short (350ps) spacing between the modes which is by means of controlled frequency spacing of the phase-locked laser modes provides a precise frequency calibration scale [93] and allows filtering of an individual mode in the output beam by means of a grating monochrometer and planer etalon[94, 95]. Mirror interaction with the radiation from the MkIII FEL that alters the pulse shape and spectra,

is a feature that supports instantaneous interaction between the source and target. In this setup, however, its not possible to differentiate between the advanced and retarded solutions.

10.1.4 Proposed Experiment II: Effect of an Absorber Target on Temporal Coherence of a SASE FEL

The efforts in realizing x-ray free electron lasers (FELs) and enhancing their performance has stimulated remarkable theoretical developments and experimental advances in the field. Yet, the successful operation of x-ray FELs based on the self-amplified spontaneous emission (SASE) principle which has made them a powerful new tool, has beckoned our attention for better understanding a comprehensive physical basis of the theory that has the potential to improve the temporal structure and spectral optimization of these sources. We will explain the advantages of including the coherent radiation reaction force as a part of the solution to the boundary value problem for FELs that radiate into "free space" (SASE FELs) and discuss how the advanced field of the absorber can interact with the radiating particles at the time of emission. Here we present an analytical verification for inclusion of the advance field in theory of FELs operating in free space. We will also discuss in some detail the experimental setup that could verify and/or further our understanding of the the underlying physics of these devices.

When formulated in the language of covariant action-at-a-distance, the solution to the boundary value problem corresponding to an oscillating particle within a spherical absorbing shell of arbitrary density is dominated by the interference of the retarded and advanced forces originating in the accelerated and absorbing particles [61]. This leads to a force on the accelerated particle exactly equal to that needed to match the power carried by radiation to the particles in the absorbing shell. Therefore a time-symmetric definition of electrodynamics provides non-diverging solution and origin for the radiation reaction field and satisfies Maxwell's energy integral [15]. In fact, it has also been shown that the action-at-a-distance formulation is not essential and the assumption of time-symmetry suffices for the conservation of energy [92]. The reliance of theory of SASE FELs on classical electrodynamics and their operational dependency on coherent radiation at femtosecond scale provides an excellent opportunity for the test and further study of the time-symmetric approach to electrodynamics.
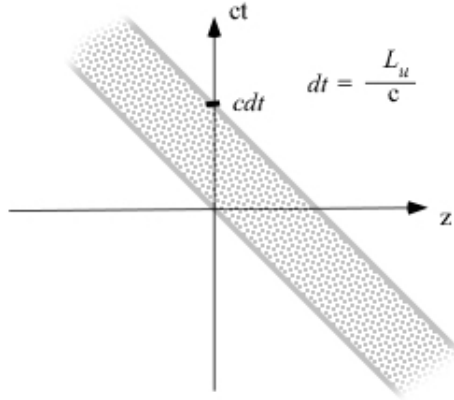
Figure 10.1: Length of the undulator defined to be equal cdt.

10.2 Conceptual Discussion

Description of FEL interactions by Kimel and Elias [51, 52] includes a viable model of the coherent radiation reaction in covariant form valid for radiation into free-space. In time-symmetric electrodynamics this can be introduced by taking in to account both the advanced and retarded field of the source and absorbing (non-emitting) particles. Applying that principle to the beam traveling in a SASE FEL, we start by considering both the advanced and retarded field/potential of both the absorber and the electrons (the emitter). It is important to note that in the absence of reflector/refractor/target in front of the electron beam traveling in z, the absorbers are the cosmological particles; and when including the effect of an absorber that far, the field and forces being considered approach the retarded field of experience). Now we must include half the retarded (outgoing) field of the emitters and the half the advanced (incoming) field of the target. The interaction of the advanced field of the target with the radiating electrons ensures energy conservation on the one hand, and on the other hand imposes the fields and forces initiated from the target on the source.

10.2.1 Non-reflecting Boundary Condition

The target mentioned above introduces a non-reflecting boundary condition to the system of the equations that must be solved. Here we refrain from calling the target an absorber to avoid confusion, since the role of the target is not absorbing the emitted photons but to be the origin of the advanced fields acting on the beam. For such signals carried on electromagnetic waves (advanced or retarded) the invariant interval $(cdt)^2 - dr^2$ between the emission of a

wave and its absorption at the non-reflecting boundary is always identically zero. So by that measure, which is the covariant statement of the distance in space-time separating transmitter and receivers, the emission and absorption of the retarded and advanced waves are all simultaneous. This has been illustrated in Fig. (10.2) Note that the advanced wave of the non-reflecting boundary (mirror) co-propagates with the fields of the undulator acting on the electrons. (The characteristics of the mirror (partially reflecting) and why it was chosen for our experiment will be explained in the next section.)

optical pulse

resonant mirror

electron bunch

reflected "retarded" wave

converging "advanced" wave

optical pulse strikes the resonant mirror

co-propagating "advanced" wave
"seeds" bunching

resonant mirror
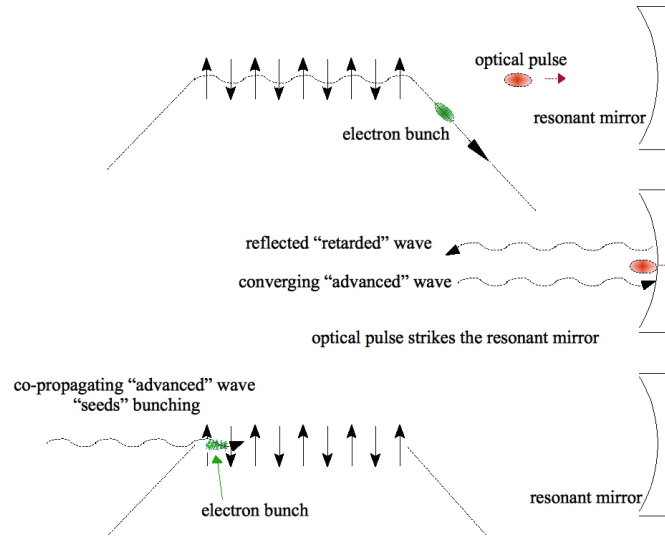
electron bunch

Figure 10.2: By the covariant statement of the distance in space-time separating transmitter and receivers, the emission and absorption of the retarded and advanced waves are all simultaneous. Presence of the mirror in front electron beam will introduce a co-propagation seed that can carry information that will improve the temporal coherence and the quality of the beam passing through the undulator.

10.2.2 Advanced Field and Evolution of Coherent Bunching in SASE

The SASE FEL starts from a randomly phased electron beam. After a few undulator periods the randomly phased electron beam gets bunched. The coherent radiation emitted by tightly bunched electron beams plays a critical role in the analysis and operation of free electron lasers. For conducting or reflecting (resonator mirror) FELs, a normal mode analysis of operation already includes the relevant boundary conditions. In order to arrive at a comprehensive first-principles field-based analysis of the intense radiation emitted into

free-space by devices that work based on the SASE principle, we also need to include the effect of boundary condition of the target.

10.3   Analytical Justification

In order to investigate the role of the advanced field, it is essential to test if the electron beam would be able to "see" the phase information that the mirror's advance field presents. Here we first discuss conceptually what the role of the mirror is, then we develop an analytical picture which verify that the advance wave of the mirror are a solution to the Maxwell's equation for fields that was briefly discussed in Ch. 2.

We discussed in Ch. 2 that the electron going through the oscillatory motion in the undulator would emit a light at the resonant wavelength of the undulator which has the same number of period as the undulator (N_u). Since SASE process starts from "noise," (stream of unbunched electron distribution), the spontaneous radiation can be modeled as random collection of gaussian spikes [4]. Each of these spikes has a width equal to the undulator coherence length $\sigma_c \sim N_u \lambda$. Therefore we can define the $E(t)$ for j electrons in the bunch by

$$E(t) = \sum_{j=1}^{N_e} E_0 \; e^{\frac{(t-t_j)^2}{2\sigma_c^2} - \frac{t^2}{2\sigma_c^2}}, \tag{10.1}$$

which in the frequency domain would be

$$E(\omega) = \sum_{j=1}^{N_e} \sqrt{2\pi} \; \sigma_c \; E_0 \; e^{-(i\omega t_j + \frac{t_j^2}{2\sigma_c^2} + \frac{\sigma_c^2 \omega^2}{2})}. \tag{10.2}$$

Then the beam would evolve as

$$E(t) = \int R(\omega) E(\omega) e^{i\omega t} d\omega. \tag{10.3}$$

As our purpose is to verify the transfer of phase information by the advance field of the mirror, we make the following approximation: 1) the mirror is essentially loss less, 2) the reflection function of the mirror is a gaussian with bandwidth of σ_ω, 3) bot beam and mirror function are expandable about a the frequency value with highest reflectivity. Then the Eq.

10.3 will go from:

$$E(t) = \int \sum_{j=1}^{N_e} \sqrt{2\pi} \; \sigma_c \; E_0 \; e^{-(i\omega t_j + \frac{t_j^2}{2\sigma_c^2} + \frac{\sigma_c^2 \omega^2}{2})} e^{i\omega t} e^{\frac{-\omega^2}{\sigma_\omega^2}} \, d\omega$$

$$= \int \sum_{j=1}^{N_e} \sqrt{2\pi} \; \sigma_c \; E_0 \; e^{-(\frac{t_j^2}{2\sigma_c^2} + \frac{\sigma_c^2 \omega^2}{2} + \frac{\omega^2}{\sigma_\omega^2})} e^{i\omega(t-t_j)} \, d\omega. \tag{10.4}$$

Then using $\sigma_c^{-1} >> \sigma_\omega$, and completing the transform integral we will have:

$$E(t) = \sum_{j=1}^{N_e} \sqrt{2\pi} \; \sigma_c \; \sigma_\omega \; E_0 \; e^{-(\frac{t_j^2}{2\sigma_c^2} + \sigma_\omega^2 (t-t_j)^2)}. \tag{10.5}$$

Notice that the new characteristic frequency for $E(t)$ is σ_ω not ω, also the amplitude of the spontaneous radiation has decreased by a factor of $\sigma_c \, \sigma_\omega$. Finally as we discussed the advance field would be the time reversed of the reflected field of the electrons.

$$E(-t) = \sum_{j=1}^{N_e} \sqrt{2\pi} \; \sigma_c \; \sigma_\omega \; E_0 \; e^{-(\frac{t_j^2}{2\sigma_c^2} + \sigma_\omega^2 (-t-t_j)^2)} \tag{10.6}$$

And Eq. (10.6) is of the from of a particular solution to the differential equation introduced in Ch. 2. These properties of the advance field supports the proposed experimental test.

10.4   Description of the Experimental Test

The discussion of time-symmetric electrodynamics goes back to conversations between Wheeler, Feynman and Einstein. Since coherent emission is central to the operation of SASE FELs, not only could SASE FELs be instrumental in the study of this fundamental aspect of electrodynamics, their technology could potentially benefit from this previously unutilized aspect of fundamental physics. The proposed setup provides just such opportunity. The qualitative justification for this experiment is the success of recent seeded experiments [96, 97]. In the experiment here the laser seed is replaced by the advanced field contributed by the mirror (As depicted in Fig. (10.2)).

10.4.1 Experimental Goal

Since SASE FELs operate based on the bunching induced by the co-propagating electrodynamic wave in these devices' undulator, they present the perfect set up for an experimental test of the model presented here. The goal of this experiment would be to evaluate the role of time-symmetric electrodynamics in operation of SASE FELs. We propose use of a multilayer bent-quartz crystal mirror at the end of the undulator to create the advanced field needed to alter the electron's bunching. This mirror will be curved (for the purpose of focusing) and be located in front of the beam and on it's transverse path right after the undulator. We ask the question: will the mirror's spontaneous response to the presence of the radiating beam (predicted by the time-symmetric electrodynamics) be able to carry phase information that will improve the temporal coherence and the quality of the beam passing through the undulator? The understanding gained from this experiment will be very important for both our current theoretical understanding and expanding the future applications of SASE FELS.

10.4.2 Bent Quartz Crystal Mirror

The bent quartz crystal mirror has two purposes. One is that only wavelengths that satisfy the Bragg condition pass through the mirror. Second, the mirror will satisfy the non-reflecting boundary condition. Therefore if the radiation wavelength is tuned to the spacing of the lattice of the quartz we can expect that wavelength radiation to transfer phase information to the beam. Of course once the wavelength is shifted it will no longer be attenuated by the mirror and pass through. Significant improvement in the spectral coherence of the beam can be expected since the focusing (bent) multilayer quartz crystal (partially reflecting mirror) will simultaneously serve as a retroreflector and a filter. In 10.1.3 we discussed a similar experiment that was conducted in the infrared regime with a dramatic improvement in the temporal coherence and spectral brightness of the emitted FEL radiation [94, 95]. Although the geometry of that experiment differ from what is proposed here, the physics is similar.

10.4.3 Set up and Required Parameters

Since the advanced co-propagating wave of the mirror will be acting as a seed laser the same condition that applies to the seeded FEL applies here: the seed power only has to exceed the spontaneous noise emitted into the coherent bandwidth and angle [49]. The wavelength of the radiation must match the spacing of the quartz lattice in one direction.
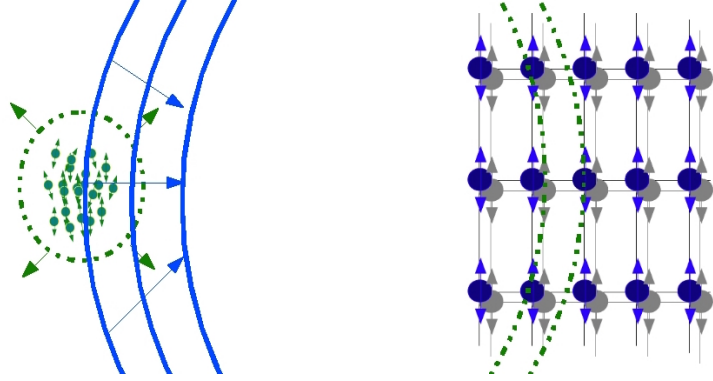
Figure 10.3: Retarded field of the source (green) and converging advance field of the absorber (blue).

Also the mirror must be located right after the undulator or beam dump to have access to a natural (unfiltered) SASE bandwidth. An optimal set of parameters for the experiment is presented in Table (10.1). It must be noted that these parameters, considering the currently

Table 10.1: Optimal Radiated Beam Parameters for Proposed Experiment II.

Parameters	Values
Beam Wavelength	1 Angstrom
Bandwidth	Natural SASE BW
Pulse energy	1 mJ or less
Pulse Duration	70 fs
Spot size	micron range
Rep. Rate	1 Hz or Less

available technology, make the experiment challenging as they are at the frontier of available parameters by current light sources that we have discussed. With further investigation, however, we hope to simplify some aspect of the experiment. These plans will be briefly discussed next.

Part III

Outlook

CHAPTER 11
CONCLUSION AND FUTURE PLANS

High brightness sources of x-rays and γ-rays are in demand more than ever before. They have been an exceptional tool for discovery and investigation of atomic scale phenomenal. Many large scale facilities with exceptional capabilities are on their way. This makes the underlying physics of radiation of prime importance. On the other hand, only limited resources are available for these large scale facilities. While the manifested advantages of these sources make them desirable to many fields, institutions and even countries, not all can afford it. This makes development of compact facilities such as one based on the MkV inverse-Compton source desirable. The ultimate goal for the ICS experiment at UH is to provide an affordable coherent source with high average brightness by means of GHz-rate electron and laser beam interactions. We report here that excellent progress is being made with in this respect.

One of the primary concerns of this work was achieving an optimal reproducible match for the electron beam to a complex system such as MkV ICS source. In Chapter 4. we discussed all the necessary elements and steps that were taken to provide the needed diagnostic and control capabilities. In chapter 5, we demonstrated that after investigating the beamline through simulation runs and modeling the beamline based on thin lens approximation, we were able to arrive at an elegant solution . This solution is executable through a systematic approach and the results are reproducible within the accessible stability of the system. In chapter 6. we investigated the compatibility of the beam diagnostics with other elements and requirement of the system.

Further development of the microwave gun (addition of laser cooling) and commissioning the tested out four-mirror [30] optical cavity are under way at University of Hawai'i. Additional studies to reduce the mulitpactoring in the waveguide are also being pursued. With the above additions, the MkV would have all the necessary elements and capabilities to achieve its goal. The chance to work on the MkV system has been of great value to me and many other students. Instead of having to perform start to end simulation for a particular design, we have had the chance to a hands on experience with a working system which has provided us with much needed intuition and understanding. This has been a rare opportunity.

The other main concern of this document was to perform a thorough study of the problem of coherent radiation in classical electrodynamics. In part II, we refuted the argument that

problem of conservation of energy in CED lies with the failure of classical physics at small scales since the discussed Maxwell energy integral test in for coherent emission in chapter 8 fails at all wavelengths and physical scales including meter and microwave wavelengths. Additionally, we showed that the Wheeler-Feynman analysis of the radiation emitted by a moving charge interacting with absorbing boundary conditions (a definition based on time symmetry in classical electrodynamics) provides a perfect match to the radiated power and radiation reaction fields for the case of two coherently oscillating particles. Some aspects of the model remain controversial and it has been considered a conceptually demanding theory [98]. It is, however, unique amongst the possible physical models in complying with Maxwell's energy integral for coherently radiating pairs of particles. Therefore, the manifest failure of conventional retarded electrodynamics makes it clear that existing retarded CED theory must be reformulated to achieve consistency with Maxwell's equations. This could be examined in detail in the case of antenna experiment. A detailed proposal for this experiment has been submitted and further studies are being done by Steven Smith.

Classical electrodynamics still serves as basis of our understanding of the dynamics of complex, macroscopic systems of charges and currents in the strong signal regime subject to complex, realistic boundary conditions. Classical electrodynamic's treatment of radiation will therefore remain the foundation for theoretical advancements in the future development of light sources where systems including as many as 10^{10} radiating electrons may need to be considered. The reliance of theory of SASE FELs on classical electrodynamics and their operational dependency on coherent radiation in free space at femtosecond scale provides an excellent opportunity for the test and further study of the time-symmetric approach to electrodynamics. In the last chapter we put forward a scheme for the SASE test that has raised some interest in an international level. The most logical next step in this case is to obtain simulation results for the proposed test. Since we are looking for a previously un-utilized aspect of physics, the most appropriate approach would be to write a dedicated simulation of this problem. We also hope to gain further insight into the problem by studying some of the intrinsic properties of SASE FEL such as shot noise and electron fluctuations.

The underlying motivation for both parts of this dissertation has been to improve upon the capabilities of the current and future relativistic electron beam x-ray sources. By studying the electrodynamics of such sources we hope to gain a more physically valid analysis of these sources and provide different fields of science and technology with an exceptional tool for investigation the subatomic level phenomena.

APPENDIX A
PHYSICAL LOCATION OF BEAMLINE
ELEMENTS WITH THEIR CORRESPONDING
CHANNEL NUMBER

Here we present a list of all channels supporting the electromagnetic magnets of the diagnostic chicaine. All the quadrupoles from this list were included in the transport simulation module. The distance in meter is from the end of the linac and these are the updated current values.

Table A.1: Table of Beamline Elements.

Channel Number	Magnet Function	Distance (m)
20	Linac Quad	0.394
21	Linac Quad	0.699
22	Vertical Corrector	0.838
23	Spectrometer	1.105
24	Vertical Corrector	1.461
26	Split Bend 1	1.753-2.400
28	Chromaticity Quad	2.070
29	Quad	2.769
30	Quad	2.896
31	Quad	3.023
32	Split Bend 2	3.531-3.861
34	Chromaticity Quad	3.594
35	Vertical Corrector	4.102
36	Horizonatal Corrector	4.102
37	Quad	4.204
38	Quad	4.331
39	Quad	4.483
40	Quad	4.978
41	Quad	5.144
42	Quad	5.271
45	Split Bend 3	5.271-6.147

Table A.1: Table of Beamline Elements.

Channel Number	Magnet Function	Distance (m)
47	Chromaticity Quad	5.867
43	Vertical Corrector	6.464
44	Horizonatal Corrector	6.464
48	Double Quad A Before IP	6.566
49	Double Quad B Before IP	6.680
51	Vertical Corrector	7.353
50	Double Quad B After IP	7.442
59	Double Quad A After IP	7.569
52	Split Bend 4	7.849-8.420
53	Chromaticity Quad	8.141
56	Quad	8.636
57	Quad	8.763
58	Quad	8.890
60	Vertical Corrector	9.017
61	Split Bend 5	9.335-9.982
62	Quad	10.224
65	Vertical Corrector	10.351
63	Quad	10.630
64	Quad	10.757
70	Vertical Corrector	12.167

APPENDIX B
SUMMARY OF THE WHEELER AND FEYNMAN APPROACH AND THE RESULTANT FORMULAS

Wheeler and Feynman's 1945 paper [61] illustrates how advanced forces from a far off absorber can be employed to build an action-at-a-distance model of radiation that intrinsically includes the radiation reaction force in a covariant and causal formulation consistent with observation. Wheeler and Feynman present four increasingly complex derivations using an absorber of arbitrary density. First, they derive an expression for the radiation reaction force on a nonrelativistic accelerated source charge. Second, they derive the fields responsible for the radiation reaction force on that source charge and show how the advanced forces cancel everywhere except at the source charge leading to *retarded only* radiation at long distances from the source, consistent with experience. Third, they consider the source charge to be moving with arbitrary velocity, and forth they take a completely general approach. The result established in the second derivation, Eq (B.1a), constitutes the analytic basis of our analysis of the coherent radiation reaction problem for this paper. Here we summarize how Wheeler and Feynman arrive at this formula.

To calculate the effect of distant absorbers on the forces in the vicinity of an accelerating source charge, first the assumed retarded field of the charge traveling outbound is used to calculate the motions of the absorber particles, then the sum of the advanced forces from the absorber near the source is calculated. It is shown that addition of this field to the actual half-advanced plus half-retarded field of the source gives the assumed fully retarded field of the source while producing the correct radiation reaction force at the position of the source. Using their formulation, the force on a particle of charge e at distance d from the source charge is

$$\mathbf{F}_{WF-rrf}(\frac{\omega d}{c}, t) = \frac{2e^2}{3c^3}(-i\omega a_0)\exp(-i\omega t)\ [F_0(\frac{\omega d}{c}) - P_2(\cos(\mathbf{a}, d))F_2(\frac{\omega d}{c})] \qquad \text{(B.1a)}$$

$$F_0(u) = \frac{1}{2}\int_{-1}^{1}\exp(iu\cos\theta)d\cos\theta \qquad \text{(B.1b)}$$

$$F_2(u) = \frac{1}{2}\int_{-1}^{1}\exp(iu\cos\theta)P_2(\cos\theta)d\cos\theta. \qquad \text{(B.1c)}$$

For a large d both the F_0 and F_2 terms reduce to

$$\frac{[\exp(iu) - \exp(-iu)]}{2iu} \tag{B.2}$$

and $\mathbf{F}_{WF-rrf}$ becomes $\mathbf{F}_{Dirac-rrf}$ indicating that the advanced field of the absorber in the vicinity of a source charge is equal to the half-advanced minus half-retarded field of the source itself.

BIBLIOGRAPHY

[1] A. Chodos. November 8, 1895: Roentgen's Discovery of X-Rays. *APS News: This Month in Physics History*, 10(10), 2001.

[2] J. M. J. Madey. Stimulated Emission of Bremsstrahlung in a Periodic Magnetic Field. *Journal of Applied Physics*, 42(5):1906, 1971.

[3] K. J. Kim, Z. Huang, and R. Lindberg. *Synchrotron Radiation and Free Electron Lasers: Principles of Coherent X-Ray Generation*. To be published.

[4] C. Pellegrini, A. Marinelli, and S. Reiche. The physics of x-ray free-electron lasers. *Reviews of Modern Physics*, 88(1):015006, March 2016.

[5] The Linac Coherent Light Source (LCLS), <http://lcls.slac.stanford.edu/>, 2016.

[6] FLASH, the Free-Electron LASer in Hamburg, <http://photon-science.desy.de/facilities/flash/>, 2016.

[7] P. Emma, R. Akre, J. Arthur, R. Bionta, C. Bostedt, J. Bozek, A. Brachmann, P. Bucksbaum, R. Coffee, F.-J. Decker, Y. Ding, D. Dowell, S. Edstrom, A. Fisher, J. Frisch, S. Gilevich, J. Hastings, G. Hays, Ph. Hering, Z. Huang, R. Iverson, H. Loos, M. Messerschmidt, A. Miahnahri, S. Moeller, H.-D. Nuhn, G. Pile, D. Ratner, J. Rzepiela, D. Schultz, T. Smith, P. Stefan, H. Tompkins, J. Turner, J. Welch, W. White, J. Wu, G. Yocky, and J. Galayda. First lasing and operation of an ångstrom-wavelength free-electron laser. *Nature Photonics*, 4(9):641–647, August 2010.

[8] The European XFEL,<http://www.xfel.eu/>, 2015.

[9] L. R. Elias, W. M. Fairbank, J. M. J. Madey, H. A. Schwettman, and T. I. Smith. Observation of Stimulated Emission of Radiation by Relativistic Electrons in a Spatially Periodic Transverse Magnetic Field. *Physical Review Letters*, 36(13):717–720, March 1976.

[10] D. A. G. Deacon, L. R. Elias, J. M. J. Madey, G. J. Ramian, H. A. Schwettman, and T. I. Smith. First Operation of a Free-Electron Laser. *Physical Review Letters*, 38(16):892–894, April 1977.

[11] J. M. J. Madey and J. M. D. Kowalczyk. Use of etendue and energy spread to assess inverse-Compton X-ray sources for Applications. In *High-Brightness Sources and Light-Driven Interactions*, volume Long Beach, page EM1A.1, Washington, D.C., 2016. OSA.

[12] E. B. Szarmes. *Optical cavity for coherent superposition of optical pulses.* US Patent 7,532,649, May 12, 2009.

[13] E. B. Szarmes, A. D. Madden, and J. M. J. Madey. Optical phase locking of a 286-GHz harmonically mode-locked free-electron laser. *Journal of the Optical Society of America B*, 13(7):1588, July 1996.

[14] E. B. Szarmes. *Phase locked free electron laser with rational mode locking,.* Patent 6,643,314., 2003.

[15] P. Niknejadi, J. M. J. Madey, and J. M. D. Kowalczyk. Radiated power and radiation reaction forces of coherently oscillating charged particles in classical electrodynamics. *Physical Review D*, 91(9):096006, May 2015.

[16] H. Wiedemann. *Particle Accelerator Physics.* Springer, 3rd edition, 2007.

[17] A. Seryi. *Unifying Physics of Accelerators, Lasers and Plasma.* CRC Press, 2015.

[18] E. B. Szarmes. *Classical Theory of Free-Electron Lasers.* Lecture Notes, University of Hawaii, 2013.

[19] A. Hofmann. Charactristics of Synchrotron Radiation. In S. Turner, editor, *CAS: CERN Accelerator School.* CERN, Geneva, Switzerland, 1998.

[20] E. Hecht. *Optics.* Addison-Wesley, 4th edition, 2001.

[21] F. R. Arutyunian and V. A. Tumanian. The Compton effect on relativistic electrons and the possibility of obtaining high energy beams. *Physics Letters*, 4(3):176–178, April 1963.

[22] J. M. J. Madey, E. B. Szarmes, M. R. Hadmack, B. T. Jacobson, J. M. D. Kowalczyk, and P. Niknejadi. Optimized Cavity-Enhanced X-Ray Sources for X-Ray Microscopy. *SPIE 8851, X-Ray Nanoimaging: Instruments and Methods,*, 88510W, 2013.

[23] C. Pellegrini and J. B. Murphy. Introduction to the physics of the free electron laser. *Laser Handbook*, 6(2), 1990.

[24] J. M. J. Madey. Private Communication, 2015.

[25] A. Bacci, C. Maroli, V. Petrillo, A. R. Rossi, L. Serafini, and P Tomassini. Compact xray free-electron laser based on an optical undulator. *Nuclear Instruments and Methods in Physics Research Section A: Accelerators, Spectrometers, Detectors and Associated Equipment*, 587(2-3):388 – 397, 2008.

[26] Lanthanum and Cerium Hexaboride, `<https://www.emsdiasum.com/microscopy/products/microscope/lab6_ceb6.aspx>`, 2015.

[27] J. M. D. Kowalczyk. *Increased Power, Pulse length, and Spectral purity Free Electron Laser For Inverse Compton X-ray Production And Laser Induced Breakdown Spectriscopy of Thin Film Photovoltaics*. Phd thesis, University of Hawaii at Manoa, 2011.

[28] R. B. Neal. *The Stanford Two-Mile Accelerator*. 1967.

[29] B. T. Jacobson, J. M. J. Madey, and P. Niknejadi. Design and Commissioning of Chasman-Green Double Bend Achromatic Lattice Linear Transport Line at the University of Hawai'i MkV Accelerator Facility. In *IPAC Conference Procceding*, page 2280, 2013.

[30] M. R. Hadmack. *An optical storage cavity-based, Compton-backscatter x-ray source using the MKV free electron laser*. PhD thesis, Universty of Hawaii at Manoa, 2012.

[31] B. T. Jacobson. *Design, Commissioning, and Operation of MkV Electron Beam Diagnostic Chicane*. PhD thesis, University of Hawaii at Manoa, 2011.

[32] B. T. Jacobson, J. M. J. Madey, M. R. Hadmack, J. M. D. Kowalczyk, and P. Niknejadi. Modular Logarithmic Amplifier Beam Position Monitor Readout System atUniversity of Hawai'i. *IBIC Conference Procceding*, page 90, 2012.

[33] NIST: X-Ray Mass Attenuation Coefficients,`<http://physics.nist.gov/PhysRefData/XrayMassCoef/>`, 2015.

[34] YAP Conversion Efficiency,`<http://www.crytur.cz/pages/33/crytur-materials>`, 2016.

[35] M. Rubin. On Optical properties of soda lime silica glasses. *Solar Energy Materials*, 12:275–288, 1985.

[36] J. M. D. Kowalczyk. Private Communication, 2015.

[37] J. M. D. Kowalczyk. Email Correspondence, 2016.

[38] P. B. Sewell. Oxygen activation of LAB6 cathodes-The double saturation effect. *Kimball Physics, Inc. Technical Bulletin # LaB6-04B*, 1991.

[39] E. Oberla, J. F. Genat, H. Grabas, H. Frisch, K. Nishimura, and G. Varner. A 15GSa/s, 1.5GHz bandwidth waveform digitizing ASIC. *Nuclear Instruments and Methods in Physics Research Section A: Accelerators, Spectrometers, Detectors and Associated Equipment*, 735:452–461, January 2014.

[40] P. Orel, G. S. Varner, and P. Niknejadi. Feasibility Study of a Novel Low Occupancy Vertex Detector Architecture Based on High Precision Timing for High Luminosity Particle Colliders. *Prepared for submission to JINST*.

[41] J. M. J. Madey. Wilson Prize article: From vacuum tubes to lasers and back again1. *Physical Review Special Topics - Accelerators and Beams*, 17(7):074901, July 2014.

[42] R. E. Collin. *Foundations for Microwave Engineering*. Wiley-IEEE Press, New York, NY, 2 edition, 2001.

[43] A. E. Siegman. *Lasers*. University Science Books, 1986.

[44] A. M. Kondratenko and E. L. Saldin. Generation of coherent radiation by a relativistic electron beam in an ondulator*. *Particle Accelerators*, 10:207–216, 1980.

[45] Y. S. Derbenev, A. M. Kondratenko, and E. L. Saldin. On the possibility of using a free electron laser for polarization of electrons in storage rings. *Nuclear Instruments and Methods in Physics Research*, 193(3):415–421, March 1982.

[46] J. B. Murphy and C. Pellegrini. Free electron lasers for the XUV spectral region. *Nuclear Instruments and Methods in Physics Research Section A: Accelerators, Spectrometers, Detectors and Associated Equipment*, 237(1-2):159–167, June 1985.

[47] J. B. Murphy and C. Pellegrini. Generation of high-intensity coherent radiation in the soft-x-ray and vacuum-ultraviolet region. *Journal of the Optical Society of America B*, 2(1):259, January 1985.

[48] M. Xie and D. A. G. Deacon. Theoretical study of FEL active guiding in the small signal regime. *Nuclear Instruments and Methods in Physics Research Section A: Accelerators, Spectrometers, Detectors and Associated Equipment*, 250(1-2):426–431, September 1986.

[49] Z. Huang and K. J. Kim. Review of x-ray free-electron laser theory. *Physical Review Special Topics - Accelerators and Beams*, 10(3):034801, March 2007.

[50] P. Niknejadi and J. M. J. Madey. A Novel Modeling Approach for Electron Beams in SASE FELs. In *Proceedings of Free Electron Laser Conference*, Basel, Switzerland, 2014. JACoW (preprint).

[51] I. Kimel and L. R. Elias. Coherent Radiation Reaction in Free-Electron Sources. *Physical Review Letters*, 75(23):4210–4213, 1995.

[52] I. Kimel and L. R. Elias. The role of radiation reaction in Lienard-Wiechert description of FEL interaction. *Nuclear Instruments and Methods in Physics Research Section A: Accelerators, Spectrometers, Detectors and Associated Equipment*, 375(1-3):565–568, June 1996.

[53] D. J. Griffiths, T. C. Proctor, and D. F. Schroeter. Abraham-Lorentz versus Landau-Lifshitz. *American Journal of Physics*, 78(4):391, 2010.

[54] M. Abraham. *Annalen der Physik*, 315:105–179, 1902.

[55] H. A. Lorentz. Electromagnetic Phenomena in a System Moving with Any Velocity Smaller than That of Light. *Proceedings of the Royal Netherlands Academy of Arts and Sciences*, 6:809–831, 1904.

[56] L. D. Landau and E. M. Lifshitz. *The Classical Theory of Fields, Volume 2*. Addison-Wesley, Reading, MA, 4th edition, 1975.

[57] S. E. Gralla, A. I. Harte, and R. M. Wald. Rigorous derivation of electromagnetic self-force. *Physical Review D*, 80(2):024031, July 2009.

[58] J. D. Jackson. *Classical electrodynamics*. Wiley, New York, NY, 3rd edition, 1975.

[59] W. Ritz and A. Einstein. On the Present Status of the Radiation Problem. *Physikalische Zeitschrift*, 10:323, 1909.

[60] W. K. H. Panofsky and M. Phillips. *Classical Electricity and Magnetism.* Courier Dover Publications, Mineola, NY, 2nd edition, 2012.

[61] J. A. Wheeler and R. P. Feynman. Interaction with the Absorber as the Mechanism of Radiation. *Reviews of Modern Physics*, 17(2-3):157, April 1945.

[62] A. M. Liénard. Champ électrique et Magnétique. *L'Eclairage Electrique*, 16(27-29):5–14 , 53–59, 106–112, 1898.

[63] E. Wiechert. Elektrodynamische Elementargesetze. *Archives Néerlandaises*, 5:549–573, 1900.

[64] S. H. Schot. Eighty Years of Sommerfeld's Radiation Condition. *Historia Mathematica*, 19(4):385–401, November 1992.

[65] A. Einstein. On the Present Status of the Radiation Problem. *Physikalische Zeitschrift*, 10:185–193, 1909.

[66] J. Slater. *Reviews of Modern Physics*, 18:441, 1946.

[67] W. Lamb. Theory of an Optical Maser. *Physical Review*, 134(6A):A1429–A1450, June 1964.

[68] C. Mead. *Collective Electrodynamics: Quantum Foundations of Electromagnetism.* MIT Press, Boston, MA, 2000.

[69] K. McDonald. Email Correspondence, 2011.

[70] S. Haroche. Nobel Lecture: Controlling photons in a box and exploring the quantum to classical boundary. *Reviews of Modern Physics*, 85(3):1083–1102, July 2013.

[71] C. F. Gauss. *Werke*, 5:629, 1867.

[72] K. Schwarzschild. *Göttinger Nachrichten*, 128:132, 1903.

[73] H. Tetrode. *Zeits. F. Physik*, 10:317, 1922.

[74] A. D. Fokker. *Zeits. F. Physik*, 58:386, 1929.

[75] A. D. Fokker. *Physica*, 9:33, 1929.

[76] A. D. Fokker. *Physica*, 12:145, 1932.

[77] J. L. Synge. On the Electromagnetic Two-Body Problem. *Proceedings of the Royal Society A: Mathematical, Physical and Engineering Sciences*, 177(968):118–139, December 1940.

[78] J. A. Wheeler and R. P. Feynman. Interaction with the Absorber as the Mechanism of Radiation. *Reviews of Modern Physics*, 17(2-3):160, April 1945.

[79] J. A. Wheeler and R. P. Feynman. Interaction with the Absorber as the Mechanism of Radiation. *Reviews of Modern Physics*, 17(2-3):162–165, April 1945.

[80] H. A. Lorentz. *The Theory of Electrons and Its Applications to the Phenomena of Light and Radiant Heat.* Columbia University Press, New York City, NY, 1909.

[81] J. A. Wheeler and R. P. Feynman. Interaction with the Absorber as the Mechanism of Radiation. *Reviews of Modern Physics*, 17(2-3):165, April 1945.

[82] F. Hoyle and J. Narlikar. Cosmology and action-at-a-distance electrodynamics. *Reviews of Modern Physics*, 67(1):113–155, January 1995.

[83] J. G. Cramer. Generalized absorber theory and the Einstein-Podolsky-Rosen paradox. *Physical Review D*, 22(2):362–376, July 1980.

[84] D. J. Griffiths. *Introduction to electrodynamics.* Prentice Hall, Upper Saddle River, NJ, 3rd edition, 1999.

[85] I. Howe. *Classical Coherent Radiation for Multiple Particles.* PhD thesis, University of Hawaii at Manoa, 2014.

[86] P. A. M. Dirac. Classical Theory of Radiating Electrons. *Proceedings of the Royal Society A: Mathematical, Physical and Engineering Sciences*, 167(929):148–169, August 1938.

[87] J. Mathews and R. L. Walker. *Mathematical Methods of Physics.* Addison Wesley, Redwood City, California, 2nd edition, 1970.

[88] J. M. J. Madey. *Class Notes on Electrodynamics for Graduate Students.* unpublished.

[89] J. M. J. Madey. Email Correspondence, 2016.

[90] J. M. J. Madey, P. Niknejadi, and J. M. D. Kowalczyk. Maxwell's "Energy Integral" and the need for time-symmetric electrodynamics. *Prepared for submission.*

[91] J. D. Kraus. *Antennas.* McGraw-Hill, New York, NY, 2nd edition, 1988.

[92] S. Smith. Role of Absorption in Radiation by Isolated Dipoles Interacting via a Time-Symmetric Green's Function. *Prepared for submission.*

[93] J. N. Eckstein, A. I. Ferguson, and T. W. Hänsch. High-Resolution Two-Photon Spectroscopy with Picosecond Light Pulses. *Physical Review Letters*, 40(13):847–850, March 1978.

[94] E. B. Szarmes and J. M. J. Madey. The Michelson resonator free-electron laser. I. Passive mode structure and mode decay. *IEEE Journal of Quantum Electronics*, 29(2):452–464, 1993.

[95] E. B. Szarmes and J. M. J. Madey. The Michelson resonator free-electron laser. II. Supermode structure and mirror detuning effects. *IEEE Journal of Quantum Electronics*, 29(2):465–478, 1993.

[96] M. Ferray, A. L'Huillier, X. F. Li, L. A. Lompre, G. Mainfray, and C. Manus. Multiple-harmonic conversion of 1064 nm radiation in rare gases. *Journal of Physics B: Atomic, Molecular and Optical Physics*, 21(3):L31–L35, February 1988.

[97] L. H. Yu. Generation of intense uv radiation by subharmonically seeded single-pass free-electron lasers. *Physical Review A*, 44(8):5178–5193, October 1991.

[98] S. Gregson, J. McCormick, and C. Parini. *Principles of Planar Near-Field Antenna Measurements.* The Institution of Engineering and Technology, London, United Kingdom, 2007.

[99] K. J. Kim. An analysis of self-amplified spontaneous emission. *Nuclear Instruments and Methods in Physics Research Section A: Accelerators, Spectrometers, Detectors and Associated Equipment*, 250(1-2):396–403, September 1986.

[100] P. Niknejadi and J. M. J. Madey. Inclusion of Advanced Fields and Boundary Conditions in the Analytic Theory of High Gain FELs. In *FEL Conference Procceding*, page WEP079, 2015.